The effects of aberrations in synthetic aperture systems

THE EFFECTS OF ABERRATIONS IN SYNTHETIC APERTURE SYSTEMS

by

Ross Brian Hooker III

A Dissertation Submitted to the Faculty of the

COMMITTEE ON OPTICAL SCIENCES (GRADUATE)

In Partial Filfillment of the Requirements

For the Degree of

DOCTOR OF PHILOSOPHY

In the Graduate College

THE UNIVERSITY OF ARIZONA

1 9 7 4

THE UNIVERSITY OF ARIZONA

GRADUATE COLLEGE

I hereby recommend that this dissertation prepared under my direction by Ross Brian Hooker III

entitled The Effects of Aberrations in Synthetic Aperture Systems

be accepted as fulfilling the dissertation requirement of the degree of Doctor of Philosophy

Jack D. Gaskill — 28 August 1974

Dissertation Director — Date

After inspection of the final copy of the dissertation, the following members of the Final Examination Committee concur in its approval and recommend its acceptance:*

P.N. Slater	28 Aug '74
Roland V. Shack	28 AUG 1974
W. Swindell	18 Sept 1974

*This approval and acceptance is contingent on the candidate's adequate performance and defense of this dissertation at the final oral examination. The inclusion of this sheet bound into the library copy of the dissertation is evidence of satisfactory performance at the final examination.

STATEMENT BY AUTHOR

This dissertation has been submitted in partial filfillment of requirements for an advanced degree at The University of Arizona and is deposited in the University Library to be made available to borrowers under rules of the Library.

Brief quotations from this dissertation are allowable without special permission, provided that accurate acknowledgment of source is made. Requests for permission for extended quotation from or reproduction of this manuscript in whole or in part may be granted by the head of the major department or the Dean of the Graduate College when in his judgment the proposed use of the material is in the interests of scholarship. In all other instances, however, permission must be obtained from the author.

SIGNED: Ross Brian Lockhart II

To Anne

and

Michael, Melinda, and Andrew

ACKNOWLEDGMENTS

The author wishes to extend his appreciation to the faculty, staff, and students of the Optical Sciences Center who provided assistance during the course of this program. Special thanks are due to the author's dissertation director, Dr. Jack D. Gaskill, for his continued encouragement and thorough review of the manuscript and to Dr. Roland V. Shack for his helpful suggestions and illuminating discussions.

The author is indebted to Janet Rowe for her efforts and patience in typing the numerous draft copies of this manuscript and to Martha Stockton and Kathy Seeley for their skillful preparation of the final manuscript.

This program was sponsored by the Rome Air Development Center, Griffiss AFB, New York, under Contract F30602-72-C-0392.

TABLE OF CONTENTS

TABLE OF CONTENTS--*Continued*

LIST OF ILLUSTRATIONS

List of Illustrations--*Continued*

List of Illustrations--*Continued*

List of Illustrations--*Continued*

List of Illustrations--*Continued*

LIST OF TABLES

ABSTRACT

The effect of optical aberrations on images formed by synthetic aperture optical systems is described in terms of the pupil function, the point spread function, and the transfer function. The synthetic aperture system considered is an array of six circular pupil elements positioned at equal intervals on a circle. The ratio of the synthesized pupil diameter to the diameter of each element is four. Six aberration forms--piston error (a constant phase shift across the pupil), tilt, defocus, spherical aberration, coma, and astigmatism--were introduced independently and in combinations into one pupil element of the array. In addition, system defocus, which affects all elements of the array, was introduced.

The aberrated pupil function was characterized by analytical expressions for the wavefront variance. The irradiance distribution of the point spread function, as well as the contrast and detail present in images of extended objects, was studied. The transfer function was calculated by computer for the case of small aberrations. For large aberrations the transfer function was determined experimentally by scanning the point spread function of a simulated synthetic aperture system, in which aberrations were introduced with an aberration generator.

It was found that piston error is the most sensitive aberration and has a pronounced effect when its magnitude is 0.25λ. For a magnitude of 0.1λ, piston error has a negligible effect. The synthetic aperture image is about equally sensitive to tilt, element defocus, and

system defocus. These aberrations do not produce a significant effect until their magnitudes are in the range of 0.25λ to 0.5λ. Spherical aberration, coma, and astigmatism are the least sensitive aberrations and are not significant until their magnitudes are nearly 1.0λ.

CHAPTER I

INTRODUCTION

Interest in applying synthetic aperture techniques to the optical region of the spectrum was stimulated by the Woods Hole Summer Study Program in 1967 (National Academy of Sciences, 1967). A large portion of this interest has been focused on applying dilute aperture techniques to the design of multiple aperture optical systems. Meinel (1970) proposed such a system for an infrared telescope, and since then a number of researchers have studied numerous aperture array configurations and image processing schemes (Boyce, 1971; Golay, 1971; Russell and Goodman, 1971; Reynolds and Cronin, 1970; Stockton, 1970; Shack, Rancourt, and Morrow, 1971; Shannon, Sanger, and Gray, 1971; Tschunko, 1971; Yansen, Reynolds, and Cronin, 1971).

In spite of the interest in dilute aperture techniques, no comprehensive examination has been made of the effects of optical aberrations on images formed by synthetic aperture systems. Aberrations have been considered only insofar as they describe the alignment and positioning of the elements for a few particular array configurations (Jain, 1971; Kishner, 1971; Yansen et al., 1972). In order to establish tolerances and make image quality predictions, it is necessary to understand how synthetic aperture images are affected by all aberrations that are likely to occur.

In this study the effects of aberrations on a six-element synthetic-aperture array are investigated. (This array is the one originally proposed by Meinel, and it is being used for the Multi-Mirror Telescope presently under construction at the Optical Sciences Center, The University of Arizona--see Meinel et al., 1972; Sanger, Hoffman, and Reed, 1972; Weymann and Carlton, 1972; Sanger and Shannon, 1973.) For most of the investigations a single element of the six-aperture array is aberrated with piston error, tilt, defocus, spherical aberration, coma, or astigmatism, or combinations thereof, but in one case all elements are aberrated with system defocus. The aberration effects are viewed in terms of the pupil function, point spread function, transfer function, and images of an extended object. The effects are correlated in order to draw conclusions about (1) the relative sensitivity to the aberrations and (2) the tolerable magnitude of the aberrations.

Chapter II gives the mathematical formulation of the pupil function, spread function, and transfer function for the synthetic aperture array. Chapter III describes a computer program used to calculate the transfer function from the pupil function. Chapter IV gives a detailed discussion of the experimental techniques and equipment used to simulate an aberrated synthetic aperture system, to measure the transfer function, and to photograph the point spread function and extended target images. The results of the computer simulation and the experimental measurements are presented in Chapter V, and the results are interpreted and correlated in Chapter VI.

CHAPTER II

THEORY

The imaging characteristics of unaberrated and aberrated synthetic-aperture systems will be considered in this chapter in terms of the properties of their pupil functions, point spread functions, and optical transfer functions, descriptors that complement each other and offer insight into the nature of images formed by such systems. The analytic results obtained in this chapter will be used with the experimental results discussed later to draw conclusions about the significance of specific aberrations on the image-forming properties of synthetic-aperture systems.

Pupil Function

The pupil function of an optical system describes the amplitude and phase variations that exist across the system's pupil. In general, the pupil function may be expressed as

$$P(\rho,\phi) = p(\rho,\phi)e^{ikW(\rho,\phi)} \tag{1}$$

where $k = 2\pi/\lambda$, $p(\rho,\phi)$ defines the boundary of the pupil and any amplitude variations across it, and $W(\rho,\phi)$ describes the phase variations across the pupil (see Fig. 1).

The wave aberration function, $W(\rho,\phi)$, may be expressed as a power series expansion in terms of ρ, β, and ϕ (Born and Wolf, 1965, pp. 466-473), where β is the angular field position.

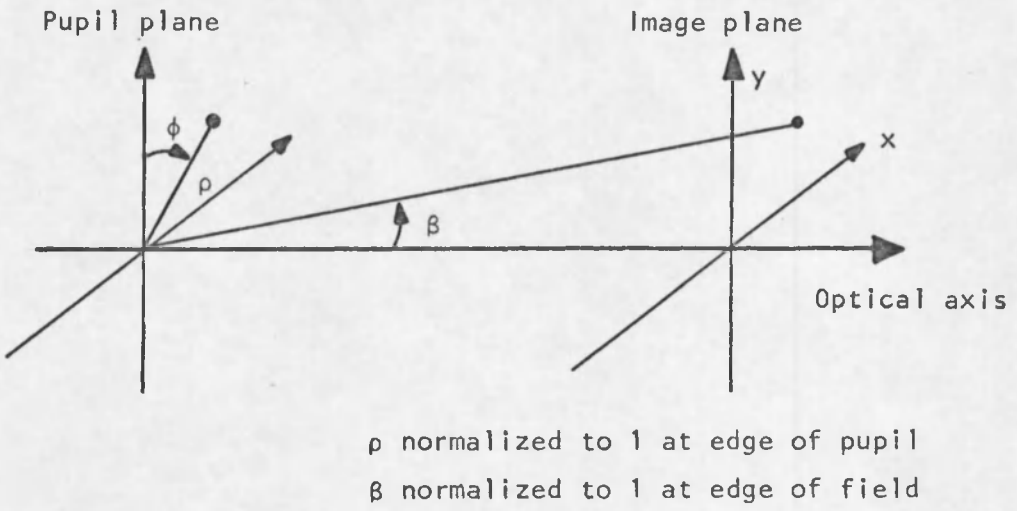

Fig. 1. Coordinate System for the Aberration Expansion.

If the system being considered has circular symmetry, only certain terms in the expansion are allowed. For such a case, the expansion may be written

$$\begin{aligned} W(\rho,\phi) = {} & W_{000} + W_{200}\beta^2 + W_{020}\rho^2 + W_{111}\beta\rho\cos\phi \\ & + W_{040}\rho^4 + W_{131}\beta\rho^3\cos\phi + W_{222}\beta^2\rho^2\cos^2\phi \\ & + W_{220}\beta^2\rho^2 + W_{311}\beta^3\rho\cos\phi + W_{400}\beta^4 \end{aligned} \tag{2}$$

where the coefficients W_{XYZ} are called aberration coefficients and indicate the maximum phase variation in the pupil due to a particular aberration. (X, Y, and Z denote the powers to which the β, ρ, and $\cos\phi$ factors are raised, respectively.)

The field dependence (β) of the aberrations will not be considered in this study. Several of the aberration terms in Eq. (2) have the same pupil dependence and reduce to the same form when the field dependence is ignored. W_{000}, $W_{200}\beta^2$, and $W_{400}\beta^4$ reduce to W_{00}, which is

called piston error. Magnification error ($W_{111}\beta\rho\cos\phi$) and distortion ($W_{311}\beta^3\rho\cos\phi$) reduce to $W_{11}\rho\cos\phi$, which is called tilt. Defocus ($W_{020}\rho^2$) and field curvature ($W_{220}\beta^2\rho^2$) reduce to $W_{20}\rho^2$, which is called defocus. After dropping the β dependence, the aberration terms of interest reduce to

W_{00}	Piston error
$W_{20}\rho^2$	Focal error (defocus)
$W_{11}\rho\cos\phi$	Tilt
$W_{40}\rho^4$	Spherical aberration
$W_{31}\rho\cos\phi$	Coma
$W_{22}\rho^2\cos^2\phi$	Astigmatism

The orientations of the three nonrotationally symmetric aberrations tilt, coma, and astigmatism are fixed when ϕ is measured with respect to the y axis (Fig. 1). However, ϕ can be measured with respect to an arbitrary axis by substituting $\phi + \alpha$ for ϕ in the wavefront aberration expansion, Eq. (2). In this case, the aberration is said to be oriented at an angle α.

The significance of these aberrations on circularly symmetric, single-aperture systems has been discussed in detail elsewhere (Born and Wolf, 1965) and will not be covered here.

Wavefront Variance

For a multiple-element pupil, the pupil function may be written as the sum of the component pupil functions. In cartesian coordinates we have

$$P(v,u) = \sum_{m=1}^{N} p_m(v - v_m \quad u - u_m)\ e^{ikW_m(v - v_m,\ u - u_m)},$$

where v_m, u_m are the coordinates of the center of the mth pupil element. Here the wave aberration function, Eq. (2), is centered on an individual aperture element. In addition, if all pupil elements are affected by an aberration function, $W'(v,u)$, which extends over the entire synthesized pupil, then the pupil function becomes

$$P(v,u) = \left(\sum_{m=1}^{N} p_m(v - v_m,\ u - u_m)\ e^{ikW_m(v-v_m,u-u_m)} \right) \cdot e^{ikW'(v,u)}. \tag{3}$$

This study is concerned primarily with the effects of individual element aberrations. Therefore, except in cases where the focus of the entire array is altered, $W'(v,u)$ will be set equal to zero.

The variance, σ^2, of a wavefront is defined as the mean of the squared wavefront error minus the squared mean of the wavefront error

$$\sigma^2 = \frac{1}{A}\iint_A W^2 dA - \left(\frac{1}{A}\iint_A W dA\right)^2,$$

where A is the area of the pupil and W is the wave aberration function. It provides a convenient characterization of a wavefront with a single number. For a synthetic aperture array of N identical elements of the same shape and size having one aberrated aperture element, the variance σ^2 may be written as

$$\sigma^2 = \frac{1}{N\pi}\int_{\phi=0}^{2\pi}\int_{\rho=0}^{1} W^2(\rho,\phi)\rho d\rho d\phi - \left(\frac{1}{N\pi}\int_0^{2\pi}\int_0^{1} W(\rho,\phi)\rho d\rho d\phi\right)^2, \tag{4}$$

where $N\pi$ is the normalized area of the synthetic aperture and ρ,ϕ are coordinates whose origin is at the center of the aberrated pupil element. When the aberration terms are substituted into Eq. (4) and the integrations are performed, the following expressions are obtained:

$$\sigma^2 = \frac{N-1}{N^2} W_{00}^2 \qquad \text{Piston error}$$

$$\sigma^2 = \frac{1}{4N} W_{11}^2 \qquad \text{Tilt}$$

$$\sigma^2 = \frac{4N-3}{12N^2} W_{20}^2 \qquad \text{Focal error}$$

$$\sigma^2 = \frac{9N-5}{45N^2} W_{40}^2 \qquad \text{Spherical aberration}$$

$$\sigma^2 = \frac{1}{8N} W_{31}^2 \qquad \text{Coma}$$

$$\sigma^2 = \frac{2N-1}{16N^2} W_{22}^2 \qquad \text{Astigmatism}$$

The variance is plotted as a function of the number of aperture elements N in Fig. 2 for each of the aberrations. The effect of piston error is far more significant than any of the other aberrations in multi-element systems. For $N = 6$, the array size used in this study, piston error has a variance three times greater than any of the other aberrations. Defocus and tilt are the next most significant aberrations and have approximately twice the variance of spherical aberration, coma, or astigmatism.

In many cases it is desirable to balance one aberration against another to reduce the variance and thereby improve the quality of the image. The optimum balance is defined to be that which minimizes the

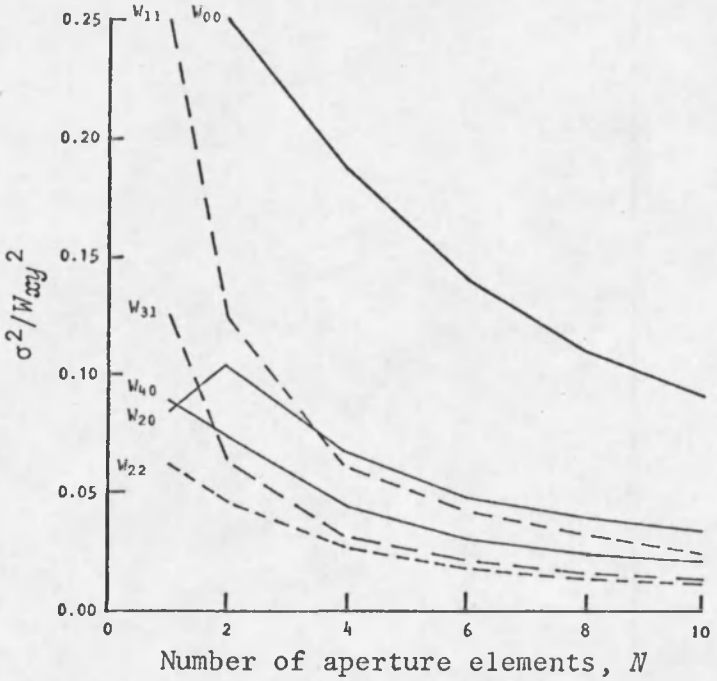

Fig. 2. Variance When One Element of an N-Element Array Is Aberrated.

variance. In this study, defocus was used to balance spherical aberration, astigmatism, and piston error. The general expressions for the variance of the balanced aberrations are given below. First, when piston error is balanced with defocus, the variance is given by

$$\sigma^2 = \frac{N-1}{N^2} W_{00}^2 + \frac{N-1}{N^2} W_{00}W_{20} + \frac{4N-3}{12N^2} W_{20}^2.$$

When spherical aberration is balanced with defocus, we have

$$\sigma^2 = \frac{4N-3}{12N^2} W_{20}^2 + \frac{3N-2}{6N^2} W_{20}W_{40} + \frac{9N-5}{45N^2} W_{40}^2.$$

Finally, when astigmatism is balanced with defocus, we have

$$\sigma^2 = \frac{2N-1}{16N^2} W_{22}^2 + \frac{4N-3}{12N^2} W_{20}W_{22} + \frac{4N-3}{12N^2} W_{20}^2.$$

If the variance is minimized with respect to the balancing aberration, the optimum magnitude of the balancing aberration is found. The optimum balance is then substituted into the expressions above to find the optimum variance. When piston error is balanced with optimum defocus, then

$$W_{20} = -\frac{6(N-1)}{4N-3} W_{00}$$

$$\sigma^2 = \left[\frac{N-1}{N^2} - \frac{3(N-1)^2}{N^2(4N-3)}\right] {W_{00}}^2.$$

If spherical aberration is balanced with optimum defocus, we have

$$W_{20} = -\left(\frac{3N-2}{4N-3}\right) W_{40}$$

$$\sigma^2 = \left[\frac{-(3N-2)^2}{12N^2(4N-3)} + \frac{9N-5}{45N^2}\right] {W_{40}}^2.$$

Finally, for astigmatism balanced with optimum defocus, we have

$$W_{20} = -\frac{1}{2} W_{22}$$

$$\sigma^2 = \frac{N+1}{8N^2} {W_{22}}^2.$$

The optimum magnitude of the balancing aberration varies with the number of aperture elements for spherical aberration/defocus and piston error/defocus, but not for astigmatism/defocus. This dependence is shown in Fig. 3. Whereas the optimum magnitude of the balancing aberration depends upon the number of aperture elements for a small number of elements, it does not change significantly when $N > 4$.

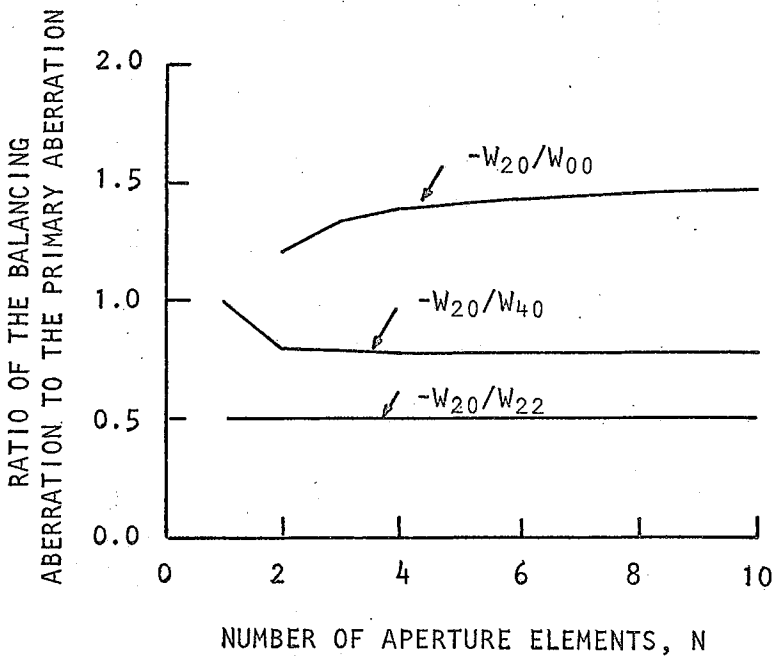

Fig. 3. Optimum Balancing of Aberrations.

In Figs. 4 through 6, the variance is plotted as a function of the number of elements for the unbalanced and optimumly balanced cases. From these curves it is apparent that the effect of piston error can be significantly reduced by introducing an appropriate amount of defocus. For $N = 6$, the variance is reduced by 70% when the piston error is balanced with defocus (Fig. 4). Balancing spherical aberration with defocus is particularly effective in reducing the variance (Fig. 5); balancing astigmatism with defocus produces only a moderate reduction (Fig. 6).

The variance is a convenient device for characterizing the errors in a wavefront. However, in order to attribute meaning to the variance as a tool for image evaluation, it is necessary to correlate the variance with image quality. Rayleigh established the foundation for this

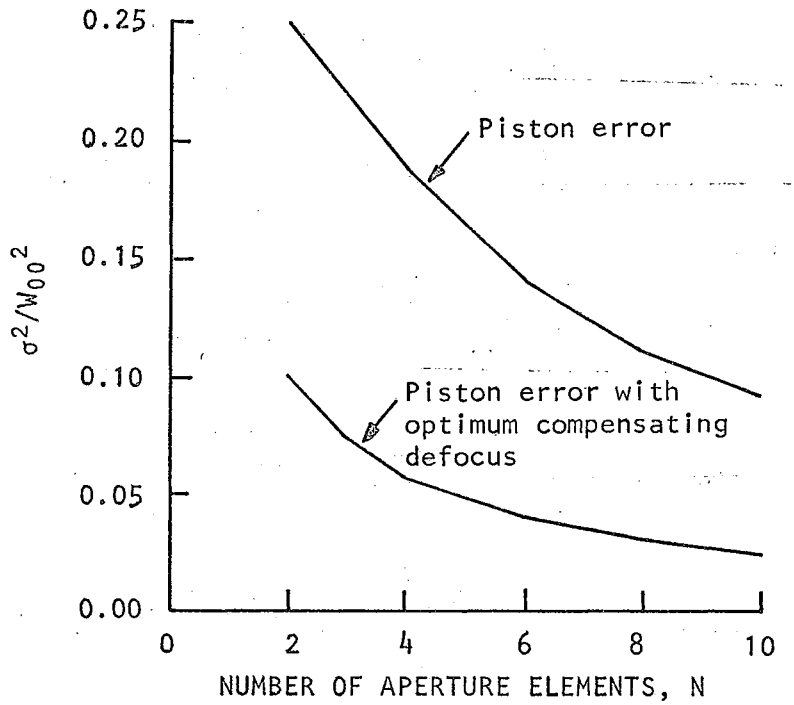

Fig. 4. Effect on Variance When Piston Error Is Balanced with Defocus.

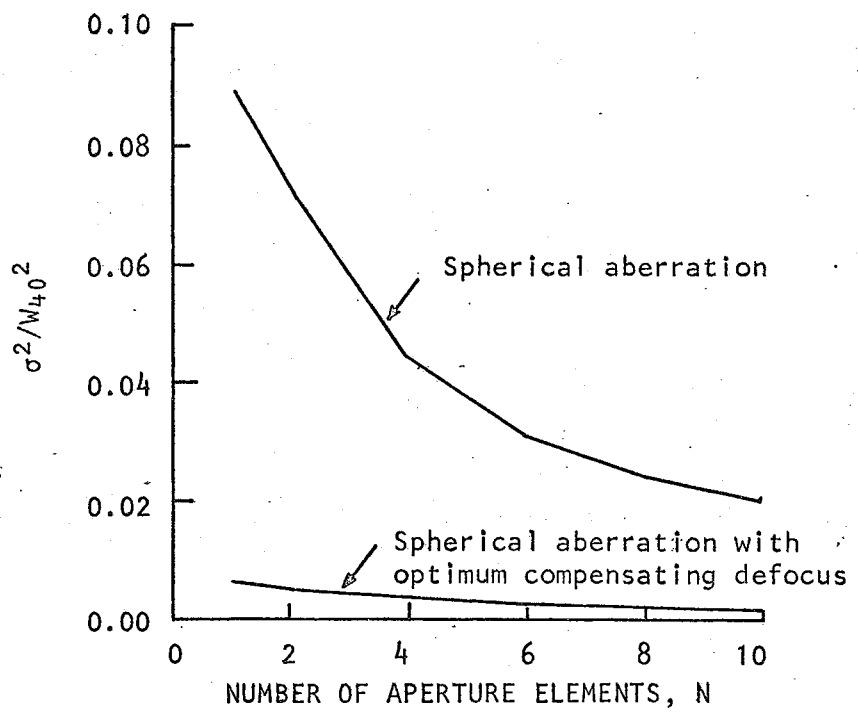

Fig. 5. Effect on Variance When Spherical Aberration Is Balanced with Defocus.

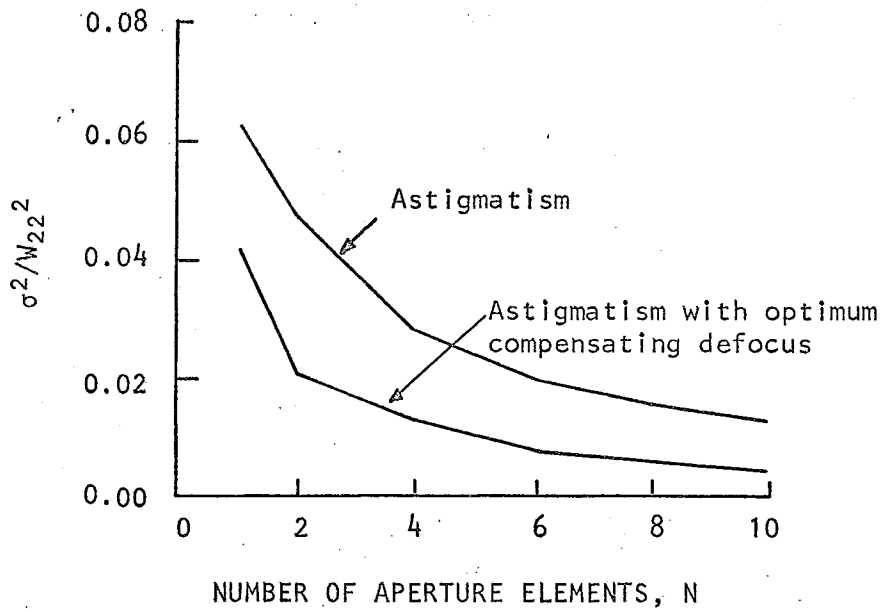

Fig. 6. Effect on Variance When Astigmatism Is Balanced with Defocus.

correlation by showing that a quarter wave of spherical aberration did not produce a significant degradation of an image (Born and Wolf, 1965, p. 468). The variance corresponding to $\lambda/4$ of spherical aberration for a single aperture element is $0.0055\lambda^2$ (see Fig. 5). Therefore, we can establish, with a few reservations (Born and Wolf, 1965, p. 468), the criterion that a wavefront must have a variance of less than $0.0055\lambda^2$ in order to produce an effectively unaberrated image.

This criterion and the curves in Figs. 2 through 6 suggest that the amounts of aberration that can be tolerated in a single element of a siz-element array are as listed in Table 1.

Table 1. Tolerable Amounts of Aberration.

Aberration	W_{XY} $N = 1$	W_{XY} $N = 6$
Piston	--	0.14λ
Tilt	--	0.36λ
Defocus	0.25λ	0.33λ
Spherical aberration	0.24λ	0.42λ
Astigmatism	0.29λ	0.53λ
Coma	0.21λ	0.51λ
Piston + defocus	--	0.5λ
Spherical aberration + defocus	0.98λ	1.7λ
Astigmatism + defocus	0.36λ	0.88λ

System Defocus. When an unaberrated synthetic aperture system is defocused, Eq. (3) reduces to

$$P(v,u) = e^{ikW'(v,u)} \sum_{m=1}^{N} p_m(v-v_m,\ u-u_m),$$

where $W'(v,u)$ is the wave aberration function for defocus. For an array of identical aperture elements positioned on a circle, the wavefront error across each element is the same, except for orientation. Since the variance is independent of the orientation of the aberration, all aperture elements in this case have the same variance. Therefore, the variance of the array equals just the variance of an aperture element.

The variance can be calculated by substituting the wavefront error across a pupil element for $W(\rho,\phi)$ in Eq. (4). The integration is straightforward and yields

$$\sigma^2 = \left[\frac{a^4}{12} + a^2(1-a)^2\right] W'_{20}{}^2,$$

where a is the radius of an aperture element normalized to the radius of the synthesized aperture, and W'_{20} is the wavefront error at the edge of the synthesized aperture. In this study, $a = 0.25$. Therefore,

$$\sigma^2 = 0.035\, W'^2_{20}.$$

The system defocus that produces a variance of $0.005\lambda^2$ (the criterion established above) is 0.39λ.

Point Spread Function

The pupil function associated with an aberrated synthetic aperture system consisting of N aperture elements (Fig. 7) can be expressed as

$$P(v,u) = \sum_{m=1}^{N} p_m(v-v_m,\ u-u_m)\, e^{ikW_m(v-v_m,u-u_m)},$$

where $p_m(v-v_m,\ u-u_m)$ describes the amplitude transmission of the mth aperture centered at $v = v_m$ and $u = u_m$, and where $W_m(v-v_m,\ u-u_m)$ is the wave aberration function associated with the mth aperture.

The amplitude spread function is the Fourier transform of the pupil function

$$\begin{aligned} A(x,y) &= \mathcal{F}[P(v,u)] \\ &= \mathcal{F}\left[\sum_{m=1}^{N} p_m(v-v_m,\ u-u_m)\, e^{ikW_m(v-v_m,u-u_m)}\right] \\ &= \sum_{m=1}^{N} \mathcal{F}\left[p_m(v-v_m,\ u-u_m)\, e^{ikW_m(v-v_m,u-u_m)}\right]. \end{aligned}$$

Using the Fourier transform shift theorem, this expression becomes

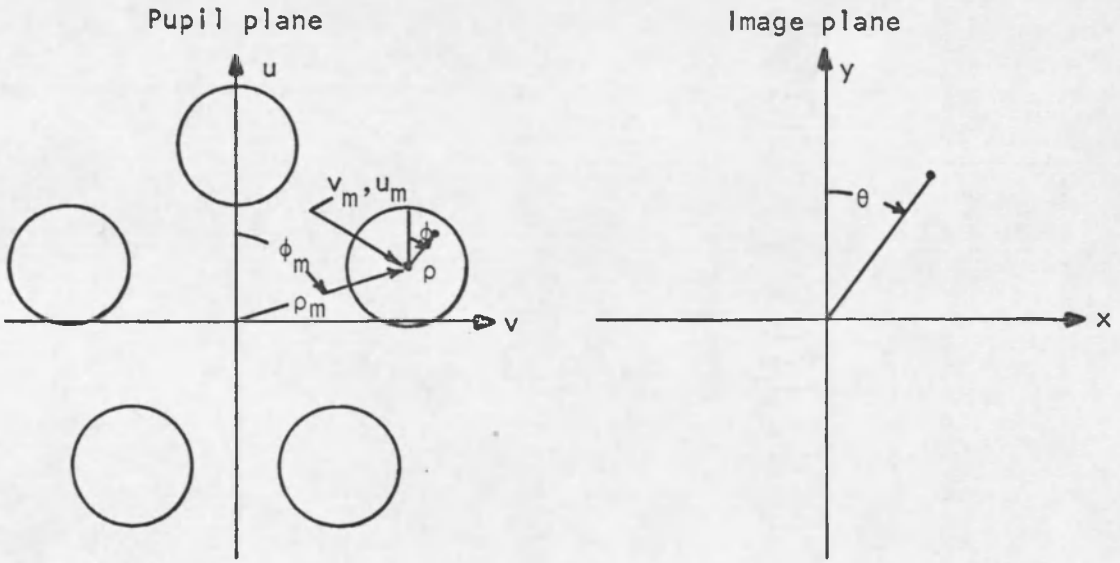

Fig. 7. Coordinates Describing Synthetic Aperture Array and Image Plane.

$$A(x,y) = \sum_{m=1}^{N} e^{-ik(xv_m/f + yu_m/f)} \mathcal{F}\{p_m(v,u)e^{ikW_m(v,u)}\},$$

where f is the focal length of the system. Using

$$x = r\sin\theta, \qquad v_m = \rho_m\sin\phi_m,$$

$$y = r\cos\theta, \qquad u_m = \rho_m\cos\phi_m,$$

the equation for $A(x,y)$ can be expressed in polar coordinates

$$A'(r,\theta) = \sum_{m=1}^{N} \exp[(-ikr\rho_m/f)(\sin\theta\sin\phi_m + \cos\theta\cos\phi_m)] \circ \mathcal{F}'\{p_m(\rho,\phi)\exp[ikW_m(\rho,\phi)]\},$$

where $\mathcal{F}'\{\}$ is the Fourier transformation operator corresponding to polar coordinates. We can also write

$$A'(r,\theta) = \sum_{m=1}^{N} a_m(r,\theta)U_m(r,\theta), \tag{5}$$

where

$$a_m(r,\theta) = \exp[(-ikr\rho_m/f)(\sin\theta\sin\phi_m + \cos\theta\cos\phi_m)]$$

$$U_m(r,\theta) = \mathcal{F}'\{p_m(\rho,\phi)\exp[ikW_m(\rho,\phi)]\}.$$

That is, the amplitude spread function of an N-element synthetic aperture system is the sum of N terms. Each term is the product of the amplitude spread function associated with a particular aperture element, $U_m(r,\theta)$, times a phase factor that depends on the position of the aperture element within the synthetic aperture array.

The phase factor, $a_m(r,\theta)$, can be evaluated easily once the synthetic aperture array is specified. Evaluating $U_m(r,\theta)$ is much more difficult and can be done only for simple forms of $W_m(\rho,\phi)$, or by the use of restrictive approximations (Born and Wolf, 1965, p. 474). If it is assumed that the aberrations will be less than $\lambda/4$, then $e^{ikW_m(\rho,\phi)}$ can be expanded in a power series and the Fourier transform integrations are easily performed. However, the results of the variance calculations presented in Table 1 show that most of the aberrations do not have a noticeable effect until their magnitude is about $\lambda/2$. Consequently, the small aberration approximation is not appropriate, and $U_m(r,\theta)$ cannot be easily evaluated.

For a synthetic aperture array consisting of N aperture elements positioned on a circle of radius ρ_m, the amplitude spread function is given by Eq. (5), where $\phi_m = m(2\pi/N)$. If $N = 6$, then $\phi_m = \pi m/3$ and the amplitude spread function becomes

$$A'(r,\theta) = \sum_{m=1}^{6} \exp\left[(-ikr\rho_m/f)\left(\sin\theta\sin\frac{\pi m}{3} + \cos\theta\cos\frac{\pi m}{3}\right)\right] \circ \mathcal{F}'\left\{ p_m(\rho,\phi)\, \exp[ikW_m(\rho,\phi)] \right\}. \quad (6)$$

Unaberrated System

If all aperture elements are identical, free of aberrations, and of radius a, the individual amplitude spread functions, $a_m(r,\theta)$, are equal and, for circular aperture elements, are given by (Born and Wolf, 1965, p. 395)

$$U(r,\theta) = -i\,\frac{2\pi a^2}{\lambda f}\,\frac{J_1[(ka/f)r]}{(ka/f)r}\,. \quad (7)$$

The amplitude spread function for the six-element array then becomes

$$A'(r,\theta) = a(r,\theta) \sum_{m=1}^{6} \exp\left[(-ikr\rho_m/f)\left(\sin\theta\sin\frac{\pi m}{3} + \cos\theta\cos\frac{\pi m}{3}\right)\right]$$

$$= -i\,\frac{2\pi a^2}{\lambda f}\,\frac{J_1[(ka/f)r]}{(ka/f)r}\left\{\exp\left[-j\,\frac{kr\rho_m}{f}\left(\frac{\sqrt{3}}{2}\sin\theta + \frac{1}{2}\cos\theta\right)\right]\right.$$

$$+ \exp\left[-j\,\frac{kr\rho_m}{f}\left(\frac{\sqrt{3}}{2}\sin\theta - \frac{1}{2}\cos\theta\right)\right]$$

$$+ \exp\left[-j\,\frac{kr\rho_m}{f}\left(-\frac{\sqrt{3}}{2}\sin\theta - \frac{1}{2}\cos\theta\right)\right]$$

$$+ \exp\left[-j\,\frac{kr\rho_m}{f}\left(-\frac{\sqrt{3}}{2}\sin\theta + \frac{1}{2}\cos\theta\right)\right]$$

$$\left. + \exp\left(-j\,\frac{kr\rho_m}{f}\cos\theta\right) + \exp\left(+j\,\frac{kr\rho_m}{f}\cos\theta\right)\right\} .$$

Making use of the relationships between exponential and trigonometric forms, this equation reduces to

$$A'(r,\theta) = -i\,\frac{2\pi a^2}{\lambda f}\,\frac{J_1[(ka/f)r]}{(ka/f)r}\left\{2\cos[(kr\rho_m/f)\cos\theta]\right.$$

$$+ 2\cos\left[(kr\rho_m/f)\left(\frac{\sqrt{3}}{2}\sin\theta + \frac{1}{2}\cos\theta\right)\right]$$

$$\left. + 2\cos\left[(kr\rho_m/f)\left(\frac{\sqrt{3}}{2}\sin\theta - \frac{1}{2}\cos\theta\right)\right]\right\} . \qquad (8)$$

Finally, the point spread function is

$$\mathrm{PSF}(r,\theta) = |A'(r,\theta)|^2$$

$$= \frac{4\pi^2 a^4}{\lambda^2 f^2}\left(\frac{J_1[(ka/f)r]}{(ka/f)r}\right)^2\left\{6 + 2\cos[(2kr\rho_m/f)\cos\theta]\right.$$

$$+ 2\cos[(kr\rho_m/f)(\sqrt{3}\sin\theta + \cos\theta)]$$

$$\left. + 2\cos[(kr\rho_m/f)(\sqrt{3}\sin\theta - \cos\theta)]\right\} \qquad \text{(continued)}$$

$$+ 4\cos\left[(kr\rho_m/f)\left(\frac{\sqrt{3}}{2}\sin\theta + \frac{3}{2}\cos\theta\right)\right]$$

$$+ 4\cos\left[(kr\rho_m/f)\left(\frac{\sqrt{3}}{2}\sin\theta - \frac{1}{2}\cos\theta\right)\right]$$

$$+ 4\cos\left[(kr\rho_m/f)\left(\frac{\sqrt{3}}{2}\sin\theta + \frac{1}{2}\cos\theta\right)\right]$$

$$+ 4\cos\left[(kr\rho_m/f)\left(\frac{\sqrt{3}}{2}\sin\theta - \frac{3}{2}\cos\theta\right)\right]$$

$$+ 4\cos\left[(kr\rho_m/f)(\sqrt{3}\sin\theta)\right]$$

$$+ 4\cos\left[(kr\rho_m/f)\cos\theta\right]\Bigg\}. \qquad (9)$$

The point spread function is represented in Eq. (9) by an Airy pattern modulated by nine cosine fringe fields. The orientation and magnitude of each of the fringe fields are characteristic of the array but are independent of the size and shape of the individual aperture elements. The fringe fields have spatial periods that are smaller than the Airy disk diameter, and when superimposed they form a complicated pattern having a central peak smaller than that of the Airy disk; the larger the ratio ρ_m/f, the smaller the width of the central peak.

Aberrated System

When an aperture element is aberrated, the amplitude spread function of that element is not the same as the amplitude spread function of the other elements, and Eq. (5) cannot be reduced to the simple form of Eq. (6). In general, the aberrated point spread function is extremely complex and difficult to express in analytic form.

However, for some aberrations it is possible to obtain expressions for the central ordinate value of the spread function. This

quantity is of interest because it indicates, to some extent, the amount of information passed by the optical system. A commonly-used criterion is stated as follows: As long as the value of the central ordinate of the point spread function is caused to decrease by less than 20%, there will be no significant degradation of the image.

Piston Error. When piston error is present in an aperture element, the amplitude spread function associated with that element is

$$U_A(r) = \mathscr{F}' \left\{ \text{circ}(r/a) \exp(ikW_{00}) \right\} ,$$

where a is element radius and W_{00} is the amount of piston error in waves. This can also be written

$$U_A(r) = \exp(ikW_{00}) \mathscr{F}' \left\{ \text{circ}(r/a) \right\} .$$

Using Eq. (7),

$$U_A(r) = -i \frac{2\pi a^2}{\lambda f} \exp(ikW_{00}) \frac{J_1[(ka/f)r]}{(ka/f)r} .$$

When the last expression is substituted into Eq. (5) and the point spread function is calculated and then evaluated at $r = 0$, one finds that

$$\text{PSF}(0,0) = \left\{ [N^2 - 2(N-1)] + 2(N-1)\cos(kW_{00}) \right\} \frac{\pi^2 a^4}{\lambda^2 f^2} .$$

The final expression is obtained by normalizing the last equation to the central ordinate for an unaberrated image:

$$\text{PSF}_N(0,0) = 1 - [2(N-1)/N^2][1 - \cos(kW_{00})]. \qquad (10)$$

This expression is valid for any array of N elements having the same size and shape but where one element is aberrated.

The introduction of piston error into one element produces a reduction of the central value of the point spread function that varies sinusoidally as the piston error increases (Fig. 8). The maximum reduction occurs when $W_{00} = \lambda/2, 3\lambda/2$, etc., and there is no reduction when $W_{00} = \lambda, 2\lambda$, etc. The magnitude of this effect depends on the total number of apertures, as shown in Fig. 9. With one aperture element there is no reduction; with two elements the reduction is a maximum.

Using Eq. (10), we can determine the amount of piston error, as a function of N, that will produce a 20% reduction in the point spread function central value. This function, which is plotted in Fig. 10, establishes a tolerance for piston error.

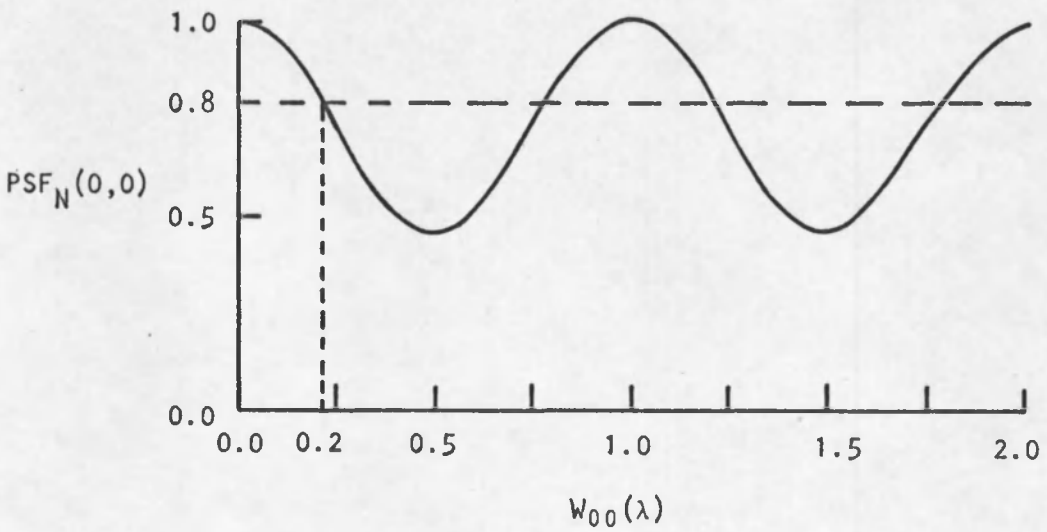

Fig. 8. Central Value of Point Spread Function in Presence of Piston Error ($N = 6$).

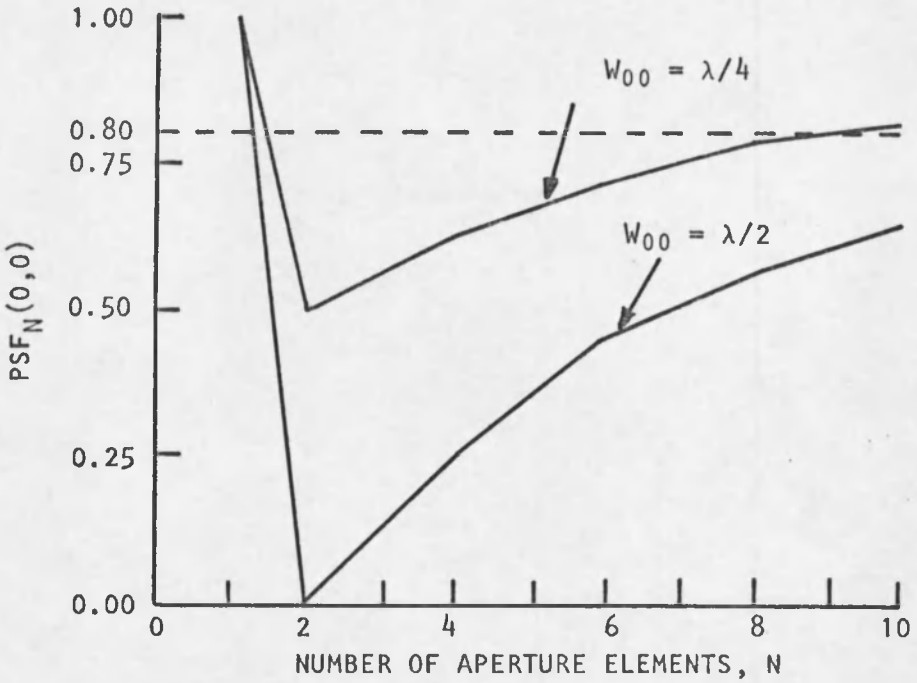

Fig. 9. Effect of Piston Error as Number of Aperture Elements Increases.

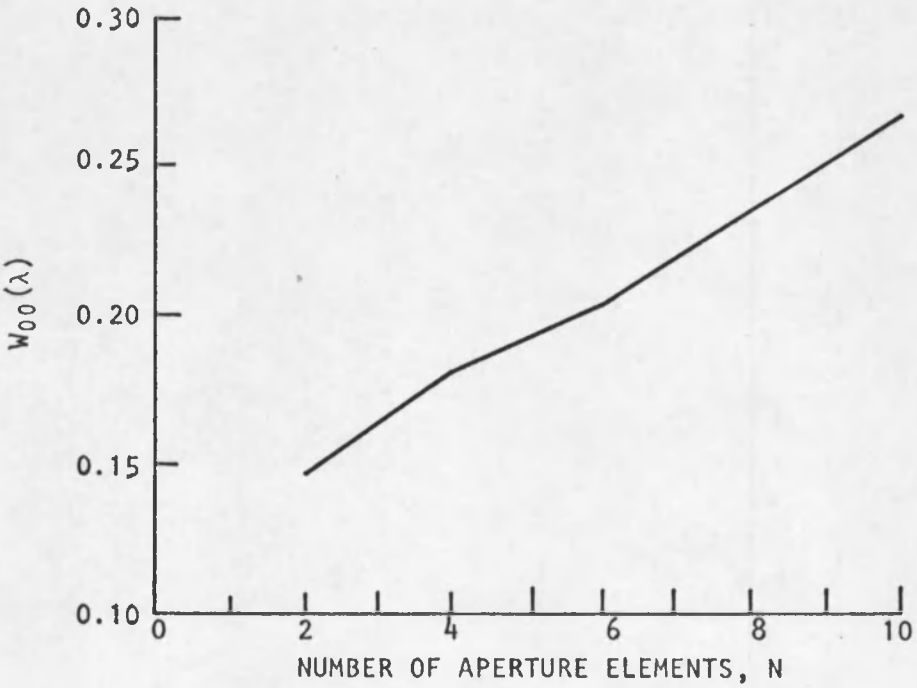

Fig. 10. Piston Error in One Element That Produces a Reduction of 20% in the Central Value of the Point Spread Function.

The array of primary concern in the present study has six identical elements located on a circle. For this array the normalized central value of the point spread function drops to 0.72 and 0.45 for $\lambda/4$ and $\lambda/2$ of piston error, respectively (Fig. 9). A 20% reduction in the point spread function central value occurs when $W_{00} = 0.2\lambda$.

Tilt. The introduction of wavefront tilt into one aperture element causes the spread function associated with that element to shift in position. The magnitude of the shift, δ, is

$$\delta = (\lambda f/a)W_{11},$$

where W_{11} is the tilt aberration coefficient in units of wavelength, a is the element radius, and f is the system focal length.

A spread function shifted along the y axis is [see Eq. (7)] expressed as

$$U_A'(x,y) = -i\frac{2\pi a^2}{\lambda f}\frac{J_1\frac{ka}{f}\left[x^2+\left(y-\frac{W_{11}\lambda f}{a}\right)^2\right]^{\frac{1}{2}}}{\frac{ka}{f}\left[x^2+\left(y-\frac{W_{11}\lambda f}{a}\right)^2\right]^{\frac{1}{2}}}.$$

Evaluating $U_A'(x,y)$ at the origin yields

$$U_A'(0,0) = -i\frac{2\pi a^2}{\lambda f}\frac{J_1(2\pi W_{11})}{2\pi W_{11}}.$$

Although the last expression was derived for a shift along the y axis, it is valid for a shift in any direction as long as the spread function has circular symmetry.

The value of an unaberrated amplitude spread function at the origin is

$$U(0,0) = -i\,\frac{2\pi a^2}{\lambda f}\,(0.5).$$

Combining N-1 unaberrated aperture elements and one aberrated aperture element gives

$$U_{\text{total}}(0,0) = -i\,\frac{2\pi a^2}{\lambda f}\,\frac{J_1(2\pi W_{11})}{2\pi W_{11}} - i\,\frac{2\pi a^2}{\lambda f}\,(0.5)(N\text{-}1),$$

and the central value of the point spread function is therefore

$$\text{PSF}(0,0) = \left(\frac{2\pi a^2}{\lambda f}\right)^2\left[\frac{J_1(2\pi W_{11})}{2\pi W_{11}} + (0.5)(N\text{-}1)\right]^2.$$

When normalized by the unaberrated central value of $N^2(2\pi a^2/\lambda f)(0.5)^2$, the last equation becomes

$$\text{PSF}_N(0,0) = \frac{4}{N^2}\left[\frac{J_1(2\pi W_{11})}{2\pi W_{11}} + (0.5)(N\text{-}1)\right]^2. \qquad (11)$$

The introduction of tilt into one aperture element produces a decrease in $\text{PSF}_N(0,0)$ as shown in Fig. 11. When $W_{11} > 0.5\lambda$, there is very little contribution from the aberrated pupil; hence, there is no further reduction in $\text{PSF}_N(0,0)$ for larger values of W_{11}. In Fig. 12, the dependence of $\text{PSF}_N(0,0)$ on the number of array elements is shown for two values of W_{11}. In Fig. 13, the amount of tilt that produces a 20% decrease in $\text{PSF}_N(0,0)$ is shown as a function of the number of array elements.

For a six-element array, $\text{PSF}_N(0,0)$ is reduced to 0.9 and 0.75 for tilt errors of 0.25λ and 0.5λ, respectively, and drops to 80% of its maximum value when $W_{11} = 0.4\lambda$.

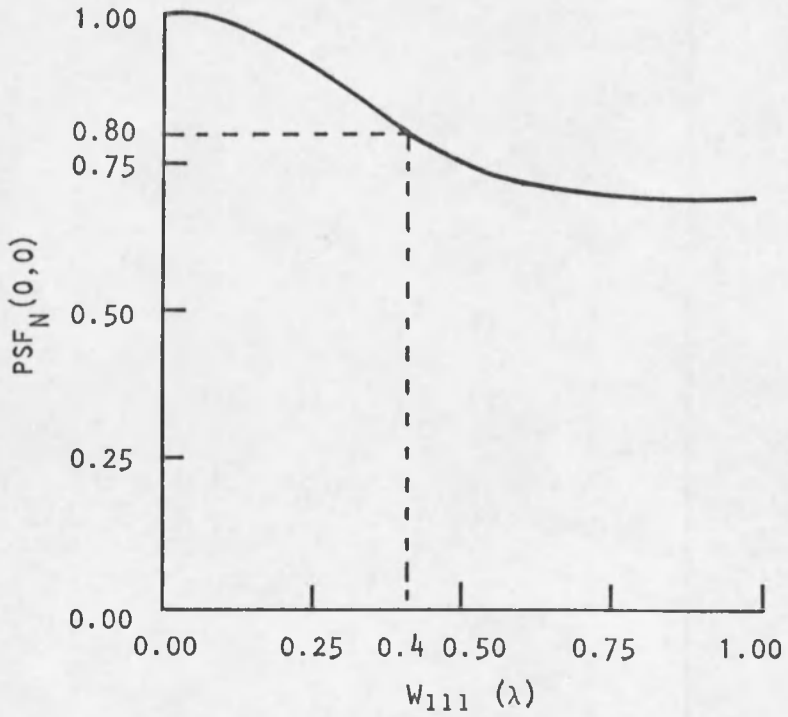

Fig. 11. Central Value of the Point Spread Function in the Presence of Tilt ($N = 6$).

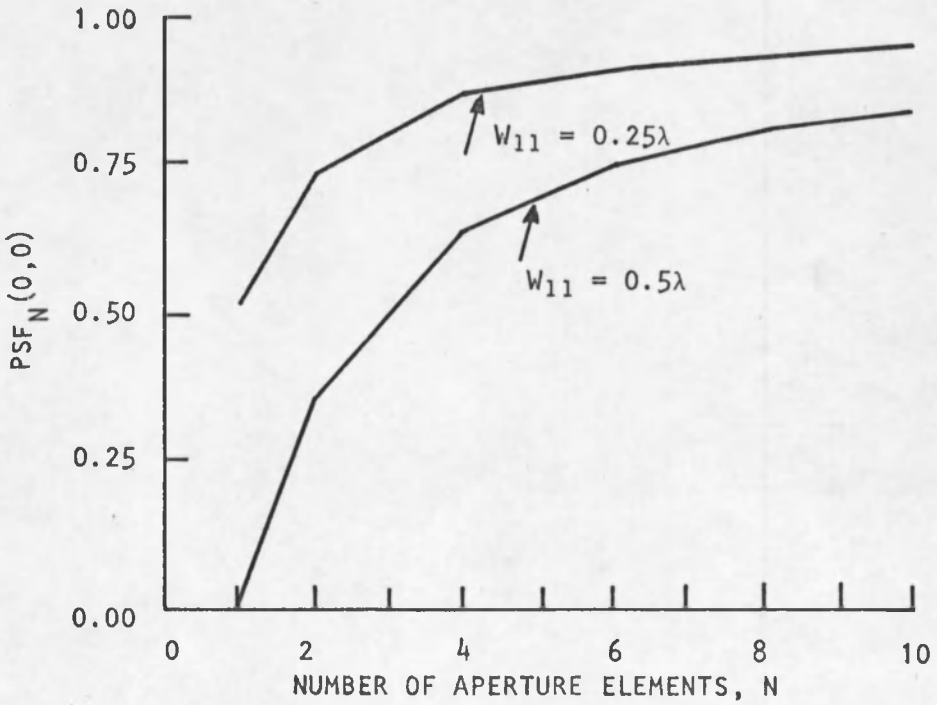

Fig. 12. Effect of Tilt as the Number of Aperture Elements Increases.

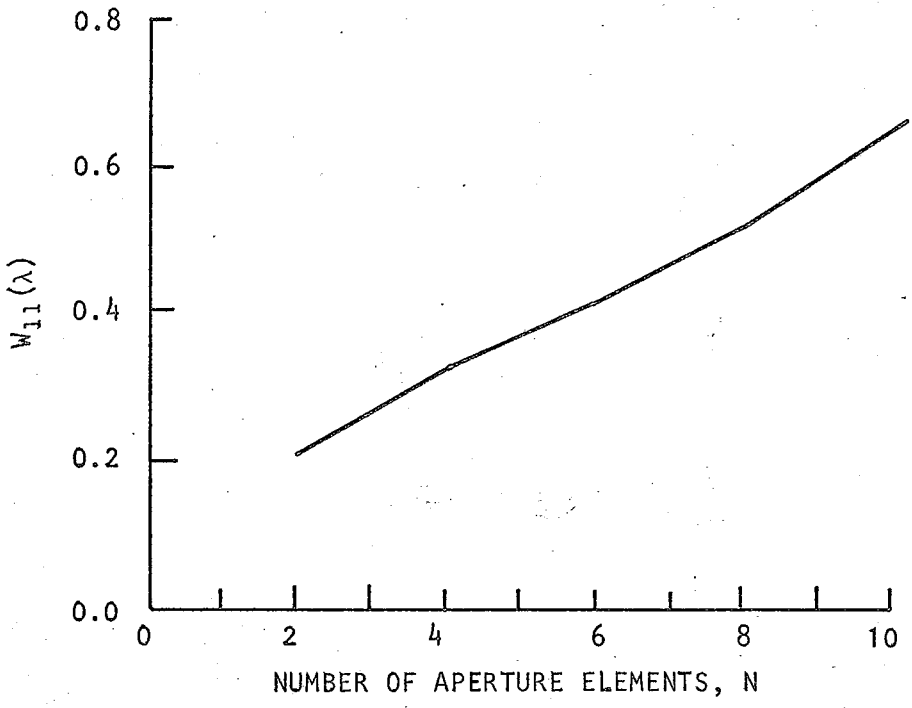

Fig. 13. Tilt in One Element That Produces a Reduction of 20% in the Central Value of the Point Spread Function.

Optical Transfer Function

The optical transfer function (OTF) of an optical system is equal to the normalized autocorrelation of its pupil function (Goodman, 1968, p. 116)

$$\mathrm{OTF}(\nu_v, \nu_u) = \frac{\iint_{-\infty}^{\infty} P(v - \lambda f \nu_v,\ u - \lambda f \nu_u) P(v,u)\, dv\, du}{\iint_{-\infty}^{\infty} P(v,u)\, dv\, du} . \qquad (12)$$

In general, $P(v,u)$ is a complicated function, and Eq. (12) is difficult to evaluate. The modulus of $\mathrm{OTF}(\nu_v, \nu_u)$ is called the modulation transfer function (MTF) of the system, and the phase of $\mathrm{OTF}(\nu_v, \nu_u)$ is called

its phase transfer function (PTF):

$$\mathrm{OTF}(\nu_v,\nu_u) = \mathrm{MTF}(\nu_v,\nu_u)\, e^{i2\pi \mathrm{PTF}(\nu_v,\nu_u)} .$$

For an unaberrated system, $P(v,u)$ is usually a real-valued, binary-type function; i.e., $P(v,u)$ is either zero or one. In that case, the value of the denominator in Eq. (12) is equal to the area of the pupil, and the value of the numerator is equal to the overlap area between the pupil and a shifted replica of itself. Therefore, the value of the transfer function at any spatial frequency coordinate (ν_v,ν_u) can be found by shifting the pupil by an amount $\lambda f \nu_v$ in v and $\lambda f \nu_u$ in u, calculating the area of overlap, and normalizing by the total area of the pupil.

The center of the unshifted nth aperture element (Fig. 14) is located at coordinates (v_{no},u_{no}). If the nth aperture is shifted in accordance with the autocorrelation integral, its new center coordinates become $(v_{no} + \lambda f \nu_v,\ u_{no} + \lambda f \nu_u)$. The distance between the center of the unshifted mth aperture element located at (v_{mo},u_{mo}) and the shifted mth aperture element is

$$l_{nm}(\nu_v,\nu_u) = [(v_{no} + \lambda f \nu_v - v_{mo})^2 + (u_{no} + \lambda f \nu_u - u_{no})^2]^{1/2}.$$

If l_{nm} is normalized by the diameter of an aperture element such that

$$\xi_{nm}(\nu_v,\nu_u) = \frac{l_{nm}(\nu_v,\nu_u)}{d} , \tag{13}$$

then the mth and nth apertures will overlap only if $l_{nm} < 1$. The amount of overlap is proportional to the contribution of the mth and nth pair to the $\mathrm{OTF}(\nu_v,\nu_u)$ at the spatial frequency ν_v,ν_u. For circular aperture

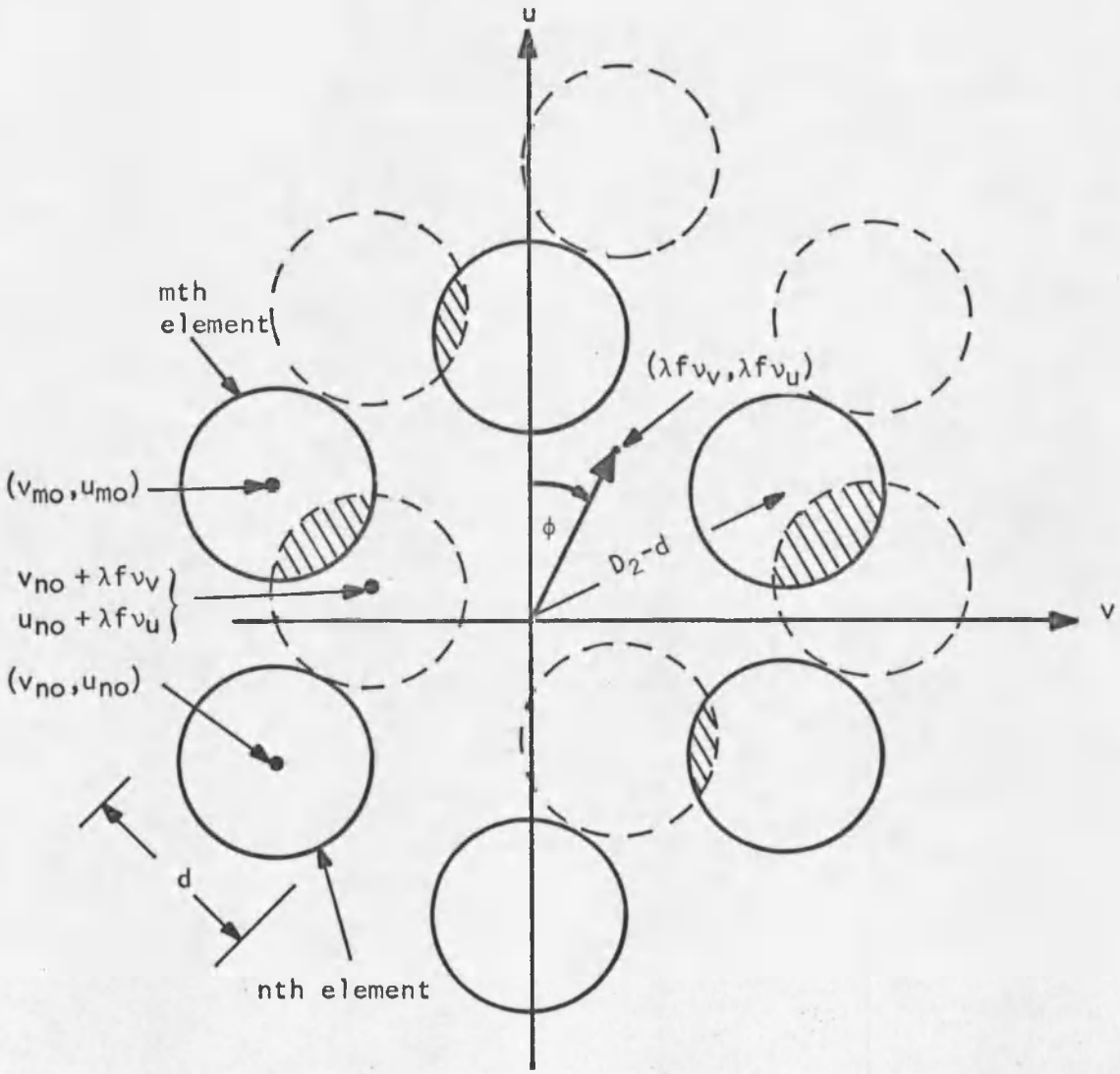

Fig. 14. Autocorrelating the Pupil Function.

elements this contribution is (Smith, 1966, p. 318)

$$\mathrm{MTF}_{nm}(\xi_{nm}) = \frac{2}{\pi}\left[\cos^{-1}\xi_{nm} - \xi_{nm}\sin(\cos^{-1}\xi_{nm})\right]. \tag{14}$$

The total transfer function is the sum of the contributions from all pairs of aperture elements

$$\mathrm{OTF}(\nu_v,\nu_u) = \frac{1}{N}\sum_{n=1}^{N}\sum_{m=1}^{N}\mathrm{MTF}_{nm}(\xi_{nm}). \tag{15}$$

This expression is valid for any array of circular aperture elements having a diameter d and focal length f. The value of ξ_{nm} goes to zero and hence MTF_{nm} is a maximum when

$$\nu_v = \frac{v_{mo} - v_{no}}{\lambda f}$$

$$\nu_u = \frac{u_{mo} - u_{no}}{\lambda f}.$$

Therefore, $\mathrm{OTF}(\nu_v,\nu_u)$ consists of a series of peaks having the form of Eq. (14), centered at locations in the spatial frequency plane that are determined by the relative separation and orientation of pairs of the aperture elements.

For an array of N aperture elements positioned on a circle, it is convenient to express $\xi_{nm}(\nu_v,\nu_u)$ in polar coordinates. Referring to Fig. 14, one can write

$$\nu_v = \nu'\cos\phi = \nu\nu_{\max}\cos\phi = \frac{D}{\lambda f}\nu\cos\phi$$

$$\nu_u = \nu'\sin\phi = \nu\nu_{\max}\sin\phi = \frac{D}{\lambda f}\nu\sin\phi$$

$$v_{no} = \tfrac{1}{2}(D - d)\sin\left[(N-1)\,\frac{2\pi}{N}\right]$$

$$u_{no} = \tfrac{1}{2}(D - d)\cos\left[(N-1)\,\frac{2\pi}{N}\right],$$

where d and D are the diameters of the individual pupil elements and the synthesized pupil, respectively. Substituting into Eq. (13) yields

$$\xi_{nm} = \frac{1}{d}\left\{\left(D\nu\sin\phi - \tfrac{1}{2}(D-d)\left[\sin(m-1)\,\frac{2\pi}{N} - \sin(n-1)\,\frac{2\pi}{N}\right]\right)^2 + \left(D\nu\cos\phi - \tfrac{1}{2}(D-d)\left[\cos(m-1)\,\frac{2\pi}{N} - \cos(n-1)\,\frac{2\pi}{N}\right]\right)^2\right\}^{\frac{1}{2}}. \tag{16}$$

Cross sections of the OTF were calculated using Eqs. (15) and (16) and are plotted in Fig. 15 for $\phi = 0°$, $45°$, and $90°$. The OTF corresponds to a six-element array in which the element diameter is one fourth the diameter of the synthesized aperture. The cross sections show the asymmetrical nature of the OTF. The curves are also marked to indicate which aperture element pairs contribute to a particular spatial frequency region. If an aperture element is aberrated, it can affect only those regions where it makes a contribution to the OTF. For example, aberrations in pupil element 1 will be reflected in all spatial frequency regions of the $\phi = 0°$ curve except from $0.25 < \nu < 0.5$. The OTF for $\phi = 45°$ is affected at all spatial frequencies by element 1, whereas the OTF for $\phi = 90°$ is affected only at spatial frequencies of less than 0.48. Of these three cross sections, the $\phi = 90°$ OTF is least sensitive to aberrations in aperture element 1. Therefore, as described in a later chapter, experimental measurement of the OTF was limited to the cases for which $\phi = 0°$ and $\phi = 45°$.

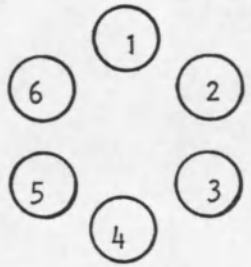

a Synthetic aperture array

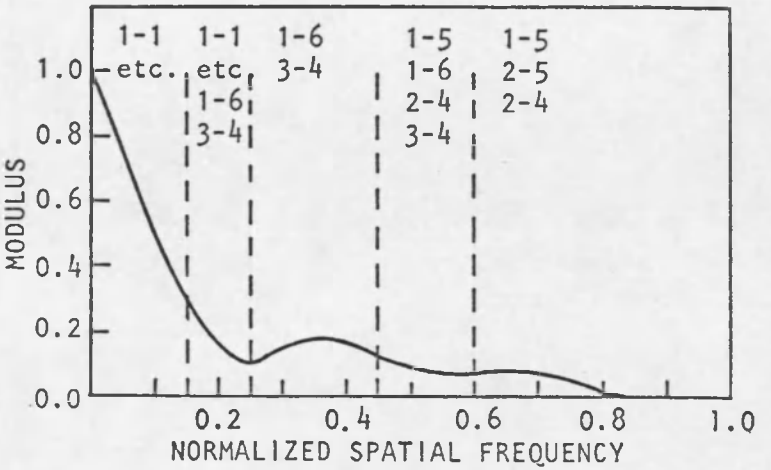

c ϕ = 45° OTF

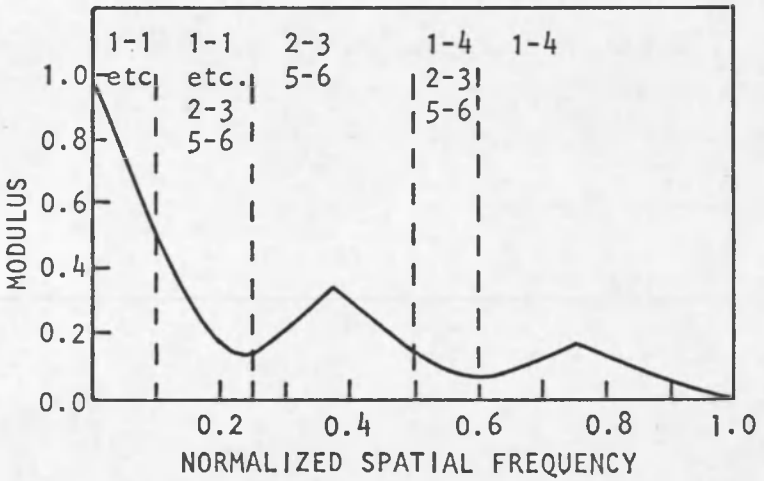

b ϕ = 0° OTF

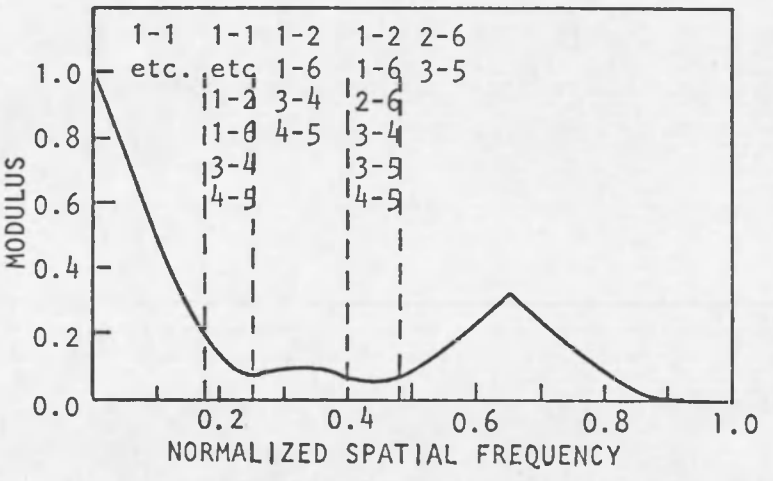

d ϕ = 90° OTF

Fig. 15. Unaberrated Transfer Function.

It is difficult to derive analytical expressions for the transfer function of an arbitrarily aberrated synthetic aperture system, but for several simple aberrations one can determine qualitatively what should happen to the transfer function. For example, when piston error is introduced into aperture element 1, the component fringe field produced by element 1 and any unaberrated element is shifted, with no decrease in its modulation. Therefore, in spatial frequency regions where only one pair of aperture elements contributes to the OTF, there can be no change in the OTF modulus due to piston error. This characteristic is illustrated by the $\phi = 0°$ OTF in Fig. 15, where the aberrated element (aperture 1) interacts with other elements in the region $0.5 < \nu < 1.0$. For $\nu > 0.6$, only one pair of elements contributes to the OTF; therefore the modulus is unchanged although the phase transfer function is nonzero. For those spatial frequency regions in which element 1 interacts only with itself ($0 < \nu < 0.25$), there will be no effect. However, in the $0.5 < \nu < 0.6$ region the shifted fringe field produced by elements 1 and 4 will be added to the unshifted fringe field produced by elements 2 and 3, and 5 and 6. The resultant is a sinusoidal fringe field having a reduced modulus as well as a phase shift.

As a second example, consider the effect of a $\lambda/2$ piston error on the OTF in the $\phi = 45°$ direction. In the region $0.25 < \nu < 0.85$, the area of overlap between the aberrated element and any unaberrated element just equals the area of overlap between pairs of unaberrated elements. As a result there will be two fringe fields for each spatial frequency superimposed in the point spread function, one having no phase shift and the other having a half-period phase shift. The resultant

fringe field will be of uniform intensity. That is, the modulus goes to zero for all spatial frequency components greater than 0.25. A similar situation exists in the region $0.25 < \nu_{xx} < 0.4$ for the $\phi = 90°$ OTF.

Very Large Aberrations

When large amounts of aberration are present in one element of the array, the spread function associated with that element is much larger than the spread function associated with the unaberrated elements. As a result, the aberrated element makes only a small contribution to the central region of the synthetic aperture spread function. For very large amounts of aberration the contribution is negligible and the array may be considered to be effectively a five-element array. The transfer function for this case is that of the unaberrated five-element array normalized to the volume under the aberrated six-element point spread function.

Figure 16 shows cross sections of the transfer function for this case, from which we conclude that the effect of large aberrations is most significant for the $\phi = 45°$ and $\phi = 0°$ cross sections. The curves represent the asymptotic values of the transfer function as the aberrations become large. For moderate amounts of aberration, however, the transfer function may be lower than that shown in Fig. 16, depending on the phase and amplitude of the amplitude spread function associated with the aberrated element.

a

ϕ = 0°

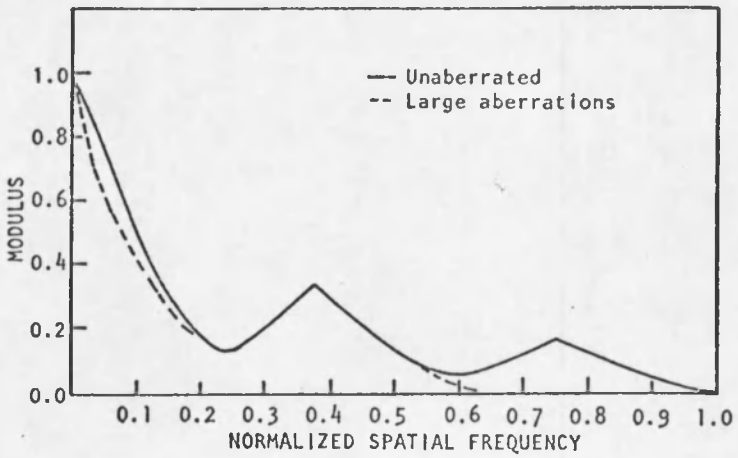

b

ϕ = 45°

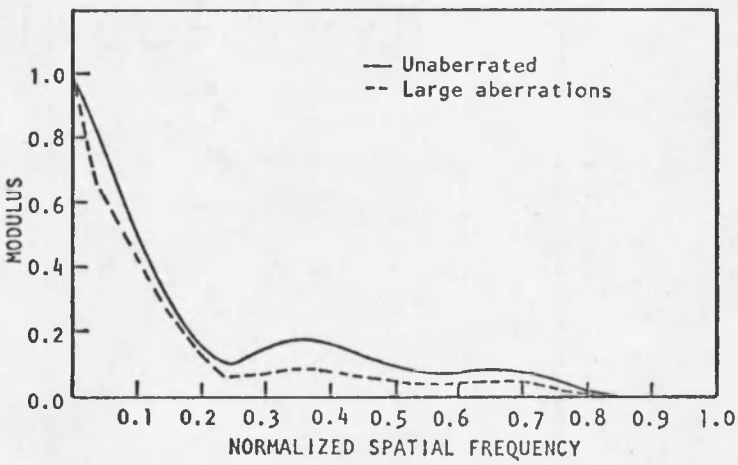

c

ϕ = 90°

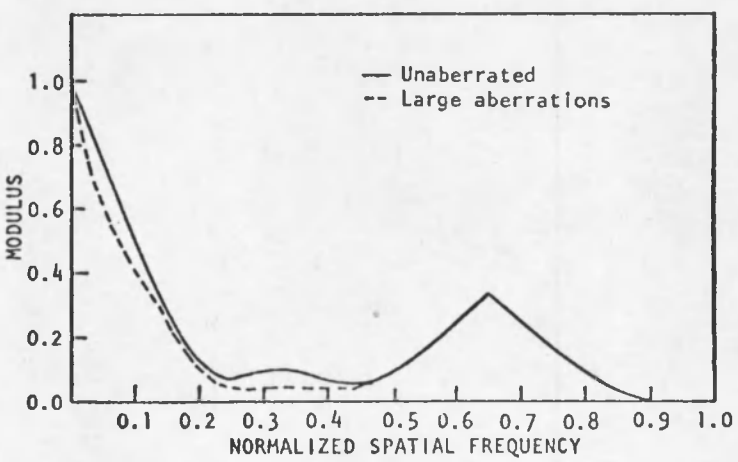

Fig. 16. Transfer Function for Very Large Aberrations in One Element.

CHAPTER III

COMPUTER SIMULATION

The computer simulation of an aberrated synthetic aperture system was done on the University of Arizona's CDC 6400 computer using the OTF program package developed at the Optical Sciences Center.

With this program the point spread function and optical transfer function were calculated from specified pupil functions. The pupil function was generated by first specifying the relative locations and radii of the circular pupil elements. Then phase aberrations were introduced across individual pupil elements by specifying A, m, n, and α for an aberration polynomial of the form

$$W(\rho,\phi) = \sum_{i=1}^{N} A_i \rho^{m_i} [\cos(\phi-\alpha_i)]^{n_i}. \tag{17}$$

Here ρ and ϕ are the coordinates of a point within an individual pupil element, referenced to the center of that element, and α indicates the orientation of the aberrated wave within the pupil element. In addition, phase variations were introduced across the entire array by specifying A, m, n, and α for a coordinate system whose origin is at the center of the array.

The program evaluates the pupil function at points in a 32 × 32 matrix, and then calculates the point spread function and optical transfer function using a Fast Fourier Transform routine. Both of these

functions emerge from the computer in 64 × 64 matrices. Output options include a printout, isometric plots, contour plots, and section plots.

The program package used for the computer simulation is described in detail elsewhere (Fell, Rancourt, and Shannon, 1971).

Error Due to Rectilinear Sampling

The small size of the input matrix and the rectilinear character of that matrix cause a small but noticeable error in the calculated transfer function. In this study the pupil element diameter was one fourth the synthesized pupil diameter. So, although the synthesized pupil was sampled at 32 points across its diameter, the individual elements were sampled at only eight points across their diameter. As a result, the circular pupil element is described by an irregular shape, as illustrated in Fig. 17. The shape of the effective pupil element is also dependent upon the location of the center of the 32 × 32 matrix. For example, Fig. 17a shows the sampled pattern of a pupil element at the top of the matrix, and Fig. 17b shows the pattern of an element at the origin of the matrix.

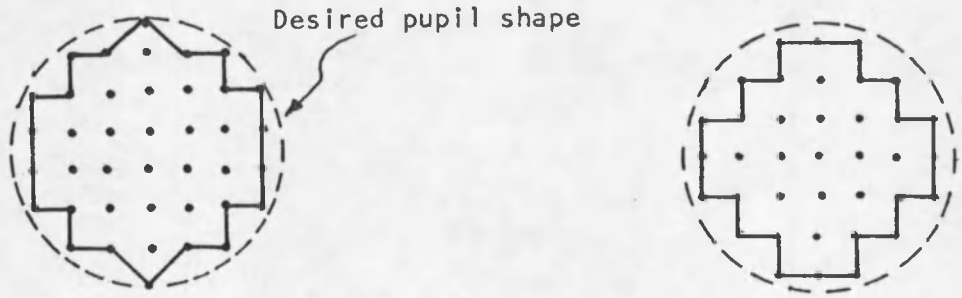

a. Pupil element at top of matrix

b. Pupil element at center of matrix

Fig. 17. Description of a Pupil Element by the 32 × 32 Matrix.

It is not surprising that these two different pupil shapes have different transfer functions. In Fig. 18 the transfer function cross sections for the two cases are compared with the exact transfer function for a circular pupil. The double values in Fig. 18a reflect the difference between two orthogonal sections of the slightly asymmetrical transfer function.

The computer-calculated transfer function cross sections of the six-element array used in this study are shown in Figs. 19 and 20. They are compared with the transfer function calculated from the analytical expression in Eq. (15). The error is effectively zero for the $\phi = 45°$ cross section and is very small for the $\phi = 0°$ cross section.

When aberrations are introduced into the multiple-element array, the errors do not necessarily remain insignificant. For example, if a piston error of λ/X is introduced into a pupil element, the $\phi = 0°$ phase transfer function should have a value of $1/X$ cycles for normalized spatial frequency components greater than 0.6 (see pupil interaction discussion in Chapter II). Calculated by the computer program, however, the phase transfer functions (Fig. 20) do not reach the proper values at $\nu = 0.6$ owing to the rectilinear pupil sampling. Although these errors are small in terms of the gross behavior of the curves, they are present and should be kept in mind when the curves are interpreted.

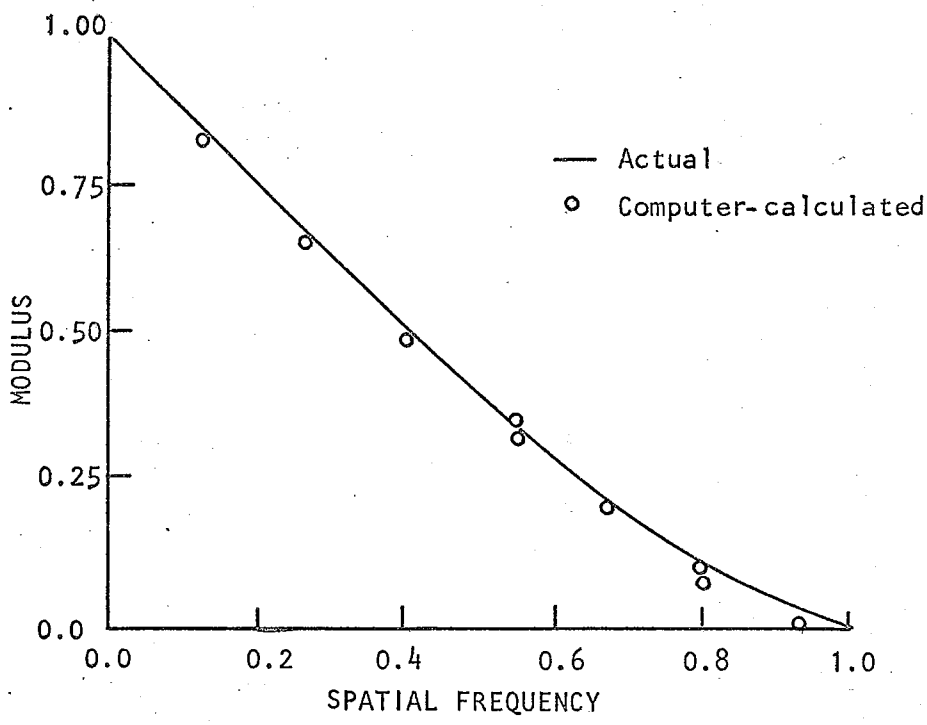

a Element at top of matrix

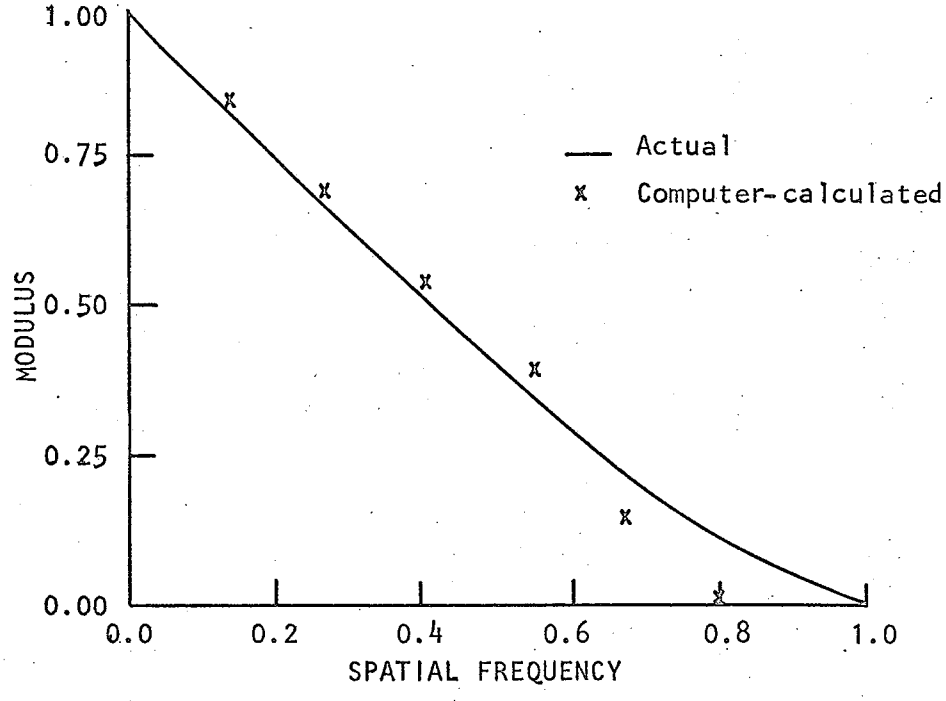

b Element at center of matrix

Fig. 18. Computer-Calculated Transfer Function of an Individual Pupil Element.

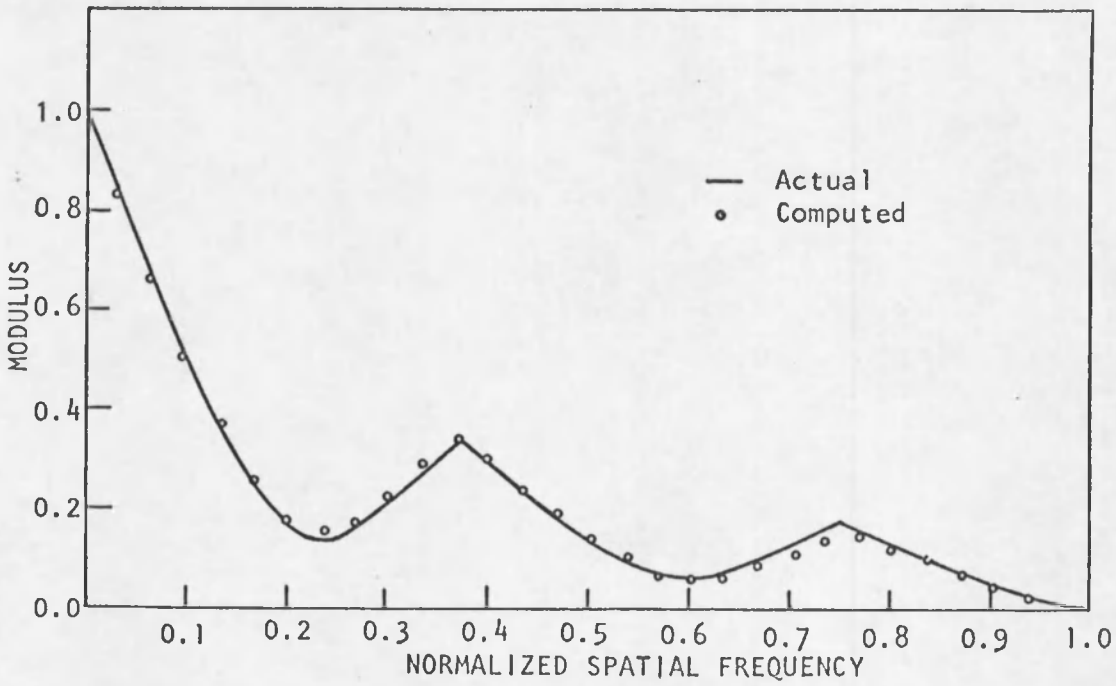

a $\phi = 0°$

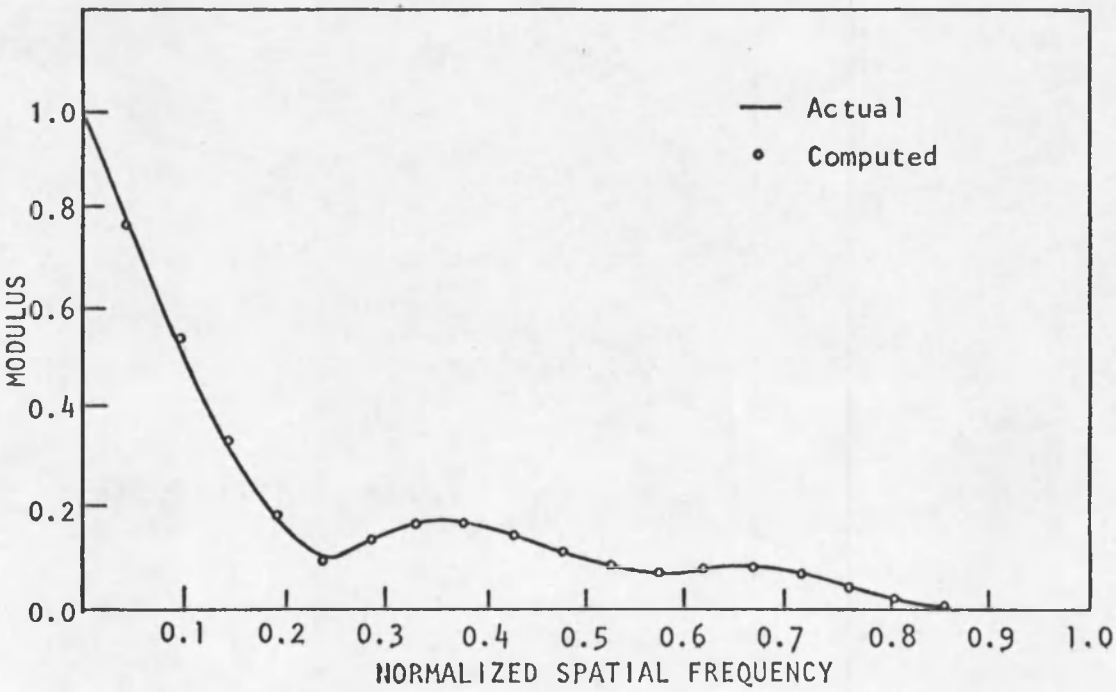

b $\phi = 45°$

Fig. 19. Computer-Calculated Unaberrated Transfer Function of the Synthetic Aperture.

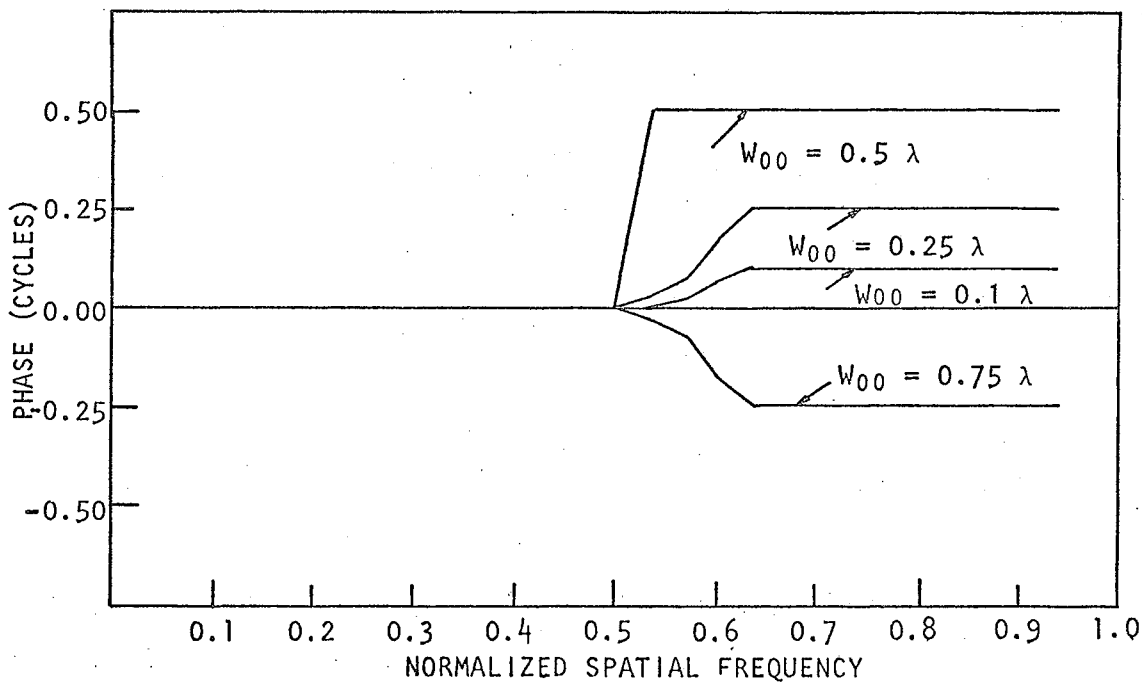

Fig. 20. Computer-Calculated $\phi = 0^{\circ}$ PTF for Piston Error.

Quarter-Wave Restriction

The OTF computer program is limited in that the phase variation between any adjacent sample points cannot exceed $\lambda/4$. This restriction limits the maximum value of the aberration coefficient that can be used. For pupils with a large density of sampled points, this restriction is not important until the magnitude of the aberrations is very large; however, even small to moderate amounts of aberration can violate the restriction for the synthetic aperture arrays used in this study.

Table 2 shows the maximum allowable aberration coefficients that could be used in this study as a result of the $\lambda/4$ restriction.

Table 2. Maximum Magnitude of Aberrations That Can Be Used with Computer Program.

Aberration	Max. value of aberration coefficient
Piston error	No restriction
Tilt	$W_{11} \leq 1.0\lambda$
Defocus	$W_{20} \leq 0.56\lambda$
Spherical aberration	
Paraxial focus	$W_{40} \leq 0.35\lambda$
Mid focus	$W_{40} \leq 1.25\lambda$
Marginal focus	$W_{40} \leq 0.79\lambda$
Coma	$W_{31} \leq 0.43\lambda$
Astigmatism	
Sagittal or tangential focus	$W_{22} \leq 0.56\lambda$
Mid focus	$W_{22} \leq 1.13\lambda$

CHAPTER IV

THE EXPERIMENTAL PROGRAM

The purposes of the experimental portion of this program were (1) to measure the transfer function when the aberrations are large and the OTF program cannot be used and (2) to observe the images of point sources and extended objects formed by aberrated synthetic aperture systems.

A block diagram of the experimental arrangement is given in Fig. 21. It shows the three major functional subsystems: the illumination stage, the synthetic aperture system, and the detection stage. The illumination stage provides two test objects, a point source and an extended object, located at infinity. The synthetic aperture system, which

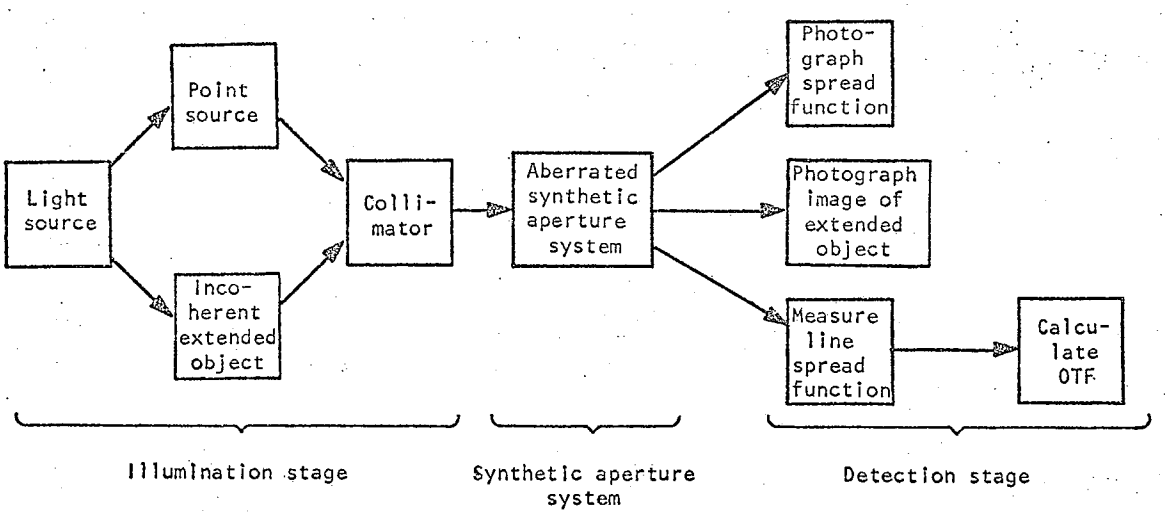

Fig. 21. Block Diagram of the Experimental Setup.

can be aberrated in varying forms and magnitudes, forms images of the test objects in the vicinity of the detection stage. The detection stage photographs the point spread function, photographs the image of the extended object, and measures the line spread function of the aberrated synthetic aperture system. A cross section of the optical transfer function is then calculated from the line spread function. Figure 22 is a photograph of the experimental arrangement on a 5-m optical bench.

Aberrated Synthetic Aperture System

The heart of the experimental setup was the aberrated synthetic aperture system. An unaberrated synthetic aperture system was simulated by placing a mask that defines the aperture array near the pupil of a high-quality telescope objective (Fig. 23). The array used in the experimental investigation consisted of six circular pupil elements equally spaced on a circle. The ratio of the synthesized pupil diameter to the individual element diameter was 4:1. Aberrations were introduced into one aperture element with an aberration generator.

The Unaberrated Array

The high-quality telescope objective was an $f/8.7$ doublet with a 4.5-in. diameter, manufactured by Diffraction-Limited, Inc. An identical lens was used as the collimator in the illumination stage. Because these two lenses limited the image quality of the unaberrated synthetic aperture system, they were tested separately and in tandem with a scatterplate interferometer. The resulting interferograms revealed that the collimating lens suffered from approximately 0.2λ of astigmatism and the

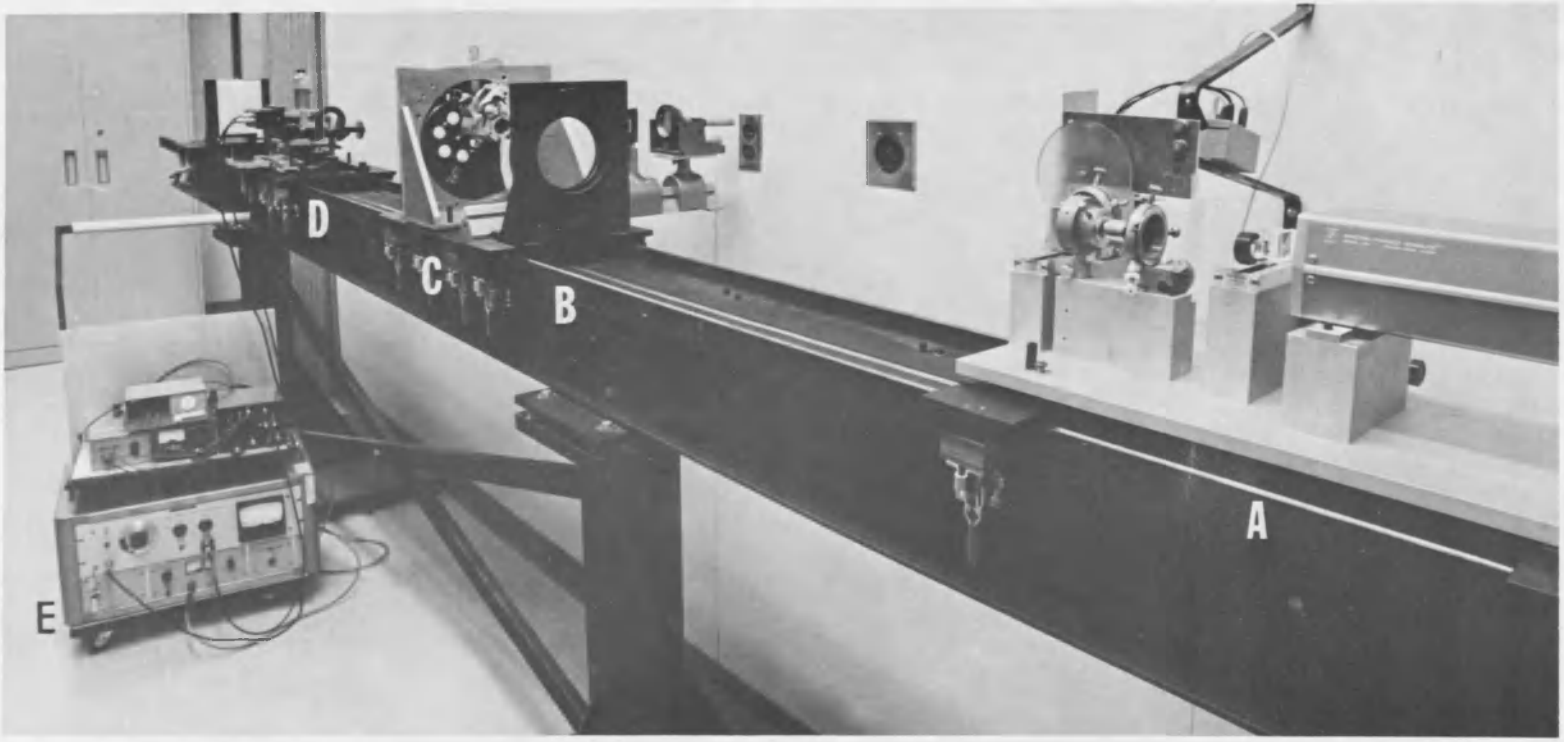

Fig. 22. Photograph of the Experimental Setup.

(A) Illumination stage, (B) collimating lens, (C) aberrated synthetic aperture system, (D) detection stage, (E) electronics.

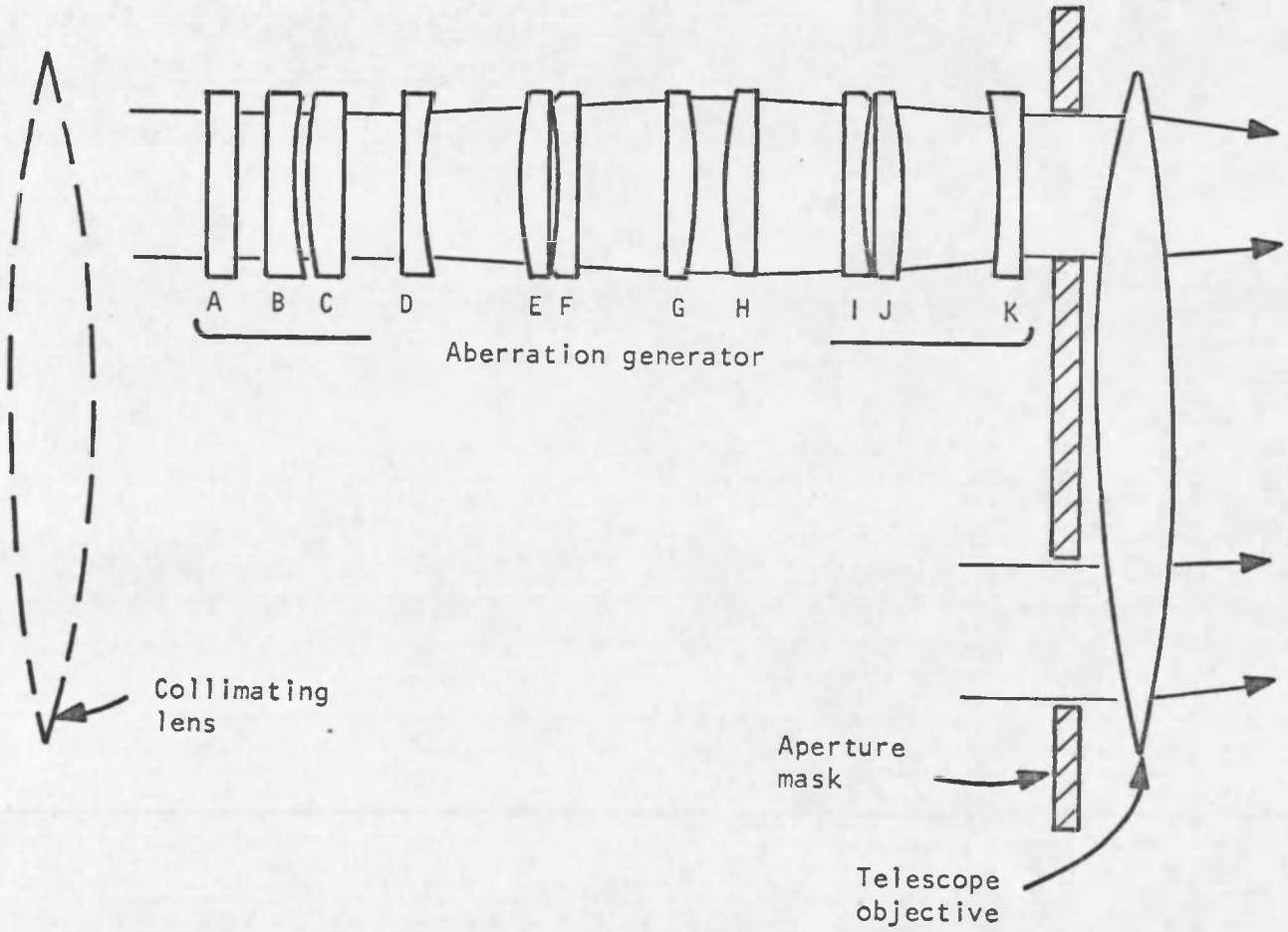

Fig. 23. Schematic of Synthetic Aperture System.

telescope objective had about 0.16λ of spherical aberration. In addition, each lens produced a 0.25λ deformation in the center of the wavefront. Fortunately, the deformations were in different directions, and when the lenses were used together the net wavefront deformation was nearly zero.

The effect of the spherical aberration was reduced by first stopping down the aperture of the objective to a diameter of 4 in. (f/10). Then the objective was focused for the zone in which the aperture elements were positioned. As a result, the wavefront error across a pupil element due to the spherical aberration was reduced to less than 0.05λ. The astigmatism was removed by introducing a compensating amount of astigmatism with a plane-parallel plate. The plate was positioned in the converging beam formed by the telescope objective and was tipped 11° with respect to the optical axis. At this angle, astigmatism was the only significant aberration introduced by the plate.

Figures 24a and 24b show the point spread function for the f/10 circular pupil and the f/10 synthetic aperture array before the plate was inserted into the beam. Introducing the plate reduced the astigmatism to nearly zero as shown in Figs. 24c and 24d. The corrected images exhibited a slight but insignificant amount of aberration.

Aberration Generator

The function of the aberration generator was to introduce controlled amounts of aberrations, either independently or in combination, into one element of the synthetic aperture array. The aberrations introduced were piston error, tilt, defocus, spherical aberration, coma,

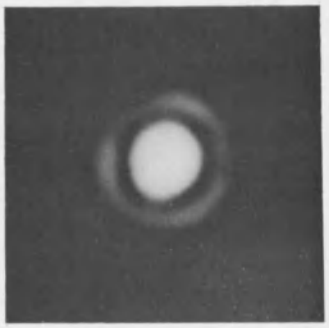

a. *f*/10 circular pupil, without plate

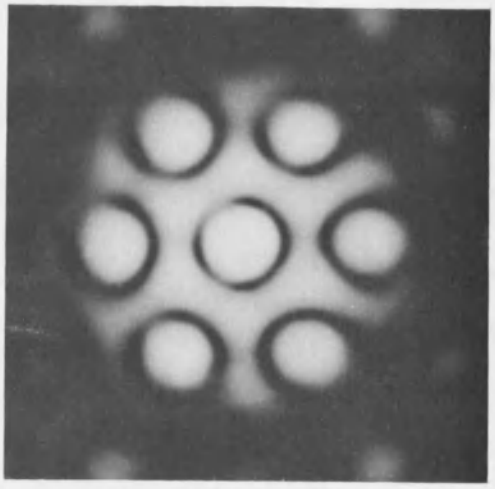

b. *f*/10 array, without plate

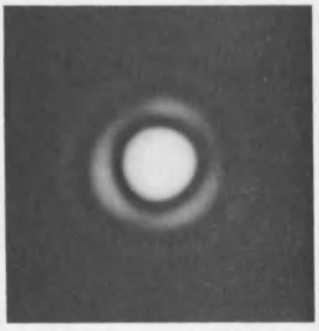

c. *f*/10 circular pupil, with plate

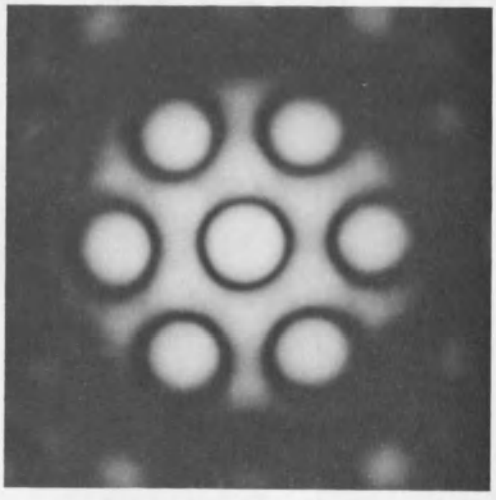

d. *f*/10 array, with plate

Fig. 24. Point Spread Function with and without the Astigmatism-Compensating Plate.

and astigmatism. The magnitude of each aberration could be varied from 0.05λ to 2.0λ, and the orientation of the aberration could be varied in the case of coma, astigmatism, and tilt. The generator was color corrected over the visible spectrum although it was used only at λ = 632 nm in this study. The isoplanatic angular field of the aberration generator was designed to be ±0.5°. Because the aberration generator operates in collimated light (see Fig. 23), it had to be afocal and have an angular magnification of unity.

A significant feature of the aberration generator was that the aberrations it introduced were not field dependent. The magnitude of coma, astigmatism, and tilt were constant across the ±0.5 field. As a result, the extended object photographs show the images that would be formed at one point in the field for the general case of field dependent aberrations.

Design. Figure 23 shows the optical layout of the aberration generator. All optical element motions are referred to a coordinate system whose origin coincides with the center of the element. The first element (A) is a plane-parallel plate that rotates about the y axis and introduces a constant phase shift (piston error) across the aperture. Elements B and C are weak cylindrical lenses that introduce astigmatism when their cylindrical axes are not parallel. By counterrotating B and C about the z axis the amount of astigmatism can be varied, and by rotating both in the same direction the orientation of the astigmatism can be varied.

The next four elements (D-F) form an afocal system whose angular magnification is about 0.9. Element D can be translated along the z

axis to introduce defocus. Element D and doublet E introduce negative spherical aberration, which just cancels the positive spherical aberration introduced by element F. When doublet E is moved along the z axis, its spherical aberration contribution changes (it is in a diverging beam), and therefore the net spherical aberration is no longer zero. Either negative or positive spherical aberration may be introduced. Because doublet E has zero power, the telescope remains afocal when E is shifted.

Elements G, H, and I form a telescope identical to the one just described except that the sequence of its elements is reversed. As a result, the net angular magnification of the two telescopes in tandem is unity. Element G, just like element F, is stationary. Doublet H moves in the x-y plane to produce coma. Wavefront tilt is introduced by rotating element I about the center of curvature of its concave surface. This rotation effectively adds a prismatic element to element I and causes the wavefront to deviate. The direction and magnitude of coma or tilt are determined by the direction and magnitude of the corresponding lens motion.

The aberration generator is shown in Fig. 25 in its operating position. Aberrations are introduced with knobs A-F. To prevent vignetting when imaging off-axis points, the aberration generator is positioned very close to the aperture mask. The clear aperture of the aberration generator is 28 mm, or about 3 mm larger than the diameter of an aperture element.

The detailed optical design of the aberration generator is given in Appendix A.

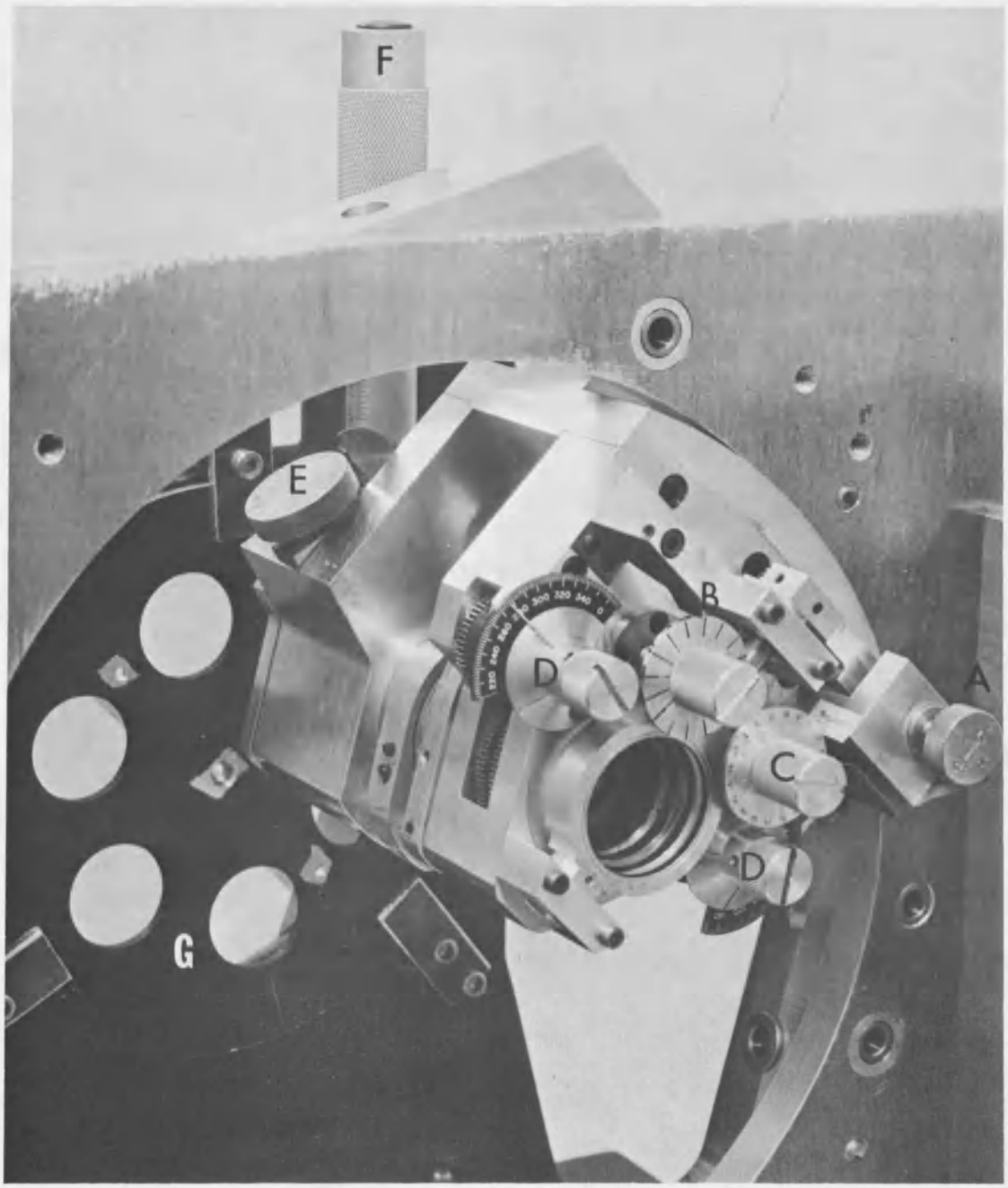

Fig. 25. Photograph of the Synthetic Aperture System.

(A) Piston error control, (B) focus control, (C) spherical aberration control, (D) astigmatism controls, (E) coma control, (F) tilt control, (G) aperture.

Calibration. The aberration generator was calibrated with a Twyman-Green interferometer that was incorporated as an integral part of the simulated synthetic aperture system. Thus the calibration could be made with the aberration generator in its operating position, and any misalignments could be detected. Figure 26 shows the components of the interferometer in position for calibrating the aberration generator. A beamsplitter was positioned between the collimating lens and the aberration generator. Light transmitted through the beamsplitter traversed the aberration generator and was reflected back toward the beamsplitter by the signal arm mirror (the telescope objective was moved to make room for this mirror). Light reflected by the beamsplitter traveled to the reference arm mirror and was reflected back to the beamsplitter, where it recombined with the signal arm beam. The resulting interference fringes were viewed on a ground glass screen (as in Fig. 26) or photographed.

All aberrations introduced by the aberration generator, except for piston error and tilt, were measured with the Twyman-Green interferometer. The dial settings for the aberration control knobs were correlated with the wavefront errors measured with the interferograms.

Piston error and tilt could not be measured conveniently with the interferometer. Instead, the effect of these aberrations on the point spread function was used as a calibration tool.

For piston error the following procedure was used:

(1) The piston error was adjusted to zero by making the point spread function of the six-element array symmetrical.

(2) All aperture elements were covered except the aberrated element and one of the unaberrated elements. The position

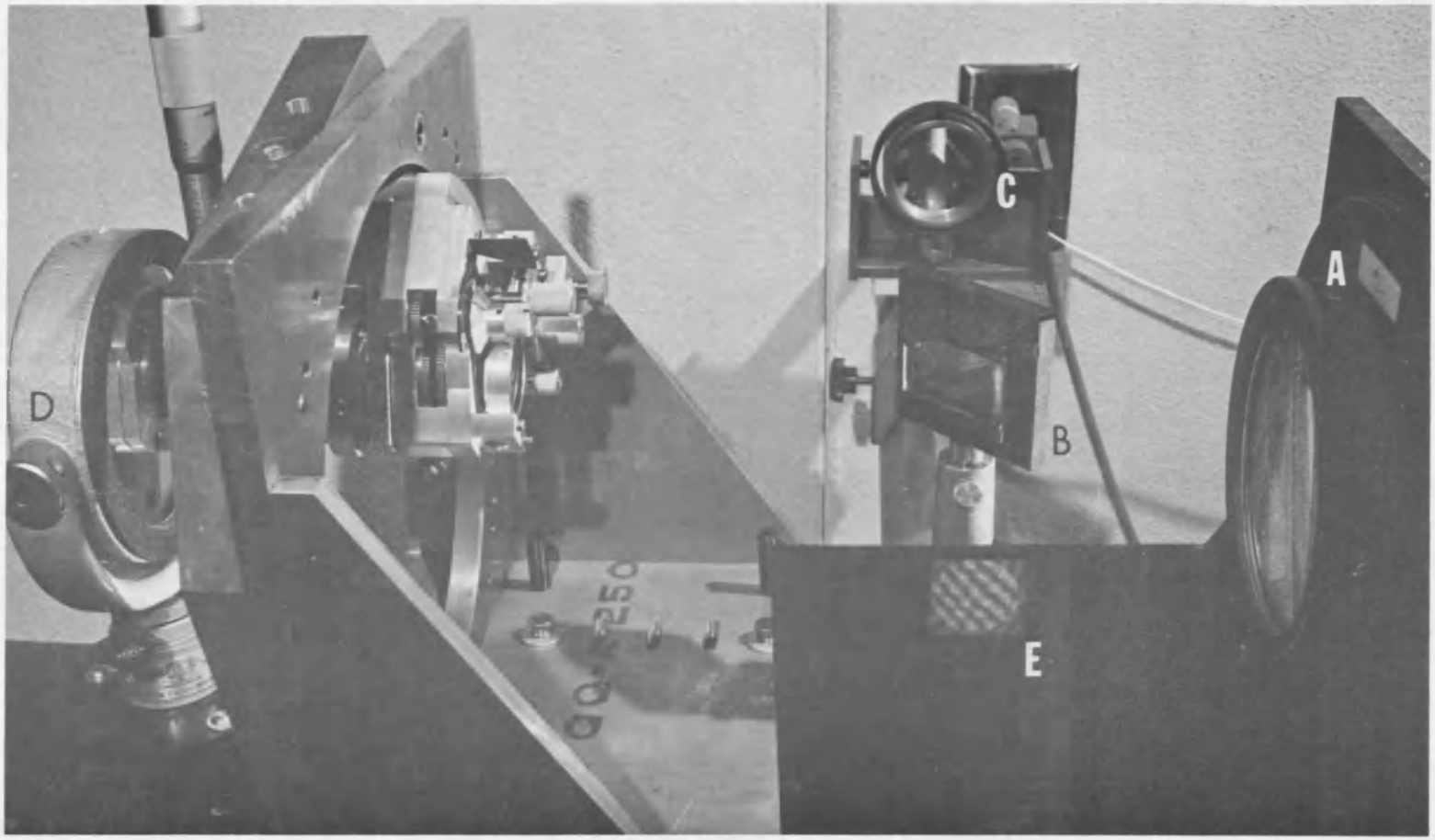

Fig. 26. Configuration for Calibration of the Aberration Generator.

(A) Collimating lens, (B) beamsplitter, (C) reference arm mirror, (D) signal arm mirror, (E) interference pattern.

as well as the period of the sinusoidal fringes in the point spread function were noted.

(3) X waves of piston error were introduced by moving the sinusoidal fringes X periods.

Using this method, piston error was introduced with an accuracy of about 0.05λ.

When tilt is introduced, the point spread function of the aberrated element shifts an amount δ, where

$$\delta = W_{11} f\lambda/a.$$

In this expression, f is the system focal length, a is the aperture element radius, and W_{11} is the tilt aberration coefficient expressed in waves. The diameter, d, of the first dark ring in the Airy pattern is given by

$$d = 1.22\lambda f/a,$$

and therefore

$$\delta = dW_{11}/1.22.$$

The last relationship and the measured value of d were used to introduce the desired amount of tilt. The point spread function of the aberrated element was shifted by an amount δ from the position of the unaberrated point spread function. This method permits tilt to be introduced with an accuracy of about 0.05λ.

Performance Evaluation. The aberration generator was designed to be free of aberrations over a $\pm 0.5^{\circ}$ field with the aberration controls in their null positions. In spite of the large number of optical

elements (11) within the device, it forms an image that exhibits only small residual aberrations.

The wavefront imperfections are apparent in the interferograms in Fig. 27, which show that about 0.14λ of astigmatism is present. (A slight difference in the powers of the astigmatism-generating cylinders prevents the complete zeroing of astigmatism.) The worst wavefront deformation at any point in the pupil is 0.2λ. The corresponding point spread function, shown in Fig. 28, is nearly free of aberrations.

Figures 27 and 28 show an interferogram of the wavefront and the point spread function, respectively, for the axial object point used in the transfer function measurements and the point spread function photographs. When extended objects are being used, however, the off-axis performance of the aberration generator is of interest as well. To examine off-axis imaging, a point object was moved to various positions in the ±0.05° field, and observations were made of the point spread function of the six-aperture array. Since there was no significant change in the point spread function across the field, the extended object occupied an isoplanatic region in the field.

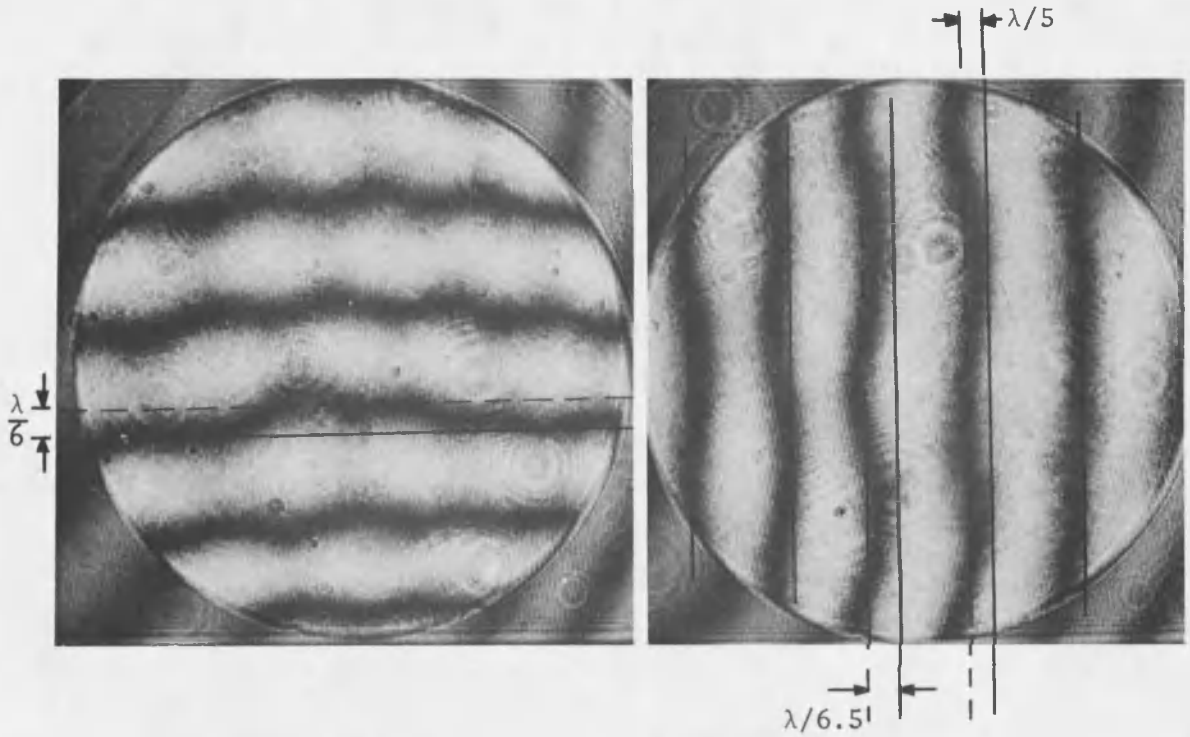

Fig. 27. Interferograms of the Wavefront Produced by the Aberration Generator (No Aberrations).

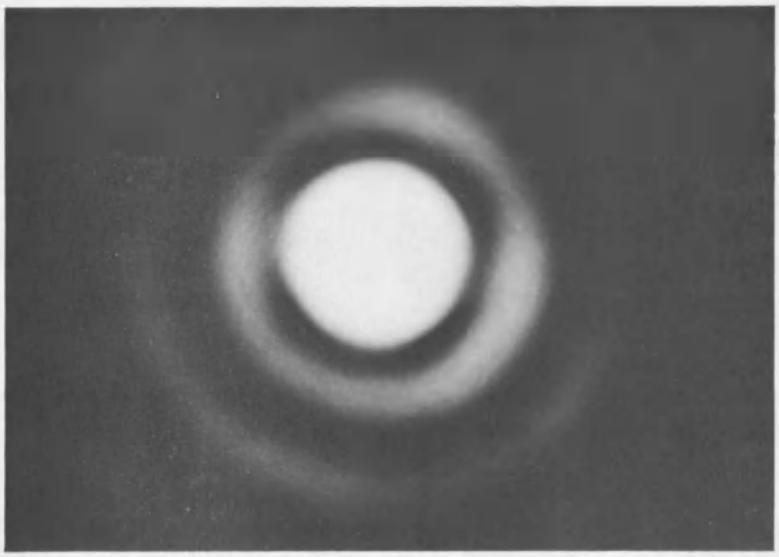

Fig. 28. PSF Associated with the Aberration Generator (No Aberrations).

The Illumination Stage

The illumination stage (Figs. 29 and 30) provides a point source and an extended object as test objects for the synthetic aperture system.

The light source is a Spectra-Physics Model 120 laser whose output is 5 mW at λ = 632 nm. When the point object is used (Fig. 29), the laser beam is focused by a 40X microscope objective onto a 5-μm-diameter pinhole. Light passing through the pinhole overfills the collimating lens by more than 50%. Since the Airy disk diameter for the $f/10$ collimating lens is about 15 μm, the 5-μm pinhole is a reasonably good approximation to a point source.

When the extended object is used (Fig. 30), a mirror and three prisms fold the light in a path around the microscope objective and pinhole. A diverging lens enlarges the laser beam from 2 mm to approximately 15 mm on the diffuser (Polacoat LS75 Lenscreen), which is rotated at 400 rpm to reduce the time-averaged spatial coherence of the light. The extended target, positioned close to the diffuser, is therefore incoherently illuminated over the time intervals of interest. Light transmitted by the target is reflected by a mirror toward the collimating lens.

Figure 31 is a photograph of the illumination stage (excluding the collimating lens). Prism 1 and the folding mirror are positioned on dovetailed slides so that they may be accurately moved into or out of the laser beam. The $\lambda/2$ plate is needed to rotate the orientation of the linearly polarized laser beam in order to reduce the visibility of fringes formed by front-to-back reflections from the beamsplitter in the Twyman-Green interferometer. (These fringes can be seen overlapping the fringe field of interest in Fig. 26.)

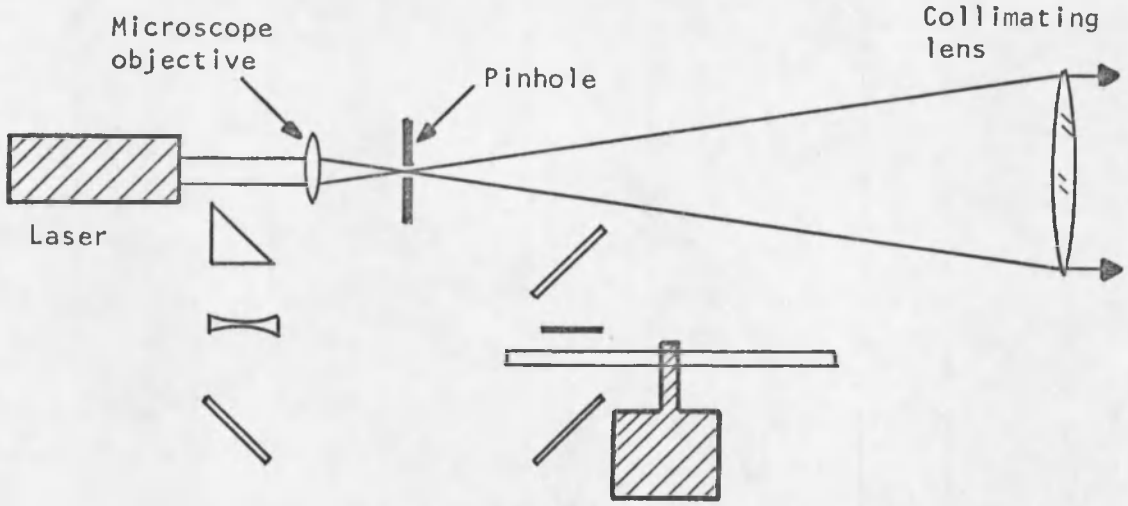

Fig. 29. Illumination Stage, Point Object.

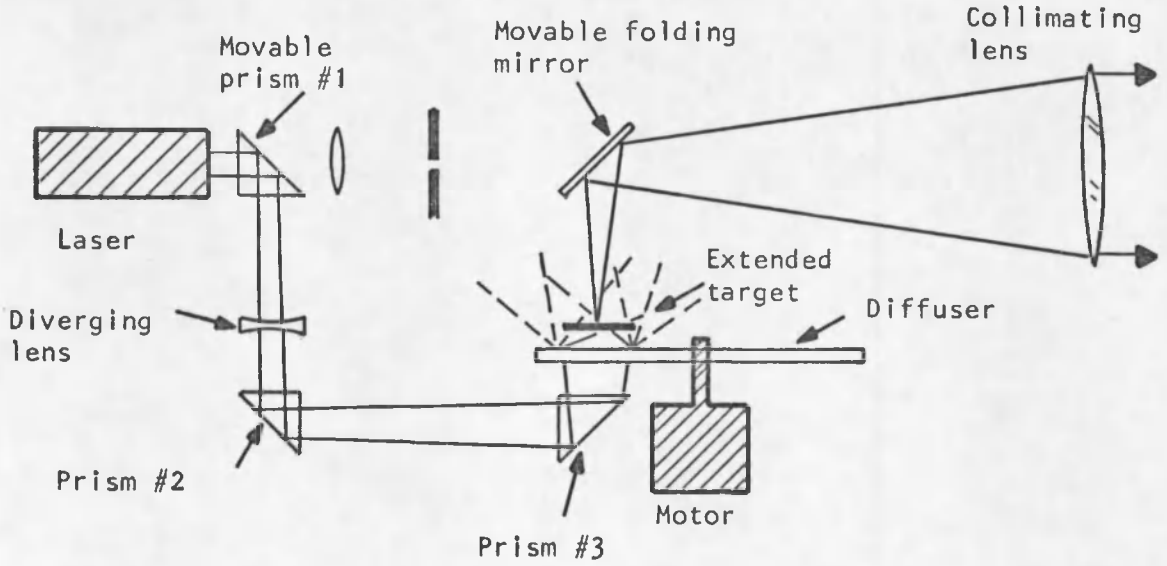

Fig. 30. Illumination Stage, Extended Object.

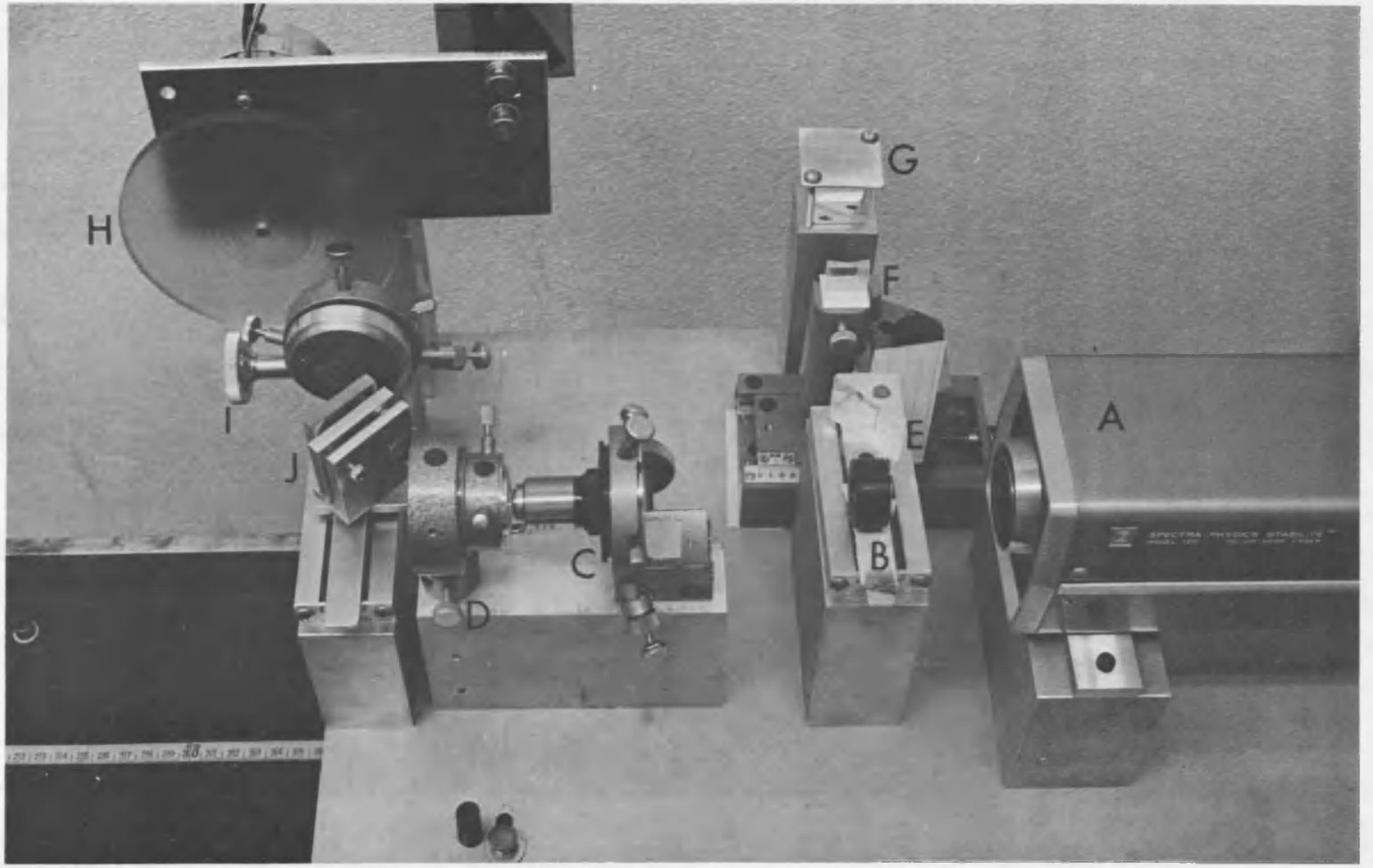

Fig. 31. Photograph of the Illumination Stage.

(A) Laser, (B) $\lambda/4$ plate, (C) microscope objective, (D) pinhole, (E) prism 1, (F) diverging lens, (G) prism 2, (H) spinning diffuser, (I) extended target, (J) folding mirror.

Uniformity of Illumination

In Chapter II it was assumed that the wave-field amplitude across the pupil was uniform. In practice this is seldom the case. Hopkins (1949, p. 22) investigated the effect on the point spread function when the amplitude distribution across a circular pupil decreases as the square of the distance from the center of the pupil. He found that the effect is negligible even for amplitude variations of 50%.

The intensity across the collimating lens was measured and found to decrease in a nearly quadratic manner to 65% of its peak value at the edge of the aperture. The corresponding amplitude distribution is shown in Fig. 32 along with the distribution used by Hopkins. It is evident that the field amplitude at the collimating lens is effectively uniform for imaging situations involving a circular pupil.

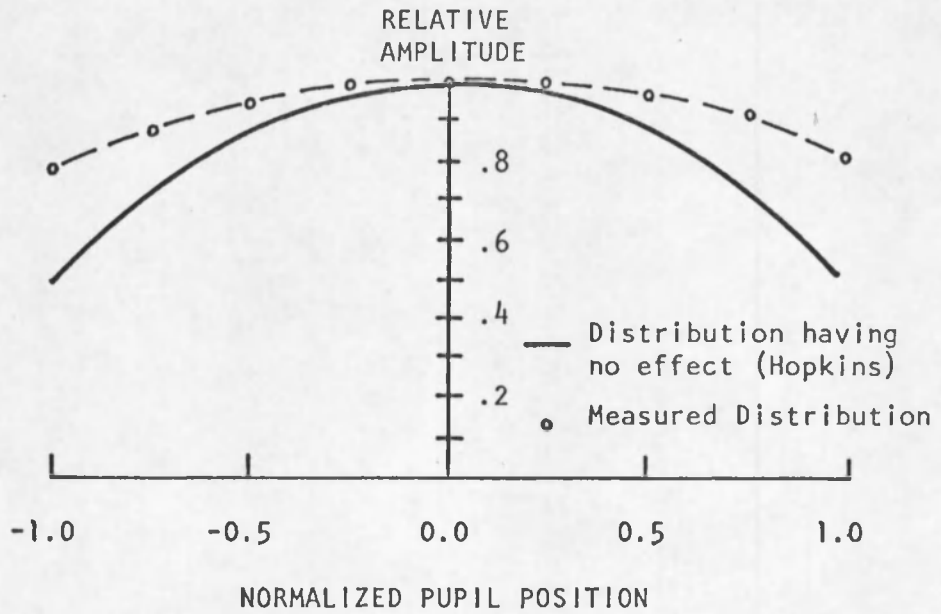

Fig. 32. Amplitude Variations across Diameter of Collimating Lens.

Unfortunately, the pupil used in the synthetic aperture experiments was not circular. In addition, the intensity distribution was not always centered on the pupil. Small mechanical drifts (and perhaps laser beam steering) often caused the distribution to be offset from the center of the lens. Reflections and absorption within the aberration generator also caused an intensity loss in the aberrated pupil element.

By careful adjustment of the pinhole at the illumination stage, it was possible to equalize the average amplitude of each aperture element to within ±6%. In many instances the difference in average amplitude was less than ±3%. The amplitude variation across an individual element was typically ±7% of the average amplitude. In view of the small magnitude of the variations and Hopkins' findings for a somewhat similar situation, it was assumed that the slight nonuniformity of illumination would not significantly affect the measurements. This assumption was supported by the high accuracy of the unaberrated transfer function measurements (to be presented later in this chapter).

Temporal Coherence of the Laser

For the simulated synthetic aperture system to work properly, light from the aberrated element must be able to interfere with light from the other elements. Since the aberration generator increases the optical path in the aberrated element by about 20 mm, the coherence length of the light must be much greater than 20 mm if a high visibility interference pattern is to be formed.

The Fourier transform of the laser's spectral energy distribution describes the temporal coherence properties of the laser, which in

turn determines the visibility of the interference fringes formed with the laser light (Born and Wolf, 1965, pp. 316-323). The spectrum, $S(s)$, of a laser that is oscillating in several axial modes simultaneously may be expressed as

$$S(s) = e^{-\pi(s/b)^2} \cdot \mathrm{comb}(s/\Delta),$$

where $\mathrm{comb}(s/\Delta)$ is an infinite series of impulses separated by an interval Δ, and b describes the width of the Gaussian-shaped, Doppler-broadened atomic resonance that modulates the series of very narrow laser lines (assumed to be δ functions) separated by a frequency Δ. The value of b for a He-Ne laser is 1500 MHz, and the value of Δ for the 45-cm-long laser used in this study is 300 MHz.

The Fourier transform of $S(s)$ is the visibility function

$$V(x) = \mathscr{F}\{S(s)\} = C\, e^{-\pi(bx)^2} * \mathrm{comb}(\Delta x),$$

where C is an unimportant constant. The visibility function is a series of Gaussian functions 6.6×10^{-10} sec wide, separated by 30×10^{-10} sec. The overlap of the Gaussian functions is negligible.

The 20-mm optical path difference introduced by the aberration generator corresponds to a time difference of 0.66×10^{-10} sec. Evaluating $V(x)$ at $x = 0.66 \times 10^{-10}$ sec yields $V(x) = 0.95$. That is, when the aberration generator is inserted in front of a pupil element, the fringes formed by that element and any other element drop in contrast by only 5%. Therefore, neglecting other factors, the transfer function will be 5% lower than theory predicts in spatial frequency regions where the aberrated element and one other element contribute to the transfer

function (e.g., $0.64 < \nu < 1.0$ in Fig. 15a). This error will be diluted in those spatial frequency regions where other element pairs contribute as well.

Spatial Coherence and the Extended Object

In order to use a laser in an incoherent imaging situation, the spatial coherence of the laser beam must be destroyed. In this experiment the spatial coherence was reduced by projecting an expanded laser beam onto a spinning diffuser. The expanded beam was approximately 15 mm in diameter, and the diffuser was positioned 40 mm behind the object, which was 2 mm in diameter. Therefore, the object effectively was illuminated by a broad source. By spinning the diffuser at 400 rpm, the phase relationships across the broad source were mixed for sufficiently long observation times. Typical exposure times were on the order of 1 sec, in which time the diffuser made six revolutions.

Photographs of resolution targets taken with the spinning diffuser did not show any of the characteristics of coherent images such as edge ringing. In addition, the highest spatial frequency component of the target to be resolved was the incoherent resolution limit. Therefore, it was concluded that the illumination scheme for the extended object did indeed produce an incoherent imaging situation.

The Extended Object

The extended object (hereafter referred to as the "target") used in this study was a photograph of a simulated aerial scene (Fig. 33), supplied by the U.S. Air Force. The target contains four resolution patterns, a runway with aircraft of various sizes, and an urban scene. Two

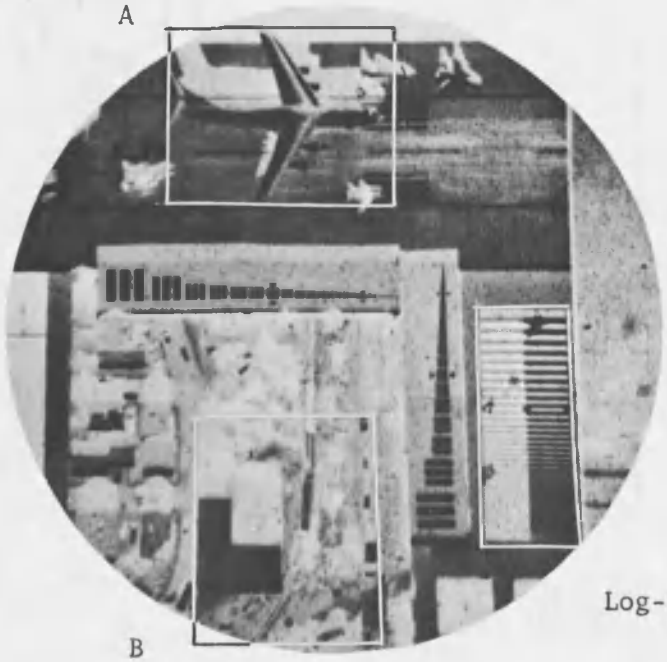

a. Entire Target (45X).

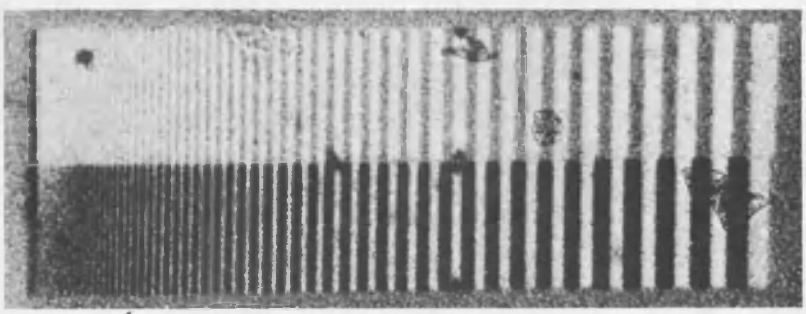

b. Section Showing Log-Periodic Target (150X).

Fig. 33. The Extended Target.

of the resolution patterns are Tri-Bar patterns with black bars on a gray background, which are oriented at 90° with respect to each other. The other two resolution patterns are log-periodic targets (a series of parallel bars whose spacing and width varies in a logarithmic manner), one having white bars on a black background and the other having white bars on a gray background. Resolution values for the log-periodic targets are given in Table 3.

Table 3. Spatial Frequency Values for Log-Periodic Target.

Element No.	Cycles/mm	Normalized to 160 cycles/mm	Element No.	Cycles/mm	Normalized to 160 cycles/mm
1	29.2	.182	19	70.3	.440
2	29.9	.186	20	74.1	.463
3	32.1	.194	21	77.2	.482
4	33.5	.209	22	81.7	.510
5	35.1	.219	23	85.9	.536
6	36.9	.230	24	90.0	.561
7	39.0	.244	25	96.0	.600
8	41.0	.256	26	101	.630
9	42.9	.268	27	106	.662
10	44.8	.280	28	112	.700
11	47.4	.296	29	118	.736
12	49.8	.312	30	122	.762
13	52.0	.325	31	131	.820
14	54.9	.342	32	139	.870
15	57.8	.362	33	140	.875
16	61.2	.382	34	146	.910
17	63.9	.398	35	158	.99
18	66.9	.417			

Although the entire image of the target was recorded on film and used to evaluate the effects of aberrations, only selected portions of the target are included in the discussion of experimental results (Chapter V). These portions were chosen on the basis of their sensitivity to

change with the introduction of aberrations. Although subtle changes occurred in most areas of the target, the changes in the selected portions were the most dramatic and illustrative of synthetic aperture imagery. The three target sections are marked in Fig. 33a. Section A contains a large aircraft and several smaller aircraft. Section B contains a large building, a railroad track, a four-car train, and four cars and trucks on a road. The third section contains the two log-periodic test patterns.

Since the transfer function for the synthetic aperture system being considered is asymmetric, two target orientations were used. In the $\phi = 0°$ (or 45°) orientation the target was oriented so that the log-periodic target reflected the $\phi = 0°$ (or 45°) transfer function.

The target transparency simulates a medium contrast aerial scene. Table 4 gives the contrast and corresponding modulation value of the scene from which the target transparency was made. These values, however, are not necessarily those of the target itself, as they do not include the effects of the camera and film that made the target transparency. In fact, the contrast of the log-periodic target is seen to decrease in Fig. 33 at high spatial frequencies.

Table 4. Contrast of Model from Which Target Photograph Was Made.

Pattern	Contrast	Modulation
Urban scene	3.0:1	.50
Tri-bar scene	4.68:1	.68
Log-periodic pattern		
White background	100:1 (high)	.98
Gray background	6.3:1 (medium)	.73

The enlargement of the target (Fig. 33b) shows that spatial frequency components of 196 mm^{-1} are present in the high-contrast log-periodic target. Since the $f/10$ synthetic aperture system cannot pass spatial frequencies greater than 160 mm^{-1}, the spatial frequency content of the image is limited by the synthetic aperture system rather than by the target.

Figure 33 shows many tiny bubblelike structures on the target transparency. These are part of the pellicle backing on the film and are needed to prevent the film from sticking together when it is rolled on a spool.

The Detection Stage

The functions of the detection stage are (1) to measure the line spread function of the aberration synthetic aperture system, (2) to photograph the point spread function, and (3) to photograph the image of the extended target.

The three configurations of the detection stage are shown in Fig. 34. For the line spread function measurement, a slit is positioned at the focus of the synthetic aperture system. The light passing through the slit is collected by a 10X microscope objective and directed to a photomultiplier tube by a folding mirror. These elements are mounted on a scanning stage so that the entire point spread function can be sampled by the slit.

When the point spread function is to be photographed, the slit and folding mirror are removed and the objective and eyepiece focus a highly magnified image of the point spread function directly onto the

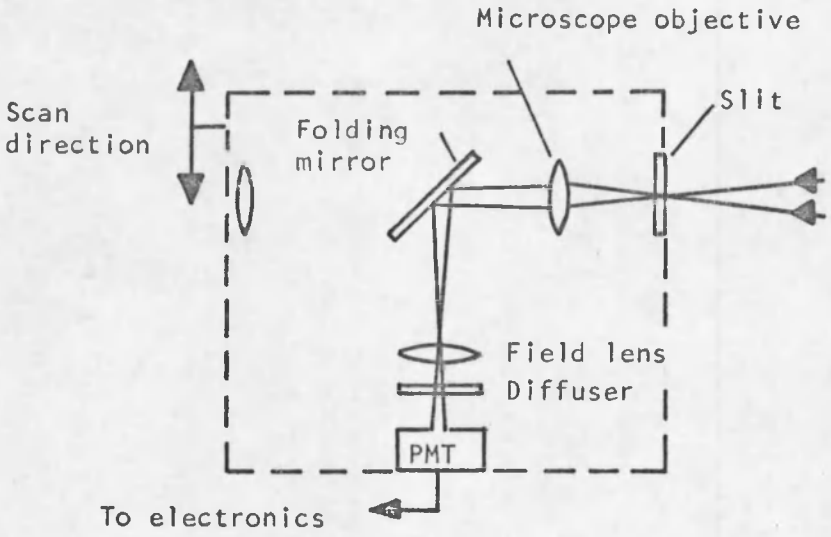

a Measuring LSF

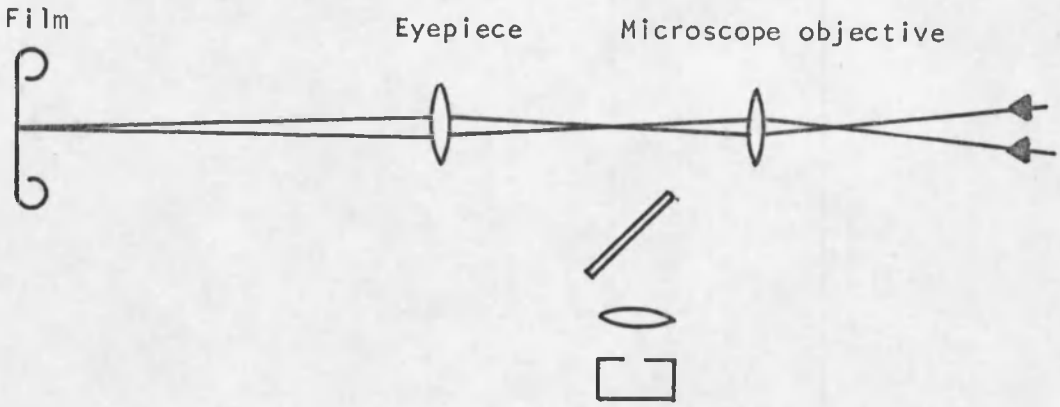

b Photographing PSF

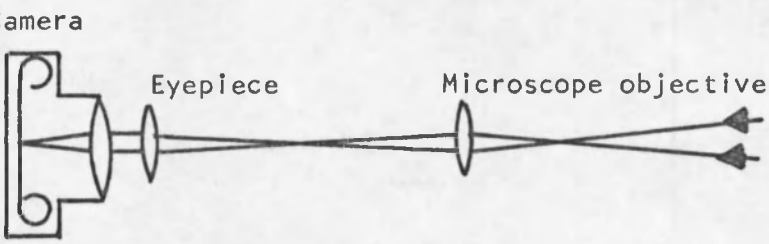

c Photographing extended object

Fig. 34. Detection Stage Configurations.

film. Photographing the image of the extended object requires the same microscope arrangement; however, rather than being projected with the eyepiece, the image is focused onto the film with a camera lens.

Figure 35 shows the detection stage mounted on the optical bench. Two dial indicators monitor the position of the stage along the optical axis (focal position) and the position of the stage transverse to the optical axis (scan position). The focal position indicator is graduated in 10-μm increments, corresponding to a $\lambda/60$ system focal shift, and the scan position indicator is graduated in 1.25-μm increments. The 10X Nikon microscope objective is of exceptionally high quality. A 6X eyepiece was used for both the point spread function and target photographs. The microscope, photomultiplier tube, and slit are mounted on a ball slide assembly that is positioned with a micrometer (not visible in photograph).

Line Spread Function Measurement

As discussed in Chapter II, the $\phi = 0°$ and $\phi = 45°$ cross sections of the OTF change significantly when aberrations are introduced into one aperture element. In order to measure the transfer function in both directions, the aberrated element is oriented at 45° to the scan axis (see Fig. 36). For the $\phi = 45°$ measurement the slit is oriented at 90° to the scan direction, and for the $\phi = 0°$ measurement the slit is oriented at 45° to the scan direction.

The 3.5-μm-wide by 1-cm-long slit is mounted on a stage that can be adjusted along the optical axis in order to focus the slit. Light passing through the slit is brought to a focus in the vicinity of a

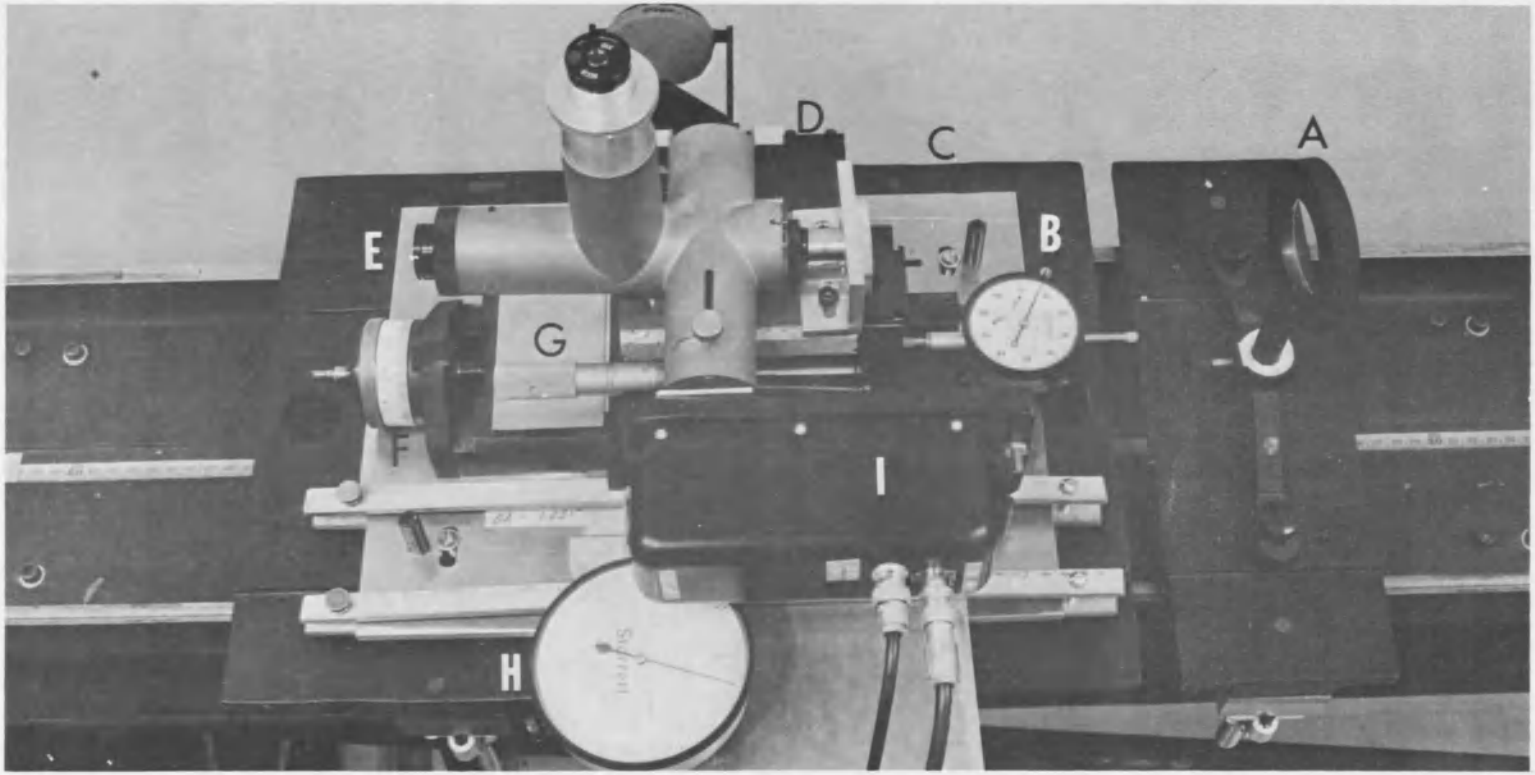

Fig. 35. Photograph of the Detection Stage.

(A) Astigmatism corrector plate, (B) dial indicator to monitor system focal position, (C) slit, (D) microscope objective, (E) eyepiece, (F) system focus control, (G) slit focus control, (H) dial indicator to monitor scan position, (I) PMT housing.

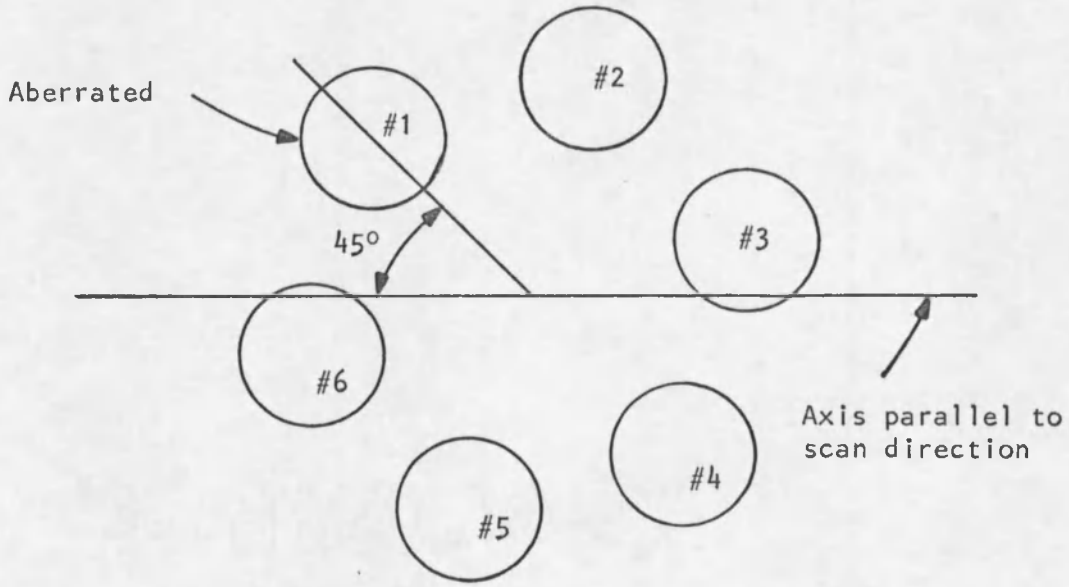

a. Pupil plane

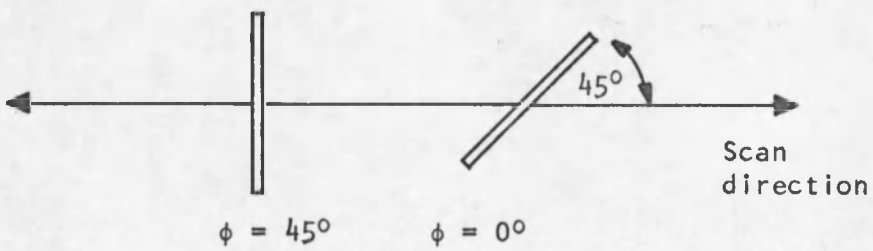

b. Image plane

Fig. 36. Geometry for OTF Measurement.

field lens (Fig. 34) by the microscope objective. The field lens images the pupil of the microscope objective onto the diffuser. Since the laser beam is linearly polarized and the 1P21 photomultiplier tube is polarization sensitive, a depolarizer is required. A diffuser made of a sandwich of vellum sheets provides the scattering elements necessary to depolarize the beam.

The signal from the photomultiplier represents the value of the line spread function for a particular scan position. The entire line spread function is generated by scanning the slit, microscope, and photomultiplier tube.

Sampling Rate. According to the sampling theorem, a band-limited function can be completely specified by its values at regularly spaced points if the sampling interval is no larger than (Goodman, 1968, pp. 21-25)

$$\Delta x_c = 1/2\nu_c,$$

where ν_c is the frequency of the highest spatial frequency component in the function. For an $f/10$ optical system, incoherently illuminated with $\lambda = 632$ nm, the cutoff frequency is 160 mm^{-1}. Therefore, because an image formed with such a system will have no components higher than 160 mm^{-1}, the maximum allowable sampling interval is 3.1 μm. The line spread function measurements are made with a 2.5-μm sampling interval for the $\phi = 45°$ direction and a 1.8-μm sampling interval for $\phi = 0°$.

Truncation of the Line Spread Function. Since the line spread function is of infinite extent, an infinite number of samples is needed to determine it completely. If the function is truncated, then the

actual line spread function, LSF(x), is approximated by a function of the form

$$\mathrm{LSF}'(x) = \mathrm{LSF}(x) \cdot \mathrm{rect}(x/a),$$

where rect(x/a) is 1 inside and 0 outside of the interval $-a/2 < x < a/2$. The Fourier transform of LSF(x) is the transfer function. Therefore

$$\mathrm{OTF}'(\nu) = K[\mathrm{OTF}(\nu) * \mathrm{sinc}(ax)],$$

where K is a normalization constant that sets $\mathrm{OTF}'(\nu = 0) = 1$. As the width of rect($x/a$) increases, the width of sinc(ax) decreases, and for sufficiently large values of a, $\mathrm{OTF}'(\nu) \simeq \mathrm{OTF}(\nu)$ with negligible error.

Rabedeau (1969) determined that, for circularly symmetric pupils with small or well balanced aberrations, a significant ($\sim$4%) error in the OTF exists even if the line spread function is not truncated until it reaches ½% of its maximum value. The error is largest at very low spatial frequencies ($\nu < 0.1$). If the LSF is truncated at its ½% values, then 20 sample points at the critical sampling interval are required.

Rabedeau's results do not necessarily apply to synthetic aperture systems because the point spread functions are generally much more complicated than for circularly symmetric systems. Therefore the effect of truncating the synthetic aperture line spread function was experimentally determined. The line spread function corresponding to the $\phi = 0°$ transfer function was measured and then truncated to varying degrees. The transfer functions calculated from the truncated line spread function were compared, and it was determined that the line spread function should be measured out to 90 μm on each side of its center. Truncation

at this point produces an error in the calculated MTF (see Fig. 37) that is less than 0.01 for normalized spatial frequency components greater than 0.1. The 180-μm sampled region extends out to the third dark ring of the $f/40$ pupil element Airy pattern and the fourteenth dark ring of the $f/10$ synthesized pupil Airy pattern. At the truncation point the value of the line spread function is about 0.5% of its peak value.

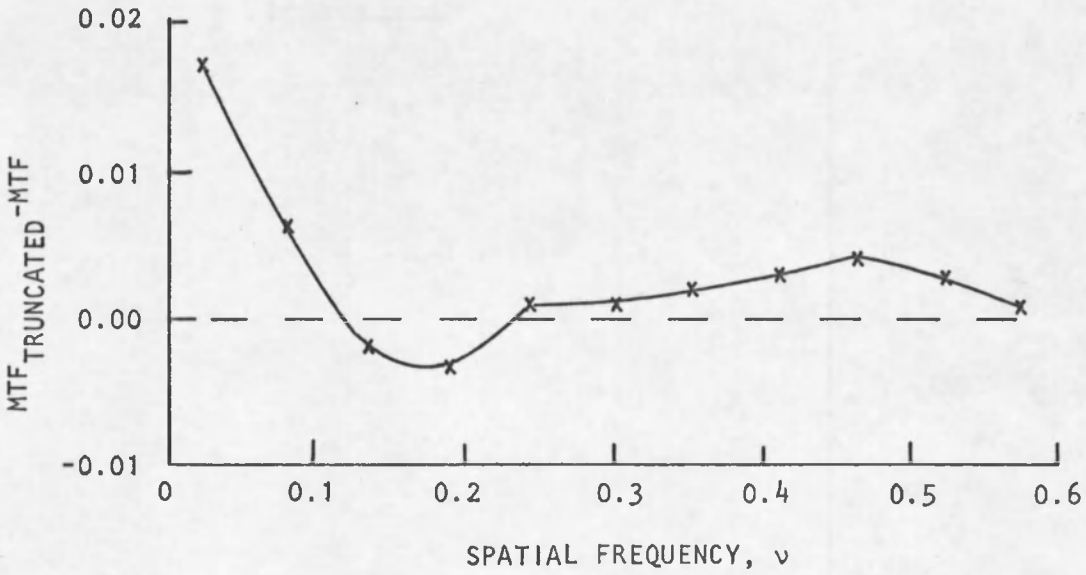

Fig. 37. Error in MTF Calculated from a Truncated Line Spread Function.

Effect of Slit Width and Point Source Diameter. The finite size of the point object and the finite width of the sampling slit affect the measured line spread function and therefore the transfer function.

The line spread function, LSF(x), is measured by scanning the point spread function, PSF(x,y), with a slit, $\delta(x)$, oriented parallel to

the y axis:

$$\mathrm{LSF}(x) = \mathrm{PSF}(x,y) \;**\; \delta(x),$$

where ** denotes a two-dimensional convolution. If the object, $\mathcal{O}(x,y)$, has finite extent, then its image is

$$\mathrm{PSF}'(x,y) = \mathcal{O}(x,y) \;**\; \mathrm{PSF}(x,y).$$

Furthermore, if the slit has a finite width, then the measured line spread function is

$$\mathrm{LSF}'(x) = \mathrm{PSF}'(x,y) \;**\; \mathrm{rect}(x/b),$$

where b is the slit width. Therefore,

$$\mathrm{LSF}'(x) = \mathcal{O}(x,y) \;**\; \mathrm{PSF}(x,y) \;**\; \mathrm{rect}(x/b).$$

Since $\mathrm{rect}(x/b) = \mathrm{rect}(x/b) \;**\; \delta(x)$, the last expression may be written

$$\begin{aligned}\mathrm{LSF}'(x) &= \mathcal{O}(x,y) \;**\; \mathrm{PSF}(x,y) \;**\; \delta(x) \;**\; \mathrm{rect}(x/b) \\ &= \mathcal{O}(x,y) \;**\; \mathrm{LSF}(x) \;**\; \mathrm{rect}(x/b).\end{aligned}$$

The cross section of the experimentally determined transfer function in the ν_x direction is the Fourier transform of $\mathrm{LSF}'(x)$

$$\mathrm{OTF}'(\nu_x,0) = \mathrm{OTF}(\nu_x,0) \cdot \mathcal{F}\{\mathcal{O}(x,y)\} \cdot \mathrm{sinc}(b\nu_x) \cdot \delta(\nu_y), \tag{18}$$

where $\mathrm{sinc}x \equiv (\sin\pi x)/\pi x$. Hence the experimentally determined OTF is the actual OTF multiplied by two factors; one depends on the object distribution and the other on the slit width.

First consider the error due to the object distribution. The object is a 5-μm-diameter pinhole illuminated by a focused laser beam. The laser beam has a Gaussian amplitude distribution that falls to its $1/e$ point when the beam diameter is 0.8 mm (according to the manufacturer's literature). Since the laser has a beam divergence of 1.1 mrad and the microscope objective is 150 mm from the laser, the $1/e$ point beam diameter at the objective is 0.95 mm. Hence, the amplitude distribution at the pupil of the objective can be expressed as

$$P(x',y') = \exp\left[-\pi\left(\frac{\sqrt{x'^2+y'^2}}{1.9\ \text{mm}}\right)^2\right].$$

The amplitude distribution at the focal plane of the objective is

$$\begin{aligned} A(x,y) &= \mathcal{F}\{P(x',y')\} \\ &= \exp\left[-\pi\left(\frac{1.9\ \text{mm}}{\lambda f}\sqrt{x^2\quad y^2}\right)^2\right], \end{aligned}$$

where f is the focal length of the objective. Substituting λ = 633 nm and f = 4 mm, the intensity distribution at the focal plane is

$$\begin{aligned} \mathcal{O}(x,y) &= A(x,y)A^*(x,y) \\ &= \exp\left[-\pi\left(\frac{1}{0.945\ \mu\text{m}}\sqrt{x^2\quad y^2}\right)^2\right]. \end{aligned}$$

When modified by the 5-μm pinhole, this focused Gaussian beam forms the "point" source for the synthetic aperture system. Since the effective diameter of the Gaussian beam is only 2 μm (at the 4% intensity points), the effect of the pinhole is insignificant in defining the

intensity distribution of the source. Therefore, the finite source size factor in Eq. (18) is

$$\mathcal{F}\{\mathcal{O}(x,y)\} = \exp\{-\pi[0.945\ \mu m \times (\nu_x^2 + \nu_y^2)^{\frac{1}{2}}]^2\}.$$

If $\nu_y = 0$ and ν_x is normalized to the cutoff frequency for an $f/10$ system, then

$$\mathcal{F}\{\mathcal{O}(x,y)\} = \exp[-\pi(0.15\ \mu m \times \nu_x)^2]. \quad (19)$$

This function shows the fractional reduction in the MTF due to the source size and is plotted in Fig. 38.

The effect of the slit width on the MTF is expressed by the $\text{sinc}(b\nu_x)$ function. If the slit width is 3.5 μm and ν_x is normalized to the cutoff frequency for an $f/10$ system, then the effect of the slit width is $\text{sinc}[(0.555\ \mu m)\nu_x]$. This factor is also plotted in Fig. 38. The combined effect is just the product of the two curves.

The major modification to the MTF comes from the slit. In order to correct this error, the MTF curves obtained experimentally are multiplied by a correction function equal to $1/\text{sinc}(0.58\ \mu m \times \nu_x)$, which very closely approximates the inverse of the net effect curve in Fig. 38. The correction function is plotted in Fig. 39.

Electronics. Owing to bench vibrations and atmospheric turbulence, the amount of light passing through the slit varied significantly with time. The bench vibrations were of relatively high frequency (> 40 Hz), whereas the atmospheric turbulence was of low frequency (0.1 to 10 Hz). These produced intensity fluctuations at the PMT that were typically 10% but often went as high as 30%. Intensity variations due to

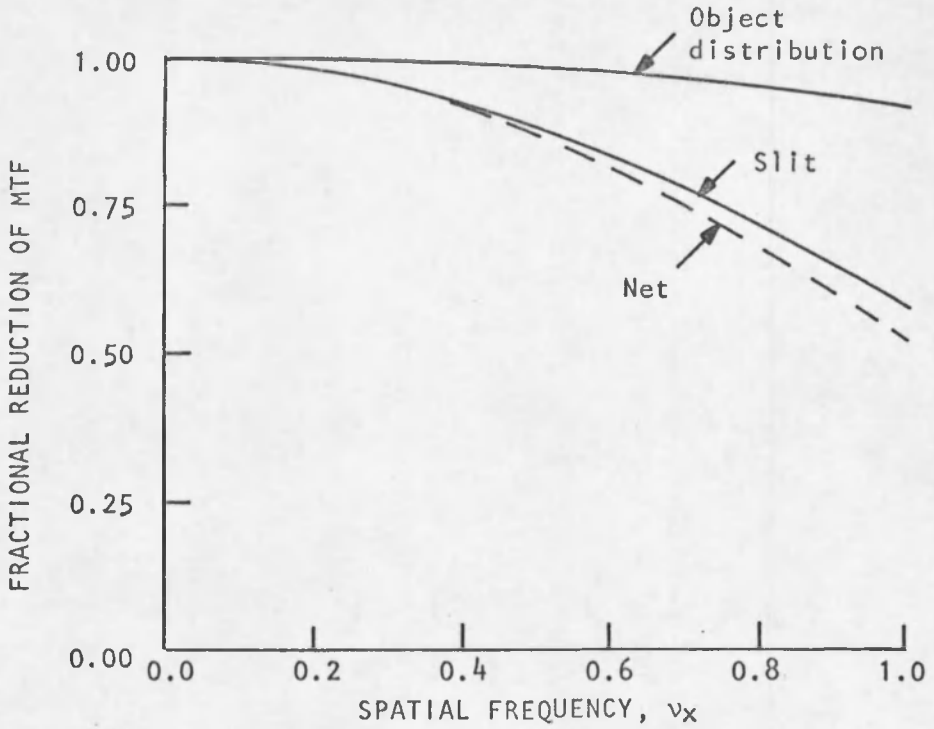

Fig. 38. Reduction of MTF Due to Slit Width and Object Distribution.

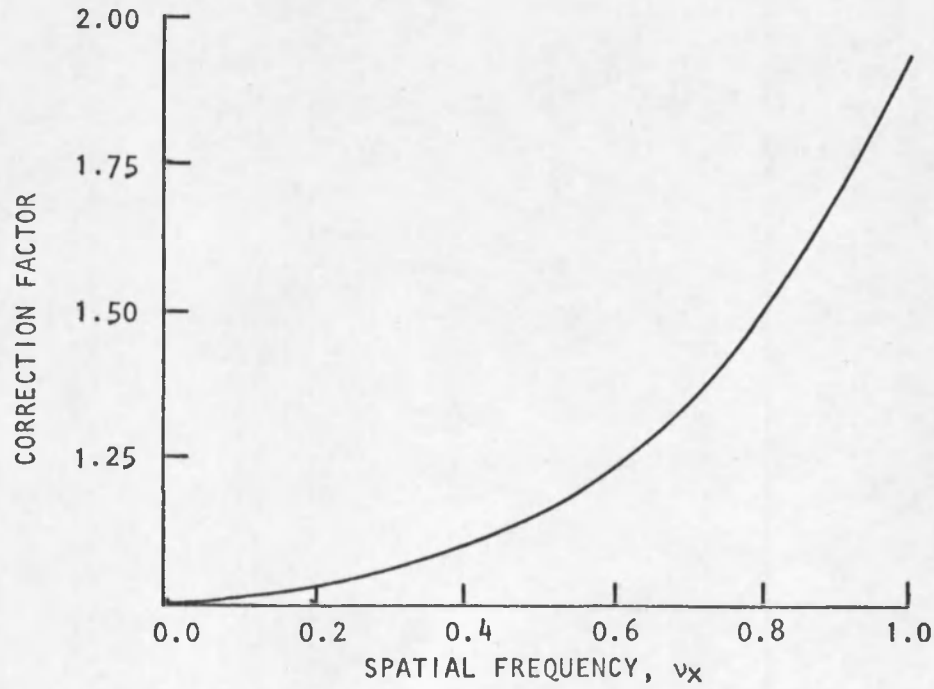

Fig. 39. MTF Correction Function.

the laser were insignificant (less than 0.3%) even over periods as long as 15 min.

Assuming that the variations due to vibration and turbulence have a zero mean relative to the actual value of the line spread function, the noise can be removed by integrating the signal for a sufficiently long period. The system for performing this function is outlined in Fig. 40. The PMT produces a current signal that is converted to a voltage signal by a Keithley Model 414 Micro-Micro Ammeter. The noisy signal is then fed to an electronic integrator that is controlled by two electronic timers. Timer 1 regulates the integration time by opening and closing a switch at the integrator's input. Timer 2 shorts out the integrating capacitor prior to the beginning of a new integration cycle. The output from the integrator is displayed on a Weston Model 1242 Digital Voltmeter.

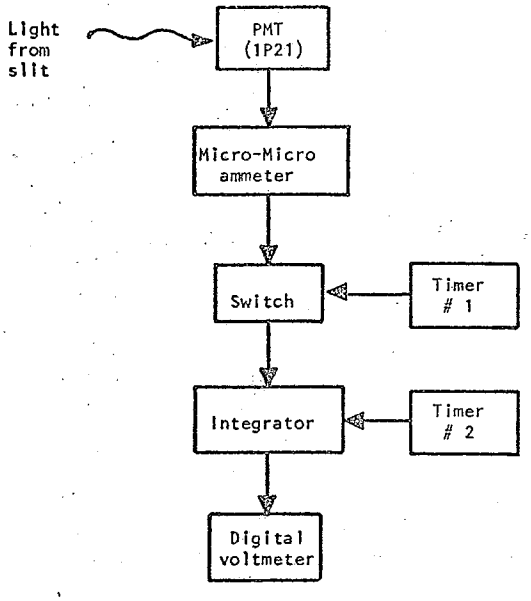

Fig. 40. Electronics.

This signal integration scheme worked remarkably well in reducing the random signal fluctuations. For an integration time of 15 sec the noise was typically 1% of the signal. The linearity of the PMT, ammeter, and integrator was sufficiently accurate for the line spread function measurements.

OTF Calculation. The optical transfer function was calculated from the measured line spread function using a fast Fourier transform routine. The program then multiplied the calculated transfer function by the correction function (Fig. 39). The program used for this calculation is described further in Appendix B.

Photographing the Point Spread Function and the Extended Target

Photographs of the point spread function and the extended target were made using the experimental arrangement shown in Fig. 34. The point spread was focused by the detection stage microscope at a plane located 700 mm from the eyepiece. Film placed in this plane recorded the 125X magnified point spread function. When the point spread function was focused at this plane, the image of the target was located at infinity (owing to the positioning of the target relative to the pinhole at the illumination stage). The target image was photographed using a 35-mm focal length lens focused at infinity. With this lens the film recorded the target at 8X magnification.

The effect of the microscope and camera optics on the image quality of the photographs was insignificant. The microscope objective (10X Nikon; N.A. = 0.25) was of very high quality, and its pupil was underfilled by the $f/10$ synthetic aperture beam. Similarly, the maximum

spatial frequency content of the target image in the focal plane of the $f/3.5$ camera lens was only 20 mm^{-1}, compared to the 250 mm^{-1} that the lens can easily resolve.

The photographs were made with Kodak Plus-X film developed in Kodak Microdol-X developer. The effect of this film on the recorded image quality is quite small. At 20 cycles/mm, Plus-X film has a transfer function value of approximately 0.85. (This value was estimated from transfer function curves for similar developers as described by Eastman Kodak Company, 1967.)

The photographs in this report show the point spread function enlarged 450X and the extended target enlarged 48X, except as otherwise noted.

Experimental Procedure

The procedure followed in a typical data run is outlined below. It is significant that (a) the exact aberration introduced was always known and recorded on an interferogram (except for piston error and tilt), and (b) the focus of the system was identical for recording of the point spread function, line spread function, and image of an extended object.

(1) The magnified point spread function of the aberrated aperture element was observed, and the aberration generator was adjusted until spherical aberration, coma, astigmatism, and defocus were zero.

(2) The tilt and piston errors were removed using a technique described earlier in this chapter.

(3) The desired aberration was introduced with the aberration generator.

(4) The telescope objective was replaced with the signal arm mirror (see Fig. 26) and an interferogram was made of the wavefront from the aberration generator.

(5) The telescope objective was placed back into position, and the detection stage was adjusted for best focus as the magnified six-element point spread function (on a screen 700 mm from the eyepiece) was being observed.

(6) The critical focus of the array was adjusted using the fine focus technique described in Appendix C.

(7) The slit was positioned in its proper orientation in front of the microscope objective, and the slit focus control was used to bring the image of the slit into focus on the focusing screen.

(8) Using the slit focus control, the slit was moved 12.2×10^{-3} in. toward the telescope objective. This was necessary in order to position the slit in the focal plane of the synthetic aperture array. The thickness of the slit's glass substrate affected the focal position obtained in step (7).

(9) The detection stage's folding mirror was moved so that the beam coming from the microscope objective was directed to the PMT.

(10) The scanner micrometer was adjusted until the maximum voltage output from the PMT was obtained. This centered the slit on the point spread function.

(11) The total light coming through each aperture element was measured. The pinhole was adjusted at the illumination stage, if necessary, to make the total power coming through each element equal to within 25%.

(12) The scanner was moved 90 μm to one side of center. This was the position for the first measurement.

(13) After the electronics had integrated the signal for the proper time, the integrator output voltage was recorded and the scanner was moved 2.5 μm for the next reading. The readings were taken until the point spread function was scanned.

(14) The folding mirror in the detection stage was retracted, and the slit was removed so that the point spread function was imaged onto the focusing screen. Film was placed in the plane of the screen, and the point spread function was photographed.

(15) The folding mirrors on the illumination stage were moved so that the target was illuminated and was imaged through the synthetic aperture system. The camera was placed against the eyepiece in the detection stage, and the image of the extended target was photographed.

Experimental Error

There are many factors that influence the accuracy of the transfer function measurements. Two categories of error sources may be defined. The first includes the sources that produce a systematic error, and the second includes random error sources. Systematic error sources include the uniformity of pupil illumination, the accuracy of the mask geometry, the source pinhole and scanning slit size, the quality of the optical elements, the linearity of the PMT and electronics, the alignment of the scanner axes, etc. Random error sources include atmospheric turbulence and mechanical vibrations.

To evaluate the net effect of these factors, the unaberrated transfer function was measured a number of times and compared with the theoretical unaberrated transfer function (Figs. 41 and 42). Figure 41 shows that there are two spatial frequency regions where the measured $\phi = 0°$ MTF is consistently higher than the theoretical MTF. From $0.25 < \nu < 0.35$ the measured MTF is about 0.03 too large, and from $0.6 < \nu < 0.7$ it is about 0.02 too large. Likewise, there are regions in the $\phi = 45°$ MTF (Fig. 42) that vary in a consistent fashion from the theoretical MTF. From $0.2 \leq \nu \leq 0.45$ the measured MTF is about 0.03 too small, and from $0.6 < \nu < 0.75$ it is about 0.03 too large.

Both the $\phi = 0°$ and the $\phi = 90°$ MTF curves fail to go to zero at their respective cutoff frequencies. This is due to high-frequency noise in the measured line spread function, which probably is caused by small inaccuracies in positioning the scanner or by random variations in the light signal produced by atmospheric turbulence or mechanical vibrations.

Except for the regions just mentioned, the MTF curves follow the theoretical curves quite well. There is typically a 0.02 spread in the data points at a particular spatial frequency, indicating a repeatability of about ± 0.01.

The phase transfer functions exhibit small random variations. Typical maximum deviations are 0.05 cycles, although at very high spatial frequencies the PTF error at times reaches 0.1 cycle.

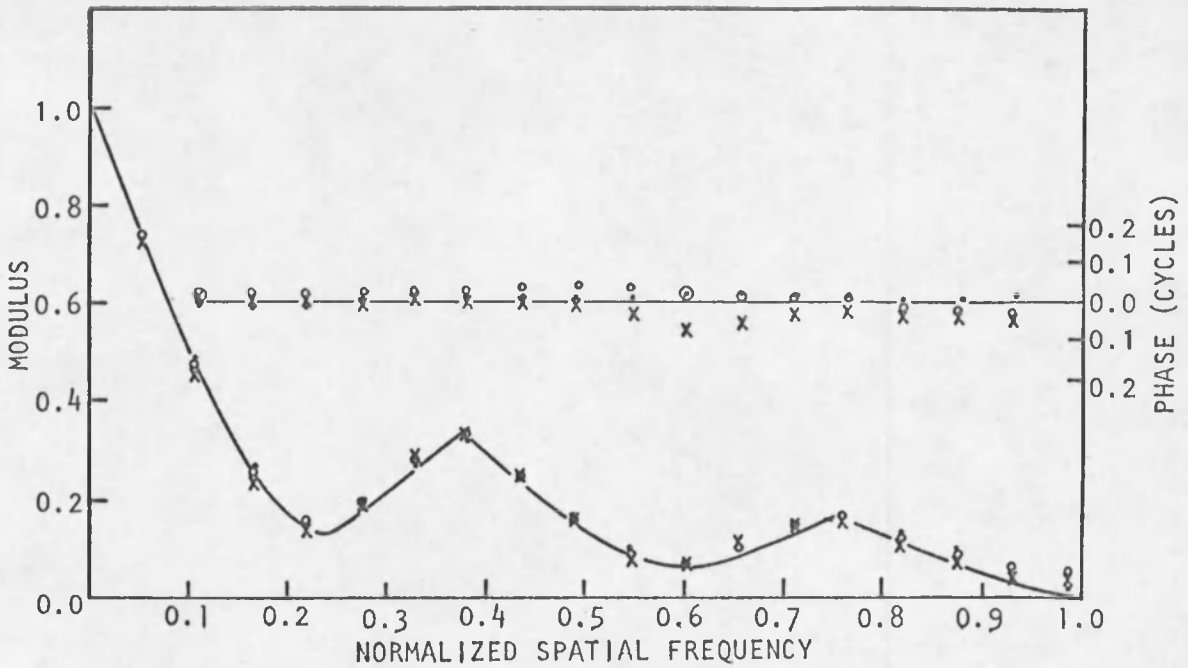

Fig. 41. The Measured ϕ = 0° Transfer Function.

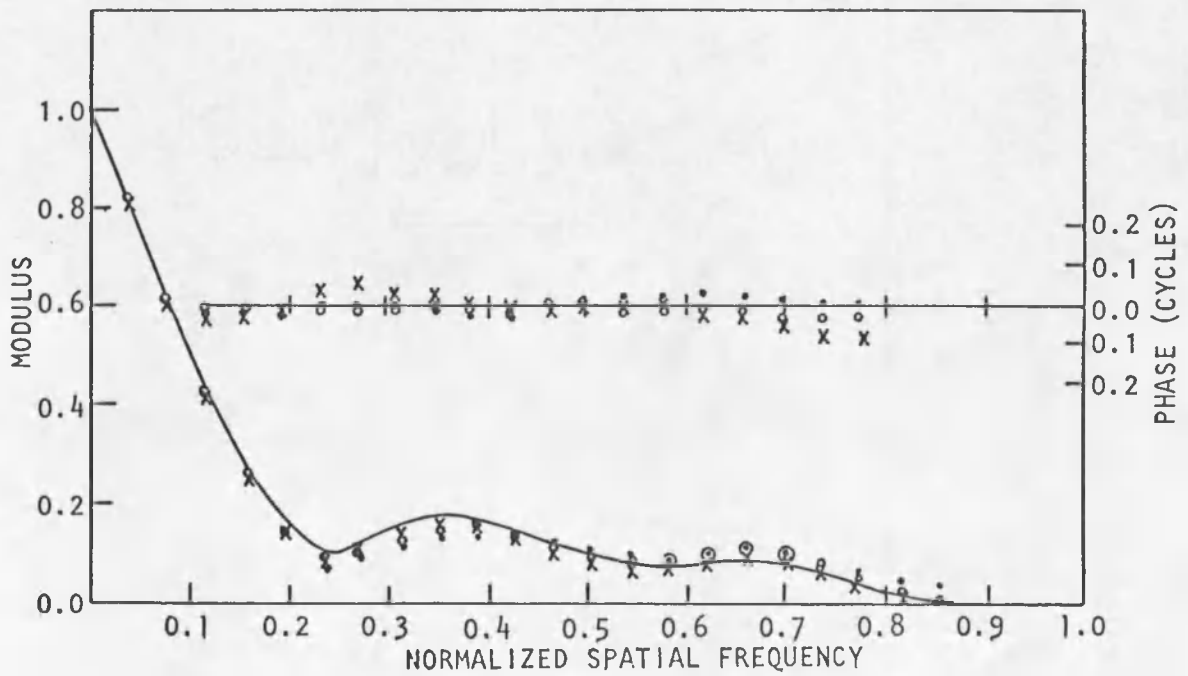

Fig. 42. The Measured ϕ = 45° Transfer Function.

CHAPTER V

RESULTS

This chapter describes the results of the computer simulation and the experimental measurements. Transfer function curves that were obtained experimentally are marked with an E. All unmarked curves were calculated using the computer program described in Chapter III. The spatial frequency axes on the transfer function curves are normalized to the cutoff frequency of an $f/10$ circular pupil (160 cycles/mm for λ = 632.8 nm). Only the $\phi = 0°$ and $\phi = 45°$ cross sections of the two-dimensional transfer function are considered. These are referred to as the $\phi = 0°$ transfer function and the $\phi = 45°$ transfer function, respectively.

The orientations of the line spread function and the extended target are defined in terms of their relationship to the transfer function. The $\phi = 0°$ (or 45°) line spread function is the inverse Fourier transform of the $\phi = 0°$ (or 45°) transfer function cross section, and is oriented perpendicular to the $\phi = 0°$ (or 45°) axis. Similarly, the images of the $\phi = 0°$ (or 45°) extended target are oriented such that the bars of the log-periodic target are perpendicular to the $\phi = 0°$ (or 45°) axis.

Three portions of the extended target are shown in this chapter. The portion that includes the $\phi = 0°$ (or 45°) log-periodic target reflects the modulation variations of the $\phi = 0°$ (or 45°) transfer

function. The other two are of general scenes and are designated by A1, A2, B1, or B2. The letter in the designation refers to the particular target section (A for airplane, B for building), and the number refers to the orientation of the target section (1 for $\phi = 0°$ and 2 for $\phi = 45°$).

Comparisons of the extended target images were made from prints that are of higher quality than the reproductions included in this chapter. As a result, some of the reproduced features do not have the clarity present in the target images.

The wavefront associated with the aberrated pupil element is described by the magnitude of its aberration coefficient, the form of the aberration (piston error, defocus, etc.), and the orientation, α, of the aberration within the pupil element; α is measured the same as ϕ, as shown in Fig. 1.

To clarify the presentation of the measured transfer function curves, two simplifications are made. First, there are no measured values shown for the $\phi = 0°$ transfer function in the region $0.25 < \nu < 0.5$, as the aberrated element does not contribute in this region. (The measured values are the same as the unaberrated theoretical values, within the error range discussed in the last chapter.) Second, the measured PTF is not shown for those cases where, for reasons of symmetry, the PTF must be zero. (The measured values vary about zero within the range mentioned in the error discussion.)

Unaberrated System

The point spread function of the $f/10$ unaberrated six-element array is shown in Fig. 43. For comparison, the spread functions of an

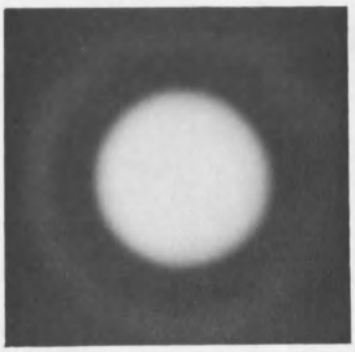

a. $f/40$ Circular Pupil.

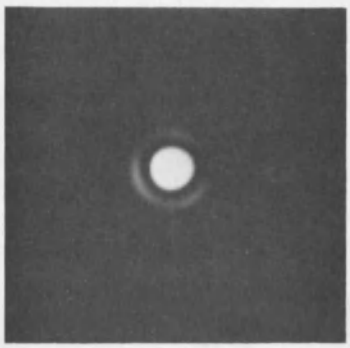

b. $f/10$ Circular Pupil.

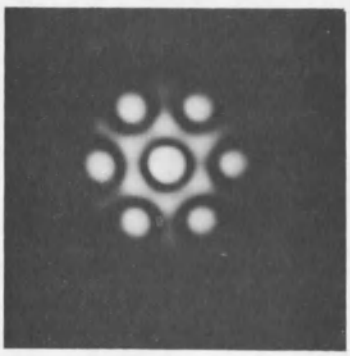

c. $f/10$ Synthetic Aperture.

Fig. 43. Unaberrated Point Spread Functions.

individual $f/40$ circular aperture element and the $f/10$ synthesized circular pupil are also shown. Both circular pupils produce Airy intensity distributions having circular symmetry, whereas the six-element array produces an intensity distribution with hexagonal symmetry.

The central core of each spread function is surrounded by a dark ring whose diameter depends on the shape and size of the pupil. The dark ring diameter for the $f/40$ circular pupil is four times the diameter for the $f/10$ circular pupil, and the diameter for the $f/10$ array is about 10% less than for the $f/10$ circular pupil. The smaller core diameter for the $f/10$ array does not imply that there is a greater concentration of energy in its core than in the core for the $f/10$ circular array. On the contrary, whereas the intensity of the first bright ring in the Airy pattern is only 4% of the peak core intensity, the intensity of each of the six subsidiary peaks for the array is 18% of the peak core intensity. Hence the concentration of energy in the core is significantly higher for the $f/10$ circular aperture even though the $f/10$ array has a slightly smaller core.

The line spread function of the circular pupil is the same in all directions. However, with the synthetic aperture array the LSF is highly dependent on the direction in which it is measured. In Fig. 44 the line spread functions for the $f/10$ circular pupil and the $f/10$ array are compared. (Each LSF has been normalized to its peak intensity.) In the case of the circular pupil, the LSF function falls off sharply until its relative intensity is less than 0.03. On the other hand, the LSF for the synthetic aperture array falls off abruptly only until the relative intensity is between 0.25 and 0.50. Beyond this point the intensity

a

f/10 circular pupil

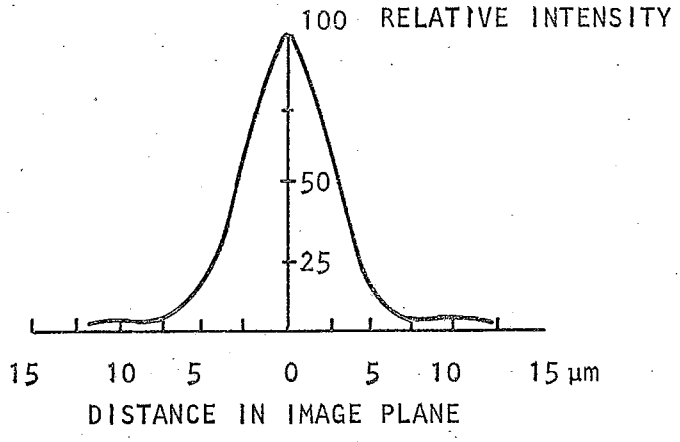

b

f/10 array, $\phi = 0°$

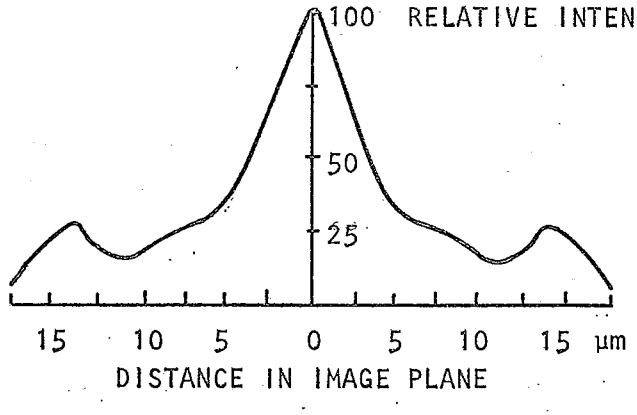

c

f/10 array, $\phi = 45°$

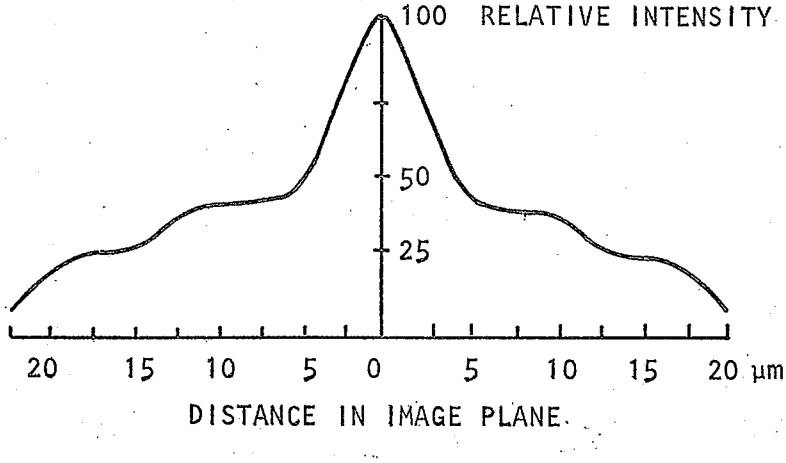

Fig. 44. Unaberrated Line Spread Functions.

decreases slowly, and there may even be secondary peaks of significant intensity (e.g., the $\phi = 0°$ LSF).

The transfer functions corresponding to the $f/40$ and $f/10$ circular pupils and the $f/10$ synthetic aperture are shown in Fig. 45. The asymmetry of the synthetic aperture transfer function is evident from the curves for the $\phi = 0°$ and $\phi = 45°$ directions. The maximum spatial frequency for the array in the $\phi = 0°$ direction is the same as for the $f/10$ circular pupil. However, in the $\phi = 45°$ direction the synthetic aperture transfer function goes to zero at a spatial frequency of 0.86.

Although the synthetic aperture array and the $f/10$ circular pupil pass spatial frequency components over nearly the same frequency region, the array reduces the contrast of these components much more than the circular pupil does. As a result, the images formed by these two systems have very different appearances. Figure 46 shows the extended target when imaged through $f/10$ and $f/40$ circular pupils, and Fig. 47 shows the target when imaged through the $f/10$ synthetic aperture array. To show the asymmetry of the array's transfer function, two orientations of the extended target are included. With each target photograph the corresponding point spread function is shown at the same scale.

The log-periodic targets are compared in Fig. 48. These targets show a maximum normalized spatial frequency of 0.23 for the $f/40$ pupil and 0.82 for the $f/10$ circular pupil. With the synthetic aperture array the maximum normalized spatial frequency is 0.74 for $\phi = 45°$ and 0.82 for $\phi = 0°$. The measured resolution was lower than the theoretical resolution for the reasons mentioned in the discussion of the test target in Chapter IV.

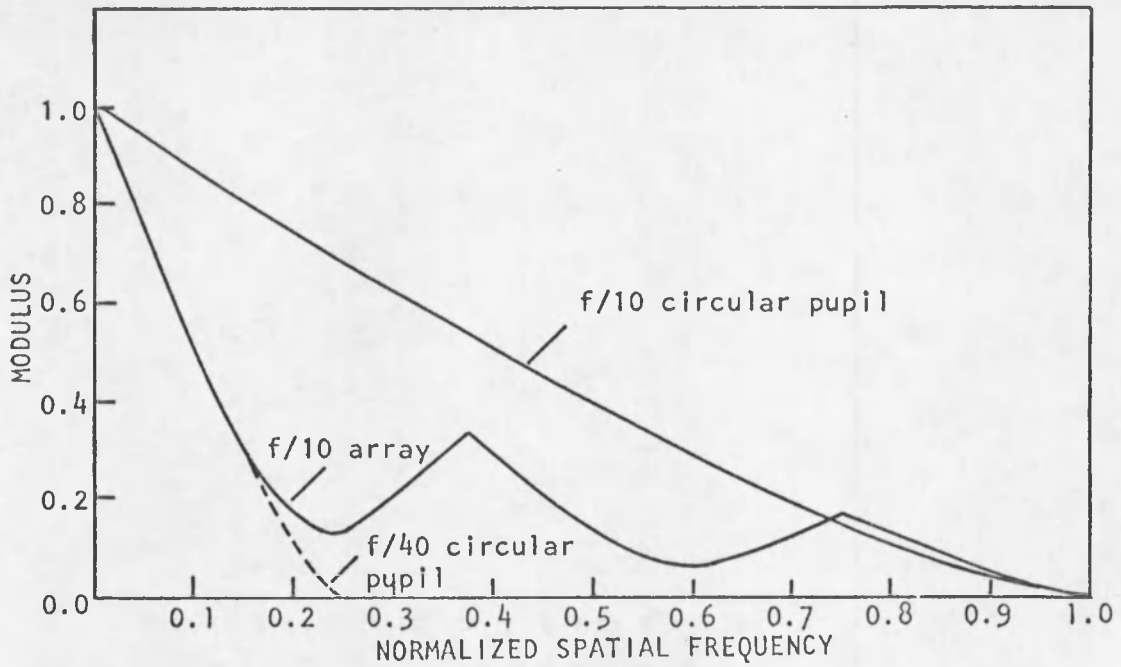

a $\phi = 0°$

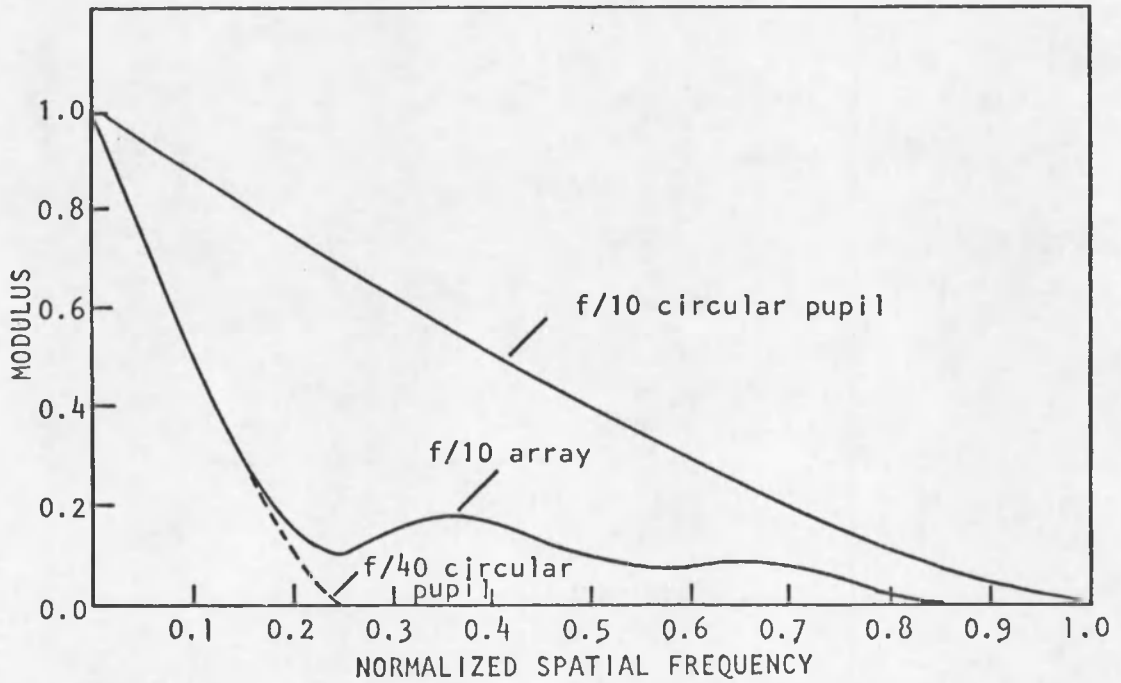

b $\phi = 45°$

Fig. 45. Unaberrated Transfer Functions.

a. f/40 Circular Pupil.

b. f/10 Circular Pupil.

Fig. 46. Unaberrated Extended Target Images, Circular Pupil.

a. $\phi = 0^{\circ}$.

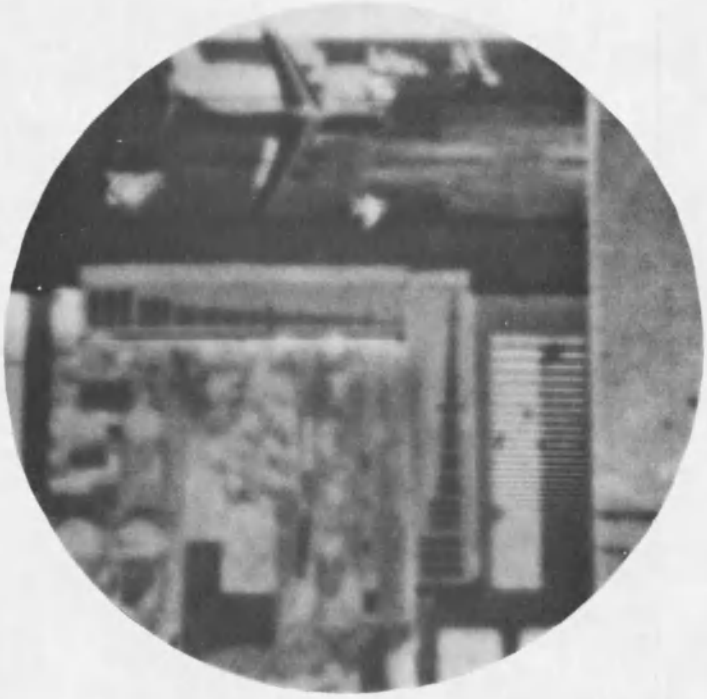

b. $\phi = 45^{\circ}$

Fig. 47. Unaberrated Extended Target Images, $f/10$ Array.

Original

$f/10$ circular pupil

$f/40$ circular pupil

$\phi = 0^{\circ}$ $f/10$ array

$\phi = 45^{\circ}$

Fig. 48. Unaberrated Images of Log-Periodic Target (82X).

The asymmetry of the synthetic aperture transfer function is further illustrated in the bottom photographs in Fig. 49. The railroad track just below the right side of the large building is resolved for $\phi = 0°$ but not for $\phi = 45°$. Similarly, the stripes on top of the railroad car are resolved for $\phi = 45°$ but not for $\phi = 0°$. Both of these features are well resolved with the $f/10$ circular pupil but are unresolved with the $f/40$ circular pupil.

In Fig. 50 the leading edge of the left wing of the large aircraft is sharp for the $f/10$ circular pupil but very fuzzy for the $f/40$ circular pupil. When imaged through the synthetic aperture array, this edge appears significantly sharper for the $\phi = 0°$ orientation than for the $\phi = 45°$ orientation. However, a sharper edge is produced with either array orientation than with the $f/40$ circular pupil.

The synthetic aperture array is also different from the circular pupil in that it produces several interesting image artifacts. These artifacts are most noticeable with images of edges and linear objects. Consider the line spread functions shown in Fig. 44. Whereas the circular pupil's LSF falls monotonically to a low level, the LSF of the array levels off when the normalized intensity is between 0.25 and 0.5. Hence, when adjacent dark and bright regions are imaged by the array, there will be a distinct gray band separating the two regions.

This effect is noticeable in the series of photographs in Fig. 49. The upper edge of the building gradually changes from dark to white for the circular pupil photographs. On each photograph two lines are drawn to indicate the geometric width of the building. The apparent width is smaller for the $f/40$ circular pupil than for the $f/10$ circular

Original $f/10$ circular pupil $f/40$ circular pupil

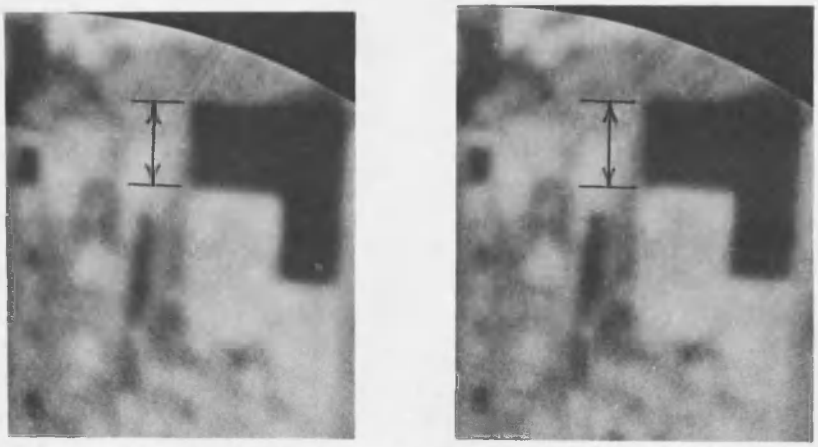

$\phi = 0^{\circ}$ $\phi = 45^{\circ}$

$f/10$ array

Fig. 49. Unaberrated Images of Target Section B (82X).

Original

$f/10$ circular pupil

$f/40$ circular pupil

$\phi = 0^{o}$

$\phi = 45^{o}$

$f/10$ array

Fig. 50. Unaberrated Images of Target Section A (82X).

pupil owing to the wider line spread function for the $f/40$ pupil. With the synthetic aperture array the transition is in distinct steps, and there is an intermediate level of gray that appears on the dark side of the geometric edge positions. The apparent width of the building in this case is nearly the same as the actual width if the edge of the building is measured from the boundary between the light and gray regions.

Another interesting artifact can be seen in the lower spatial frequency regions of the log-periodic target (Fig. 48). There appear to be faint bright lines between adjacent bright bars in the 0.19 to 0.23 normalized spatial frequency region. These faint lines are artifacts that also are produced by the wide skirts of the synthetic aperture's line spread function. In Fig. 51 two line spread functions are overlapped to illustrate the cross section of an image of two line objects. For the $\phi = 0°$ LSF, a strong secondary peak is present between the two main peaks for a line separation of 28 μm (corresponding to a normalized spatial frequency of 0.23). Similarly, a weak secondary peak is formed for the $\phi = 45°$ LSF when the lines are separated by 29 μm (corresponding to a spatial frequency of 0.21). This artifact will be called "double imaging." It is most noticeable when high-contrast periodic lines are imaged through the synthetic aperture array. Low-contrast objects, such as the three-bar targets, should also produce this artifact. However, the additional line in this case is of such low contrast that it cannot be detected.

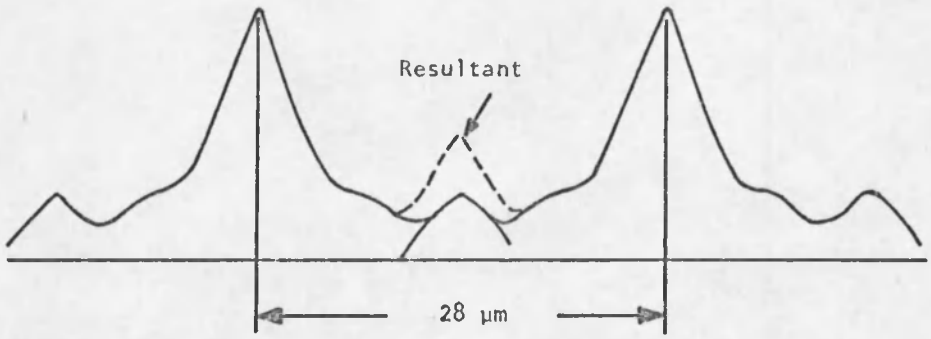

a ϕ = 0° LSF

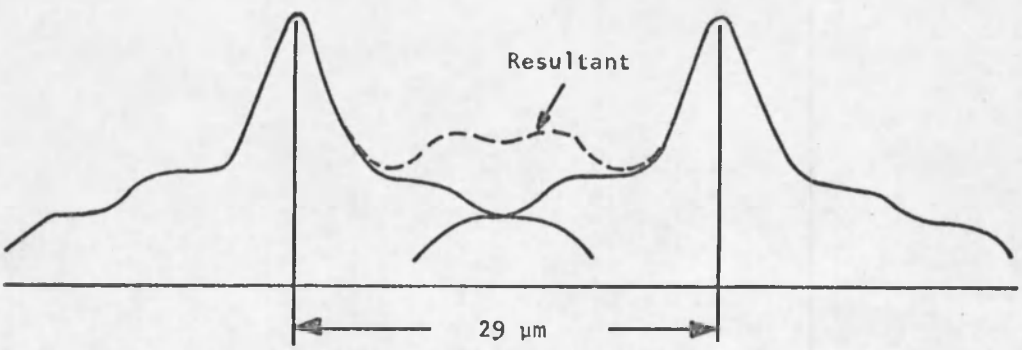

b ϕ = 45° LSF

Fig. 51. Addition of Two Line Spread Functions to Illustrate Double Imaging.

Aberrated System

System Defocus

The introduction of system defocus into the synthetic aperture array produces the point spread functions shown in Fig. 52. Although there is little if any change with 0.25λ of defocus, the six secondary peaks are elongated radially with 0.50λ of defocus. Further defocusing continues to shift light from the central core and its surrounding hexagonal plateau to the outer structure of the pattern. With 1.5λ of defocus the central core is very dim and there appears to be no light in the region of the original plateau. The hexagonal symmetry of the pattern is maintained for all magnitudes of system defocus since it is an aberration that is symmetrical with respect to the array.

System defocus reduces the low and high spatial frequency components more rapidly than the middle spatial frequencies. Figure 53 shows that the MTF is reduced by less than 0.02 for 0.25λ of defocus, whereas it is reduced by as much as 0.1 for 0.5λ of defocus. With 0.75λ of defocus, the MTF has a value less than 0.05 for more than half of the passbands in the $\phi = 0°$ curve and for more than three fourths of the passband in the $\phi = 45°$ curve. The phase transfer function is zero since system defocus is a symmetrical aberration with respect to the array.

Figures 54 through 56 show target sections for various amounts of system defocus. The change in the log-periodic target is evident when 0.5λ of defocus is introduced. With this amount of aberration the stripes on the railroad car (target section A2) and the railroad track (target section A1) cannot be resolved. With 0.75λ of defocus only the

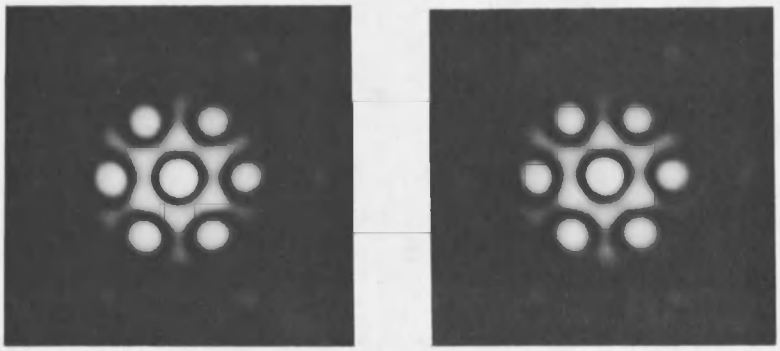

$W_{20}' = 0\lambda$ 0.25λ

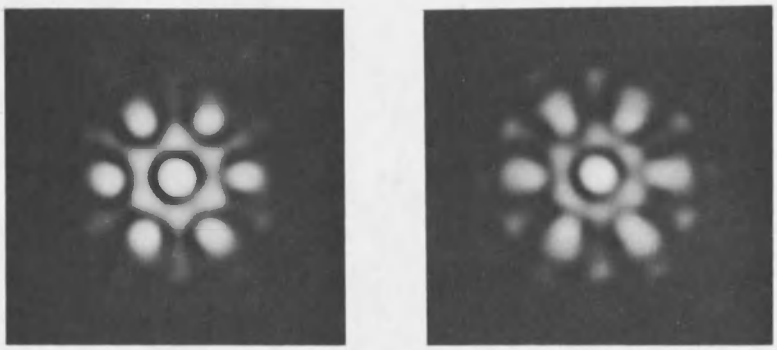

0.5λ 0.75λ

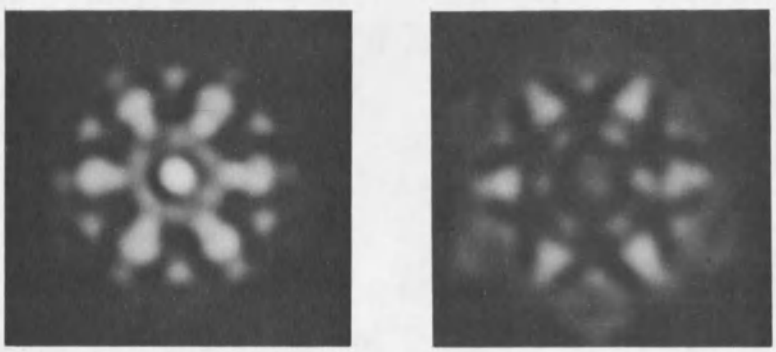

1.0λ 1.5λ

Fig. 52. PSF for System Defocus.

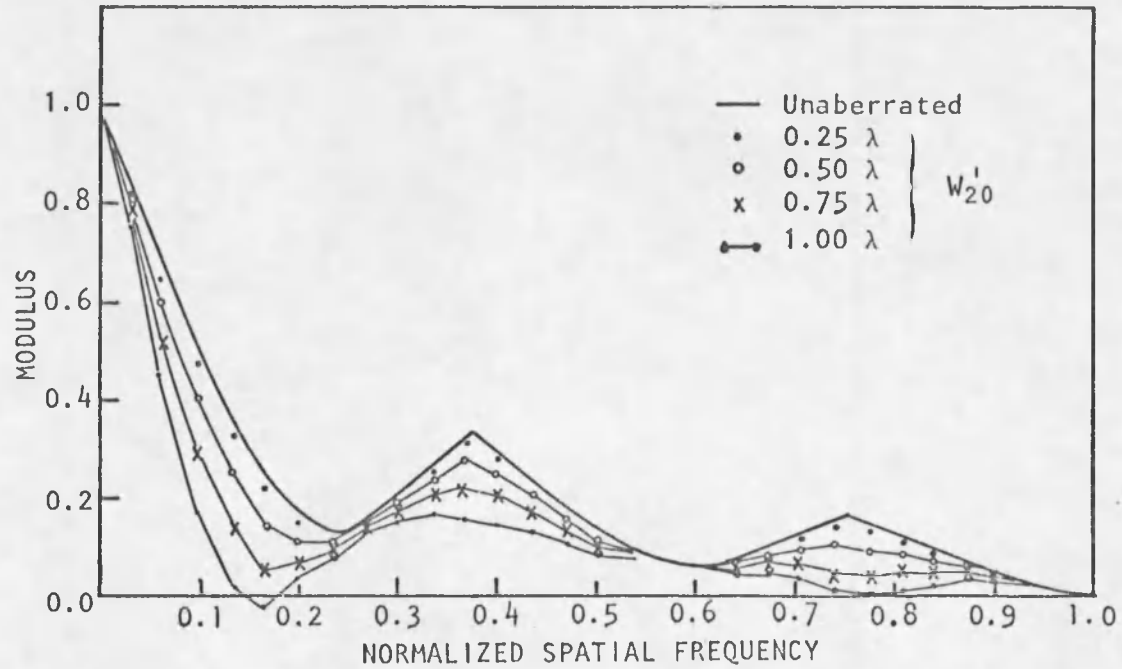

a $\phi = 0°$

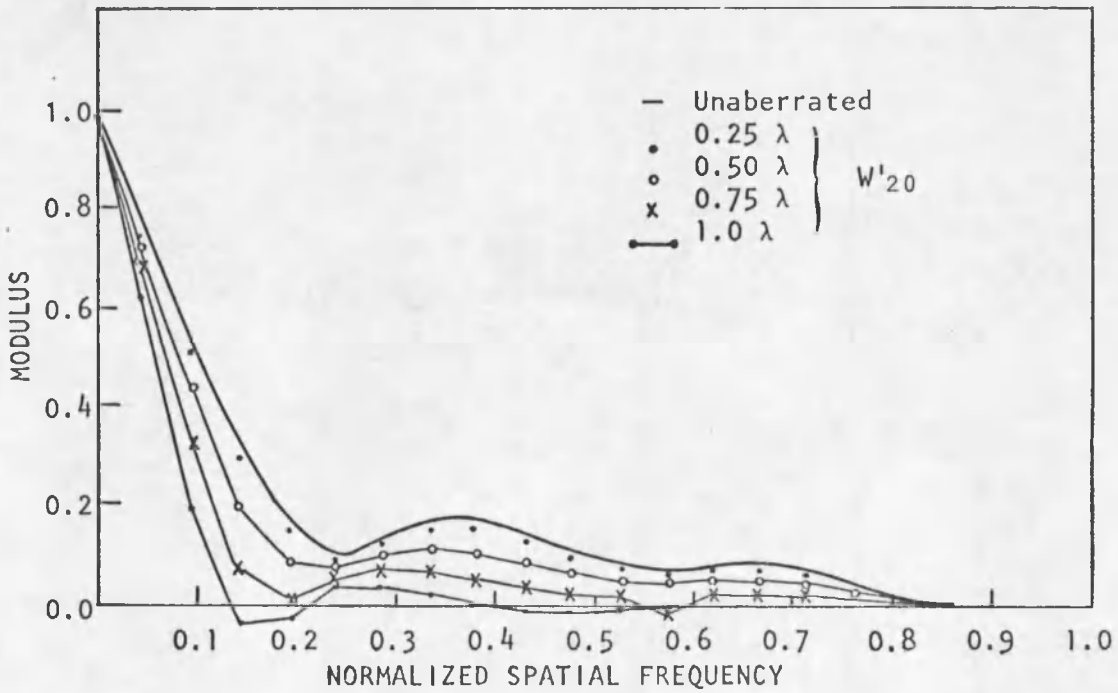

b $\phi = 45°$

Fig. 53. Transfer Functions for System Defocus.

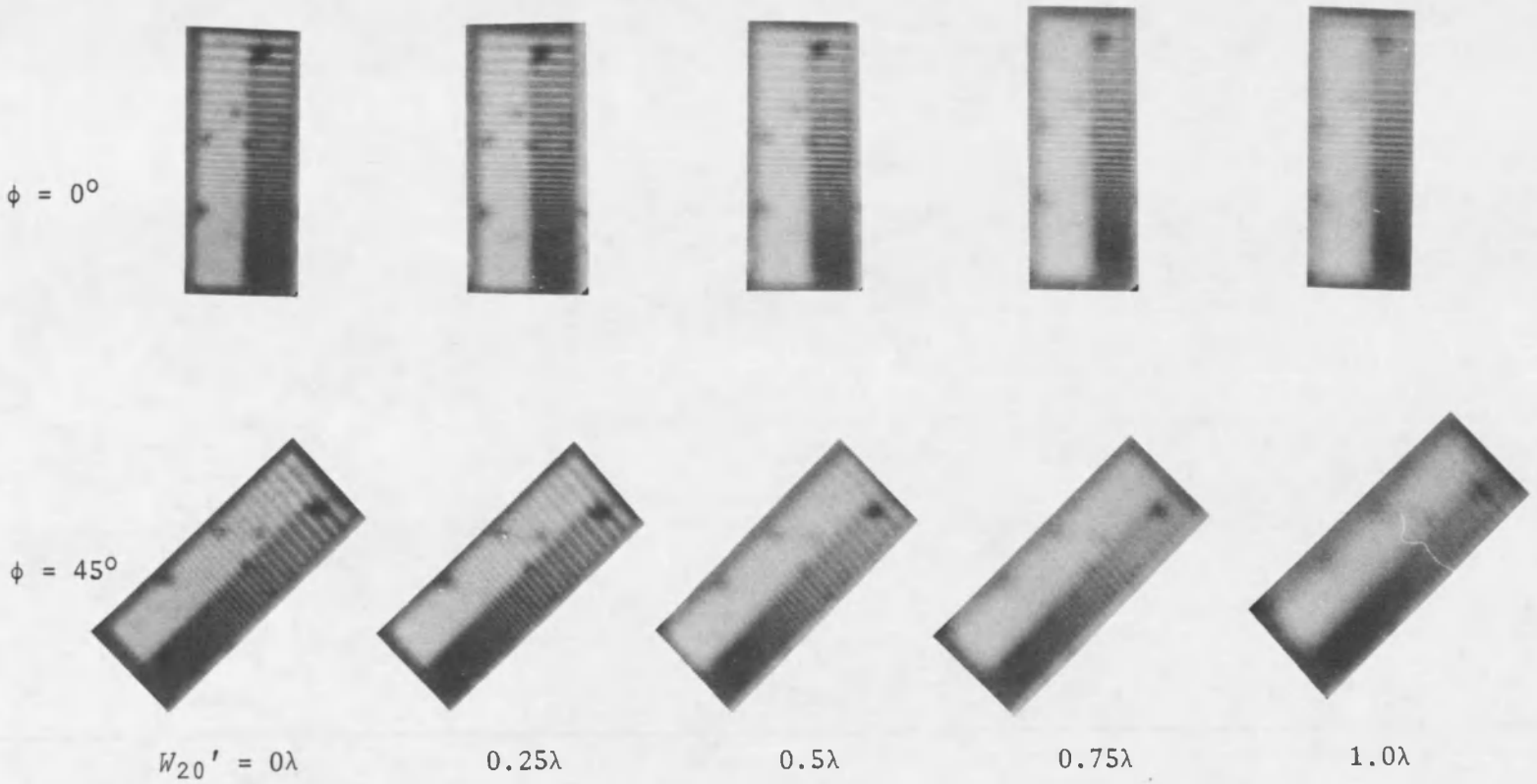

Fig. 54. Log-Periodic Target for System Defocus.

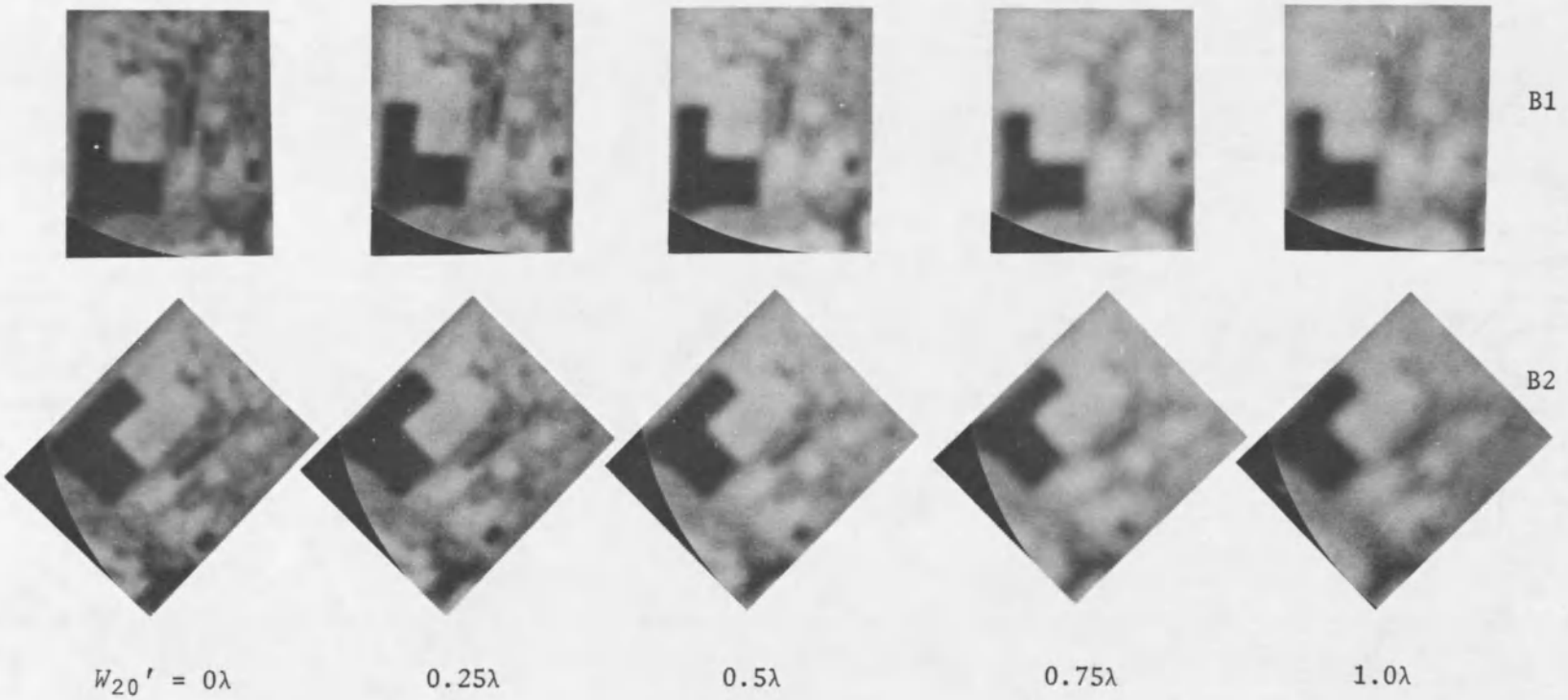

Fig. 55. Target Section B for System Defocus.

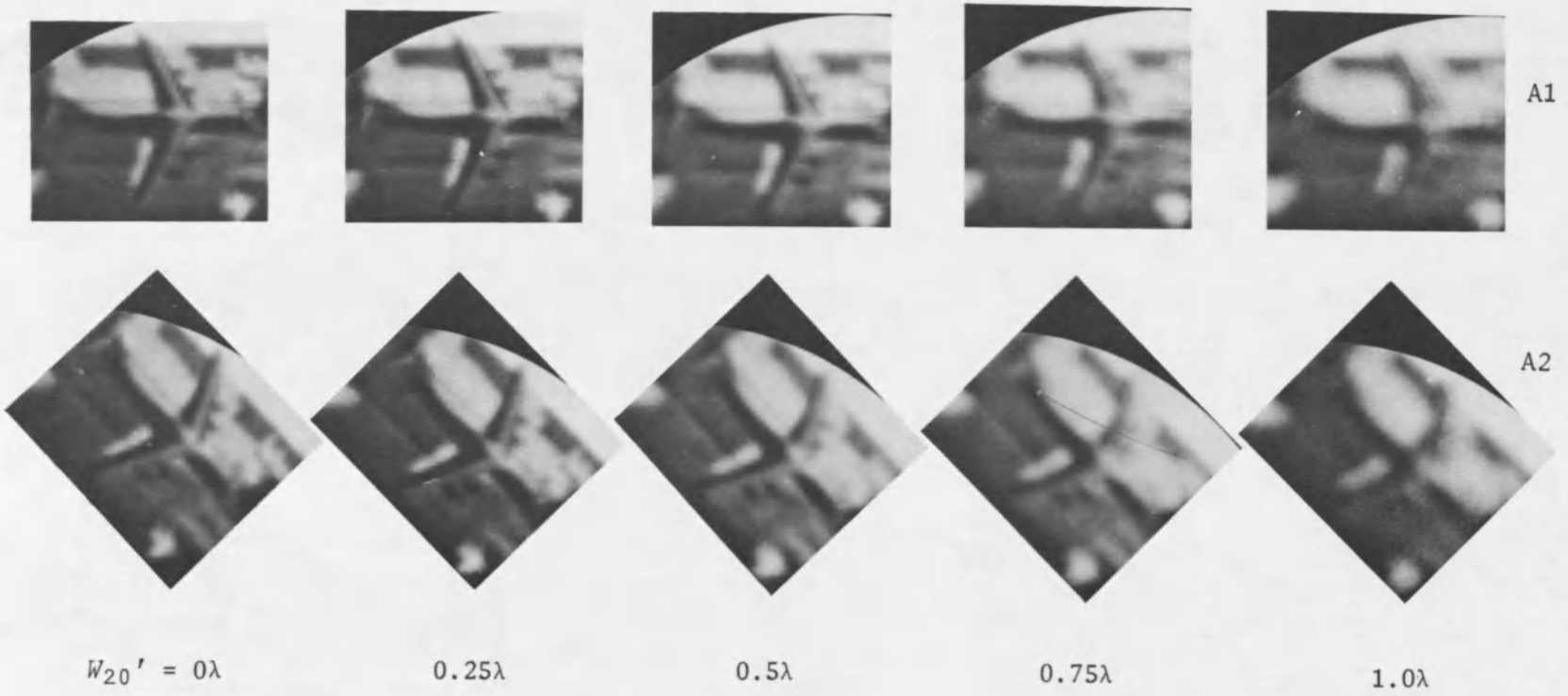

Fig. 56. Target Section A for System Defocus.

midfrequencies (0.25 to 0.4) are visible in the $\phi = 45°$ log-periodic target. The $\phi = 0°$ log-periodic target shows increased double imaging in the low-frequency region as the system defocus is increased. When there is 1.0λ of defocus, the double imaging is very significant and can be seen easily on the upper edge of the large building (section B1) and the leading edge of the large aircraft wing (section A1).

Piston Error

The introduction of piston error into one element of a synthetic aperture system drastically influences the point spread function. Although the effect on the PSF for 0.1λ of piston error is not noticeable (Fig. 57), 0.25λ of piston error makes the pattern very asymmetric. The central core is egg-shaped with its narrow end pointing along the $+y$ axis, and the surrounding plateau region has a threefold symmetry. As the piston error increases from 0.25λ to 0.5λ, the pattern loses its threefold symmetry and appears to acquire a rectilinear nature. The pattern for 0.75λ of piston error is identical to that of the 0.25λ case except that it is rotated by 180°. When the piston error is 1.0λ the PSF returns to its unaberrated form.

The sequence of photographs in Fig. 57 illustrates a unique property of piston error. As the magnitude of this aberration increases, the PSF and transfer function vary in a cyclical fashion. The maximum effect of piston error is observed when its magnitude is an odd multiple of 0.5λ. When the piston error is an even multiple of 0.5λ it has no effect on the PSF. No other aberration behaves in this manner.

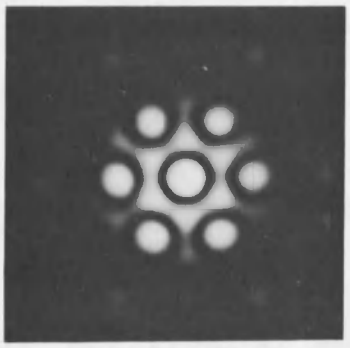

W_{00} = 0 and 1.0λ

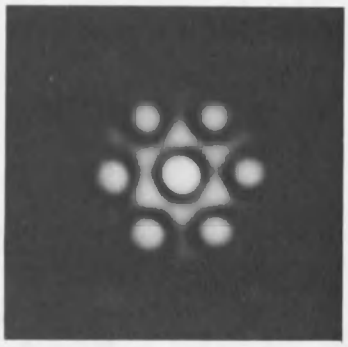

0.1λ

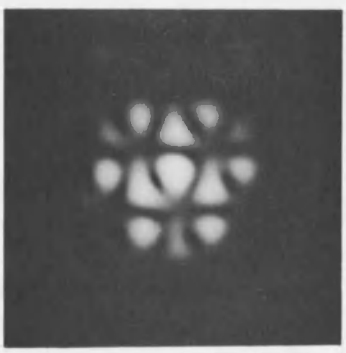

0.25λ

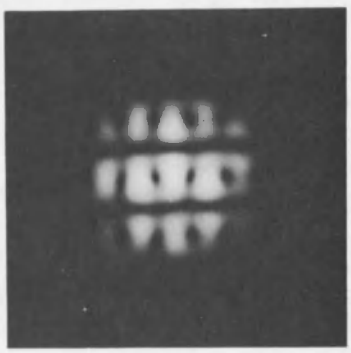

0.5λ

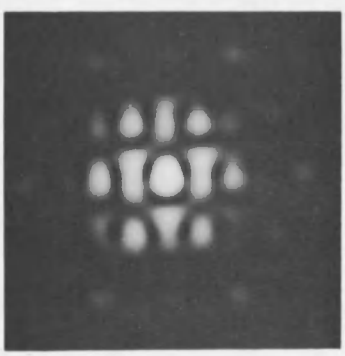

0.75λ

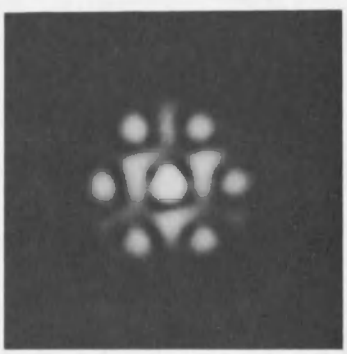

0.5λ
W_{20} = -2λ/3

Fig. 57. PSF for Piston Error.

Figures 58 through 61 show the effect of piston error on the transfer function and the extended target images. For the $\phi = 0°$ transfer function, only the aberrated element and one unaberrated element contribute to the spatial frequency region between 0.64 and 1.0 (see Fig. 15). In this region the MTF is unaffected, and the value of the PTF in cycles equals the magnitude of the piston error in waves. The $\phi = 0°$ log-periodic target in Fig. 59 shows that the high-frequency bars in the vicinity of $\nu = 0.75$ are visible even when 0.5λ of piston error is present. More than two pairs of elements contribute to the $\phi = 0°$ transfer function in the spatial frequency region from 0.5 to 0.64. Therefore, the modulus as well as the phase is affected.

Whereas piston error affects the PTF more than the MTF for the $\phi = 0°$ orientation, the MTF is more affected for the $\phi = 45°$ orientation. Figure 58 shows that, for 0.5λ of piston error, the MTF is zero for spatial frequency components greater than 0.25. The $\phi = 45°$ log-periodic target (Fig. 59) illustrates this reduction in the modulus of the transfer function.

Several features in the target section images (Figs. 60 and 61) are changed when piston error is introduced. As the piston error increases to 0.5λ, the distinction between the two railroad tracks in target B1 and between the stripes on the railroad car in B2 decreases. At $W_{00} = 0.5\lambda$ they are unresolved. Similarly, the leading edge of the left aircraft wing in target A1 (Fig. 61) becomes less distinct as the piston error increases to 0.5λ. The image quality improves as the piston error increases from 0.5λ to 1.0λ.

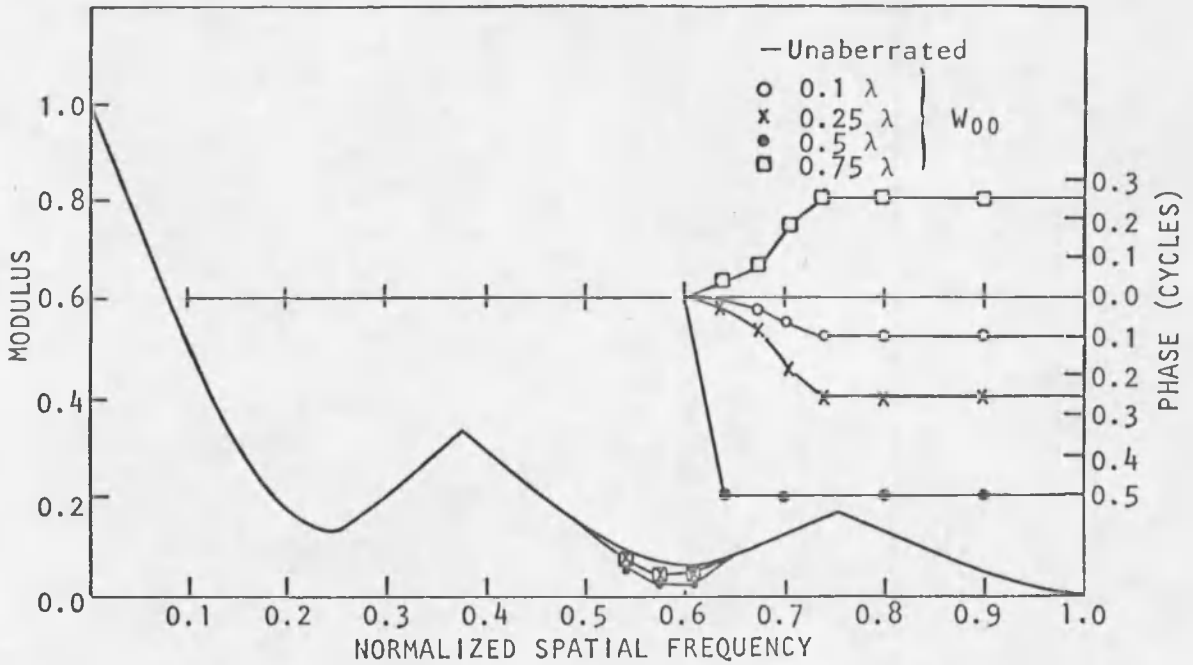

a $\phi = 0°$

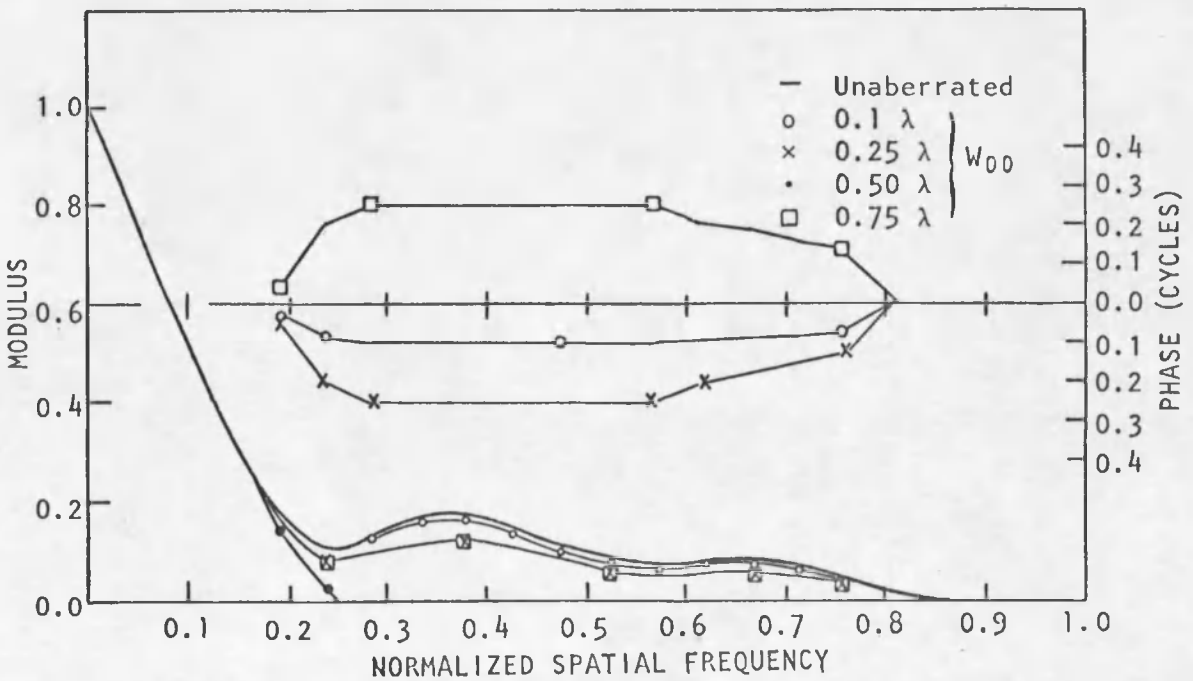

b $\phi = 45°$

Fig. 58. Transfer Function for Piston Error.

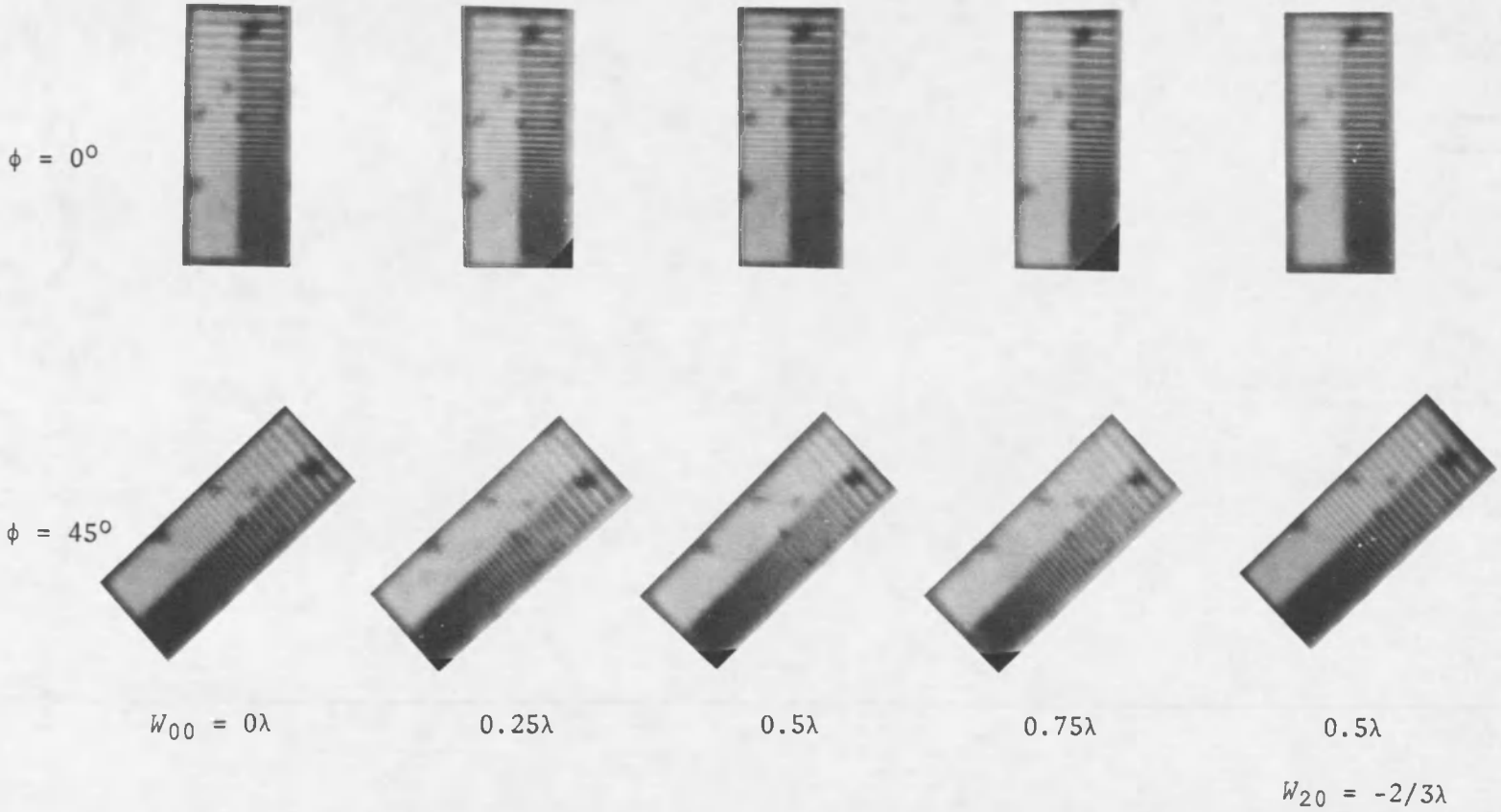

Fig. 59. Log-Periodic Target for Piston Error.

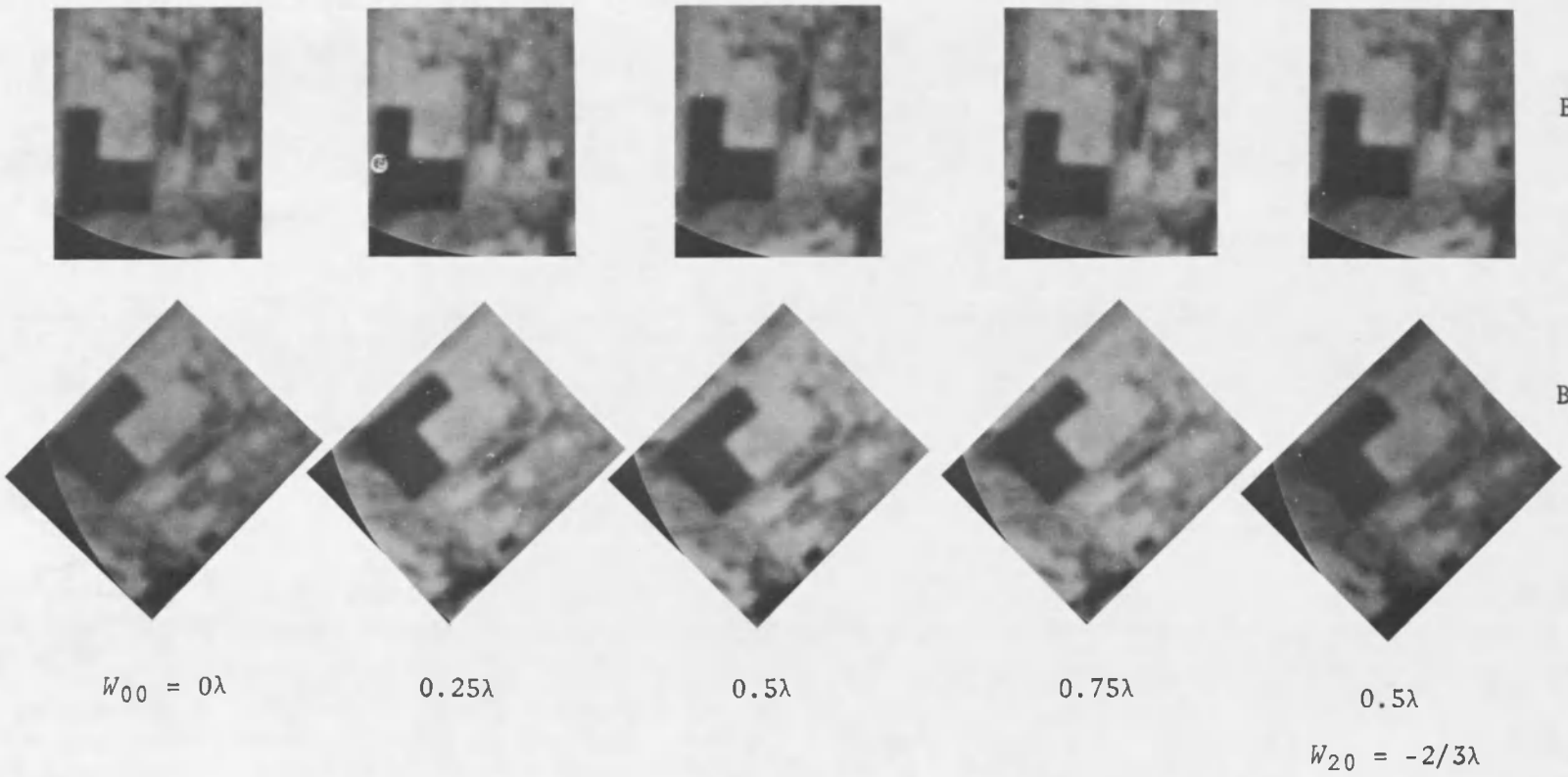

Fig. 60. Target Section B for Piston Error

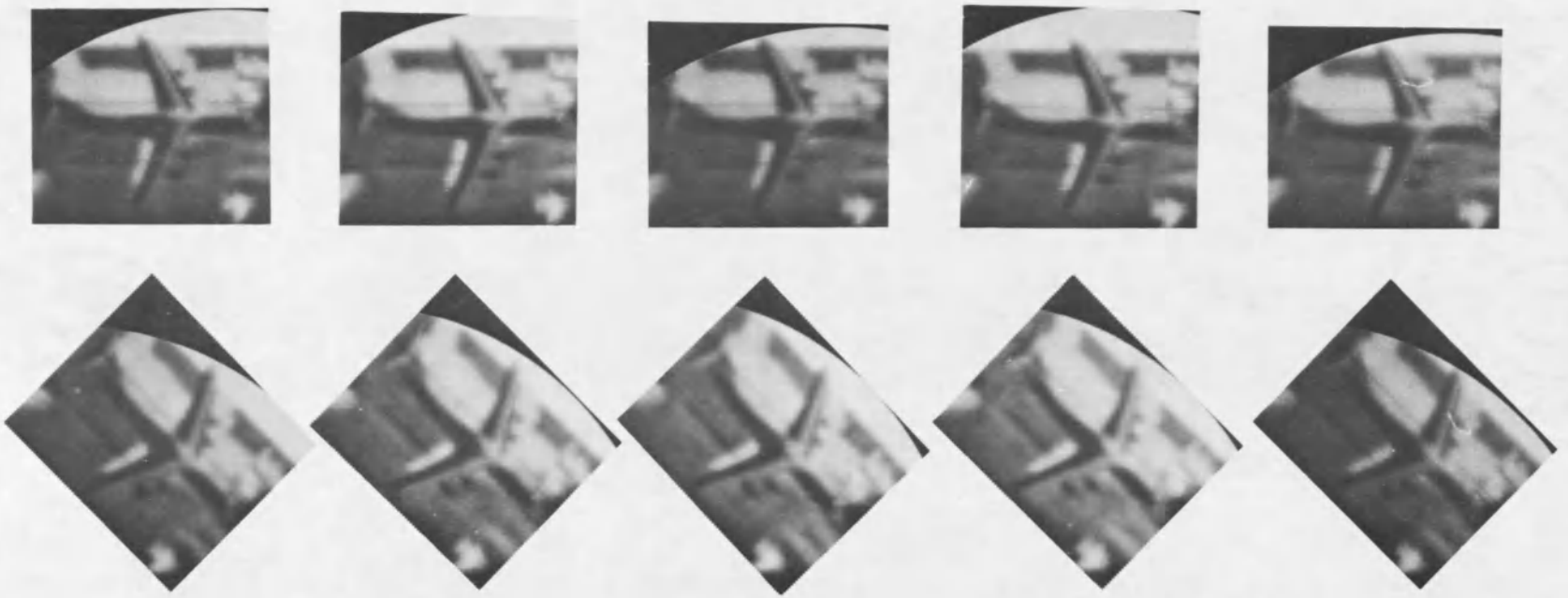

Fig. 61. Target Section A for Piston Error.

Balancing Piston Errors with Defocus. The effects of 0.5λ of piston error are very noticeable, particularly on the $\phi = 45°$ transfer function. By introducing a compensating amount of defocus into the aberrated element, the $\phi = 45°$ MTF can be improved significantly. Figure 62 shows the transfer function when 0.5λ of piston error is balanced with -0.66λ of defocus. The $\phi = 45°$ MTF has been improved by as much as 0.1, and the PTF shows very little phase error. The $\phi = 0°$ PTF is substantially improved, but the $\phi = 0°$ MTF has decreased significantly, particularly in the high-frequency region.

The effect of the balancing aberration on the point spread function and the target photographs is equally apparent. Figure 57 shows that the point spread function has a better defined central core and has regained its hexagonal symmetry to some extent. The higher frequency bars on the $\phi = 45°$ log-periodic target (see Fig. 59) are resolved as a result of adding the balancing aberration. However, as would be expected from Fig. 62, the high-frequency bars ($\nu > 0.6$) on the $\phi = 0°$ log-periodic target are not resolved. Target features that are unresolved as a result of the 0.5λ of piston error (railroad track, leading edge of aircraft wing, and stripes on boxcar; see Figs. 60 and 61) can be resolved when the compensating defocus is added.

Interaction Between Piston Error and System Focus. When 0.5λ of piston error is introduced into one element, the $\phi = 45°$ MTF goes to zero for spatial frequencies greater than 0.25. However, if system defocus is also introduced, the MTF can be raised significantly.

Figure 63a shows that the $\phi = 45°$ MTF for 0.5λ of piston error is as much as 0.06 higher when 0.25λ of system defocus is added. The

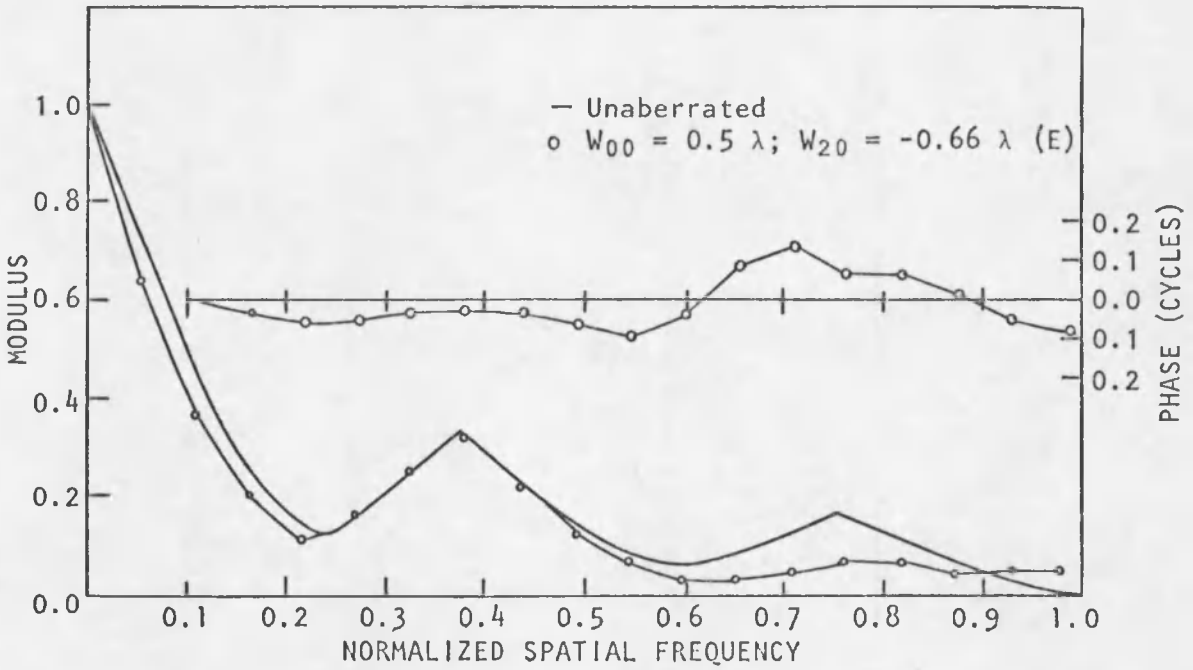

a $\phi = 0°$

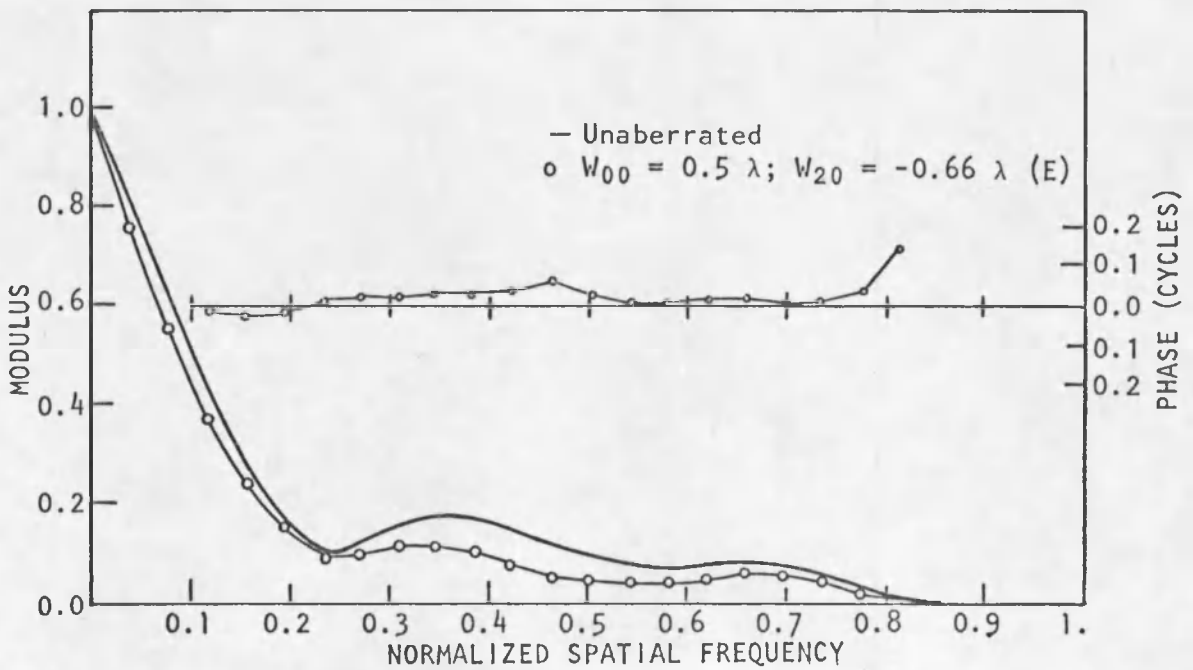

b $\phi = 45°$

Fig. 62. Transfer Function for Piston Error Balanced with Defocus.

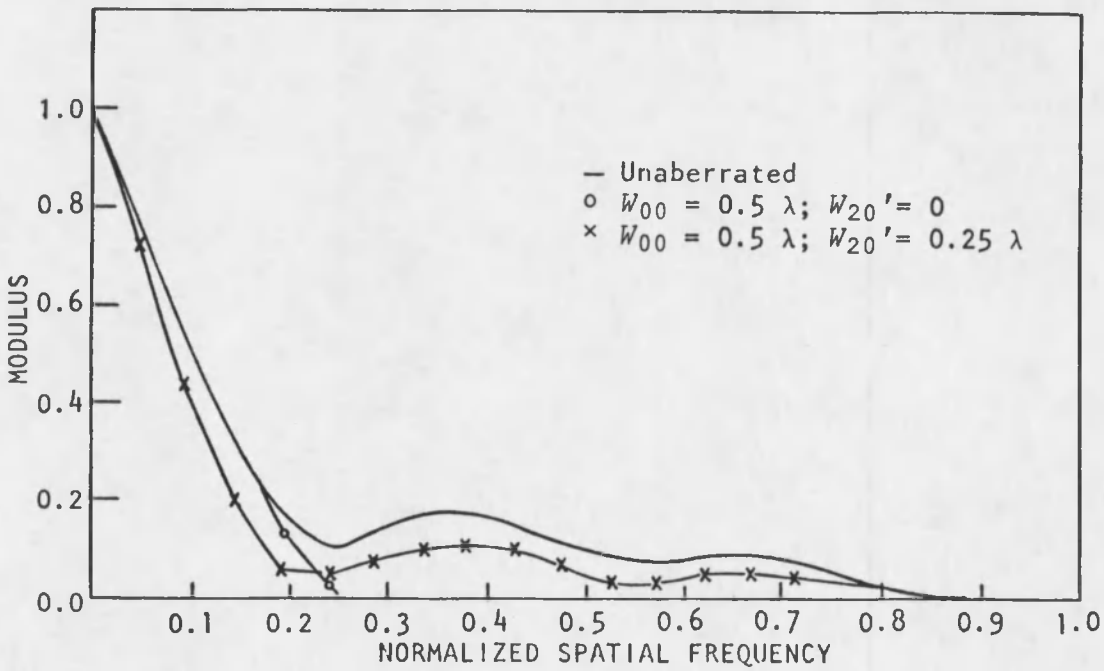

a. $\phi = 45^{\circ}$ MTF.

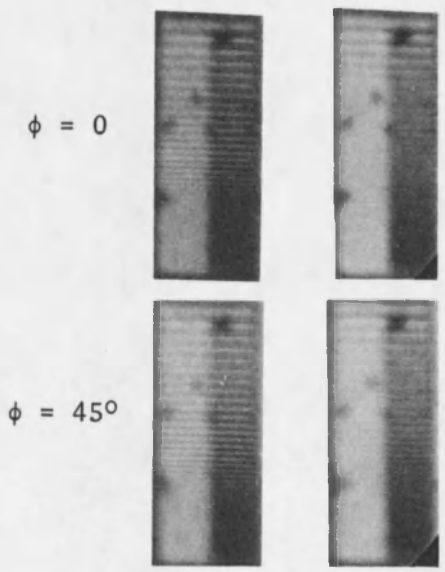

b. Log-Periodic Target.

Fig. 63. MTF and Log-Periodic Target for Piston Error Balanced with System Defocus.

improvement in MTF is evident in the $\phi = 45°$ log-periodic target in Fig. 63b. There is no significant decrease in the $\phi = 0°$ transfer function as indicated by the $\phi = 0°$ log-periodic target.

Unfortunately, neither the MTF for images of the log-periodic target completely describe the imaging characteristics of the synthetic aperture system. While the MTF improves when system defocus is introduced, PTF develops severe fluctuations (Fig. 64a). As a result, the target sections show a degradation rather than an improvement as system defocus is introduced (Fig. 64b).

Wavefront Tilt

The effect of wavefront tilt is to shift the point spread function of the aberrated pupil element away from the spread functions of the unaberrated elements. In Fig. 65 the point spread function is shown for various magnitudes of tilt and for two different orientations. The shifted spread function is clearly visible in the $W_{11} = 0.75\lambda$ photographs. The effect of $\alpha = 0°$ tilt is to make the central core of the PSF elliptically shaped, while $\alpha = 90°$ tilt makes the core egg-shaped. For small amounts of tilt (less than 0.5λ) the intensity distribution of the surrounding plateau shifts in the direction of the aberrated element's spread function. For $\alpha = 0°$ the pattern is symmetrical about the y axis and for $\alpha = 90°$ the pattern is symmetrical about the x axis. When the tilt is 0.75λ the light from the aberrated element is not contributing significantly to the center of the pattern and the central core and surrounding plateau have the same basic appearance for both $\alpha = 0°$ and $\alpha = 90°$.

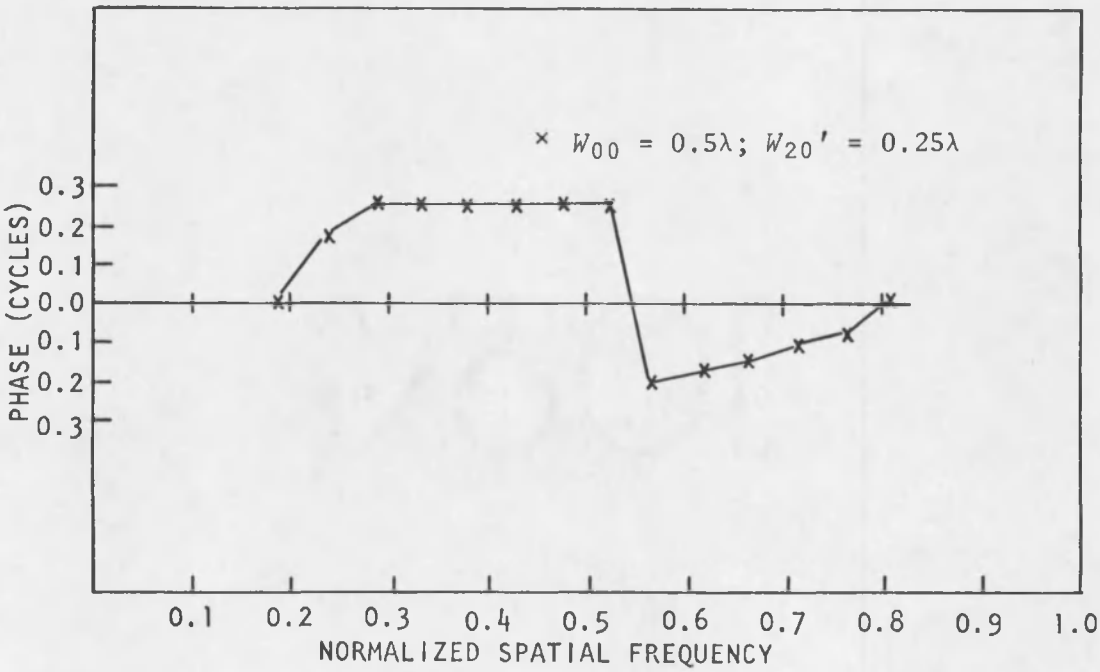

a. $\phi = 45^{\circ}$ PTF.

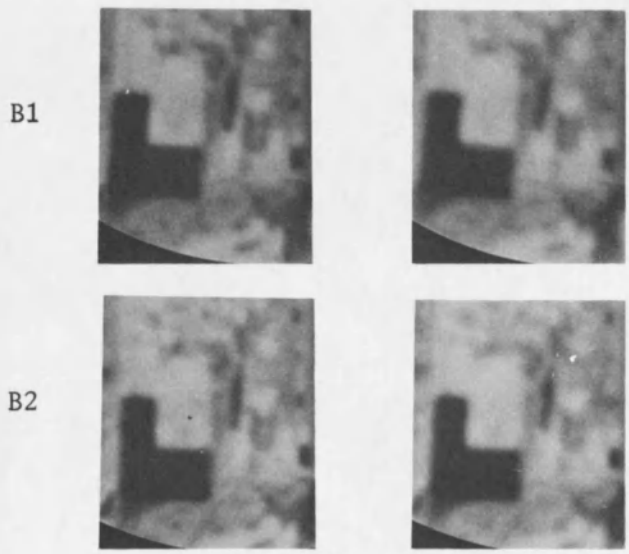

W_{00} = 0.5λ	0.5λ
W_{20}' = 0λ	0.25λ

b. Target Section B.

Fig. 64. PTF and Target Section B for Piston Error Balanced with System Defocus.

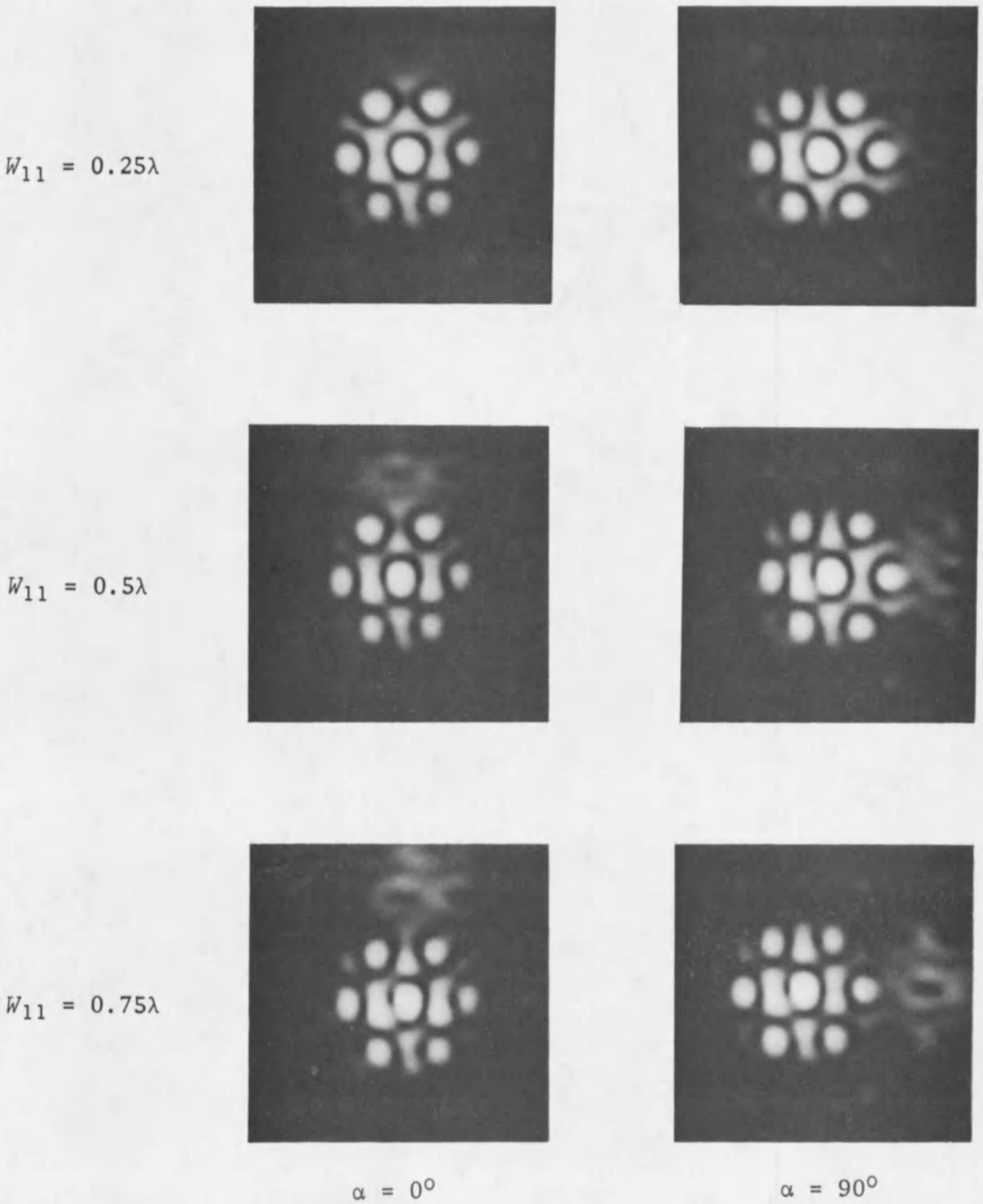

Fig. 65. PSF for Tilt.

The transfer function cross sections are shown in Figs. 66 and 67, and the target section photographs are shown in Figs. 68 through 71.

The $\phi = 0°$ transfer function behaves basically the same at high spatial frequencies for $\alpha = 0°$ and $\alpha = 90°$. With 0.5λ of tilt, the modulus is at a barely detectable level and a moderate phase error exists. The modulus is effectively zero for spatial frequencies greater than 0.6 when the tilt equals 0.75λ. The low-frequency response, however, is different for the two orientations of tilt. When $\alpha = 90°$ the low spatial frequency components are not affected, but when $\alpha = 0°$ these components show a significant decrease in modulus. These characteristics are visible in the log-periodic targets of Figs. 68 and 69.

Tilt affects the $\phi = 45°$ transfer function across the entire spatial frequency region. The decrease in the MTF is slightly greater for the $\alpha = 0°$ than for the $\alpha = 90°$ tilt orientation.

An interesting characteristic of the transfer function for the $\alpha = 0°$ tilt orientation is the increase of the MTF in the spatial frequency region from 0.12 to 0.22 when the tilt increases from 0.5λ to 0.75λ. This increase is only about 0.04 but can be detected by comparing the $\phi = 45°$ log-periodic targets in Fig. 68. The very low frequency portion of the target shows significant double imaging (and hence low contrast) when the tilt is 0.5λ and only slight double imaging when the tilt is 0.75λ.

The effect of 0.25λ of tilt on the target sections is not significant. However, when the tilt is 0.5λ there are noticeable changes. The stripes on the boxcar (target section B2 in Fig. 70) are well resolved for a tilt of 0.25λ, barely resolved for 0.50λ, and unresolved

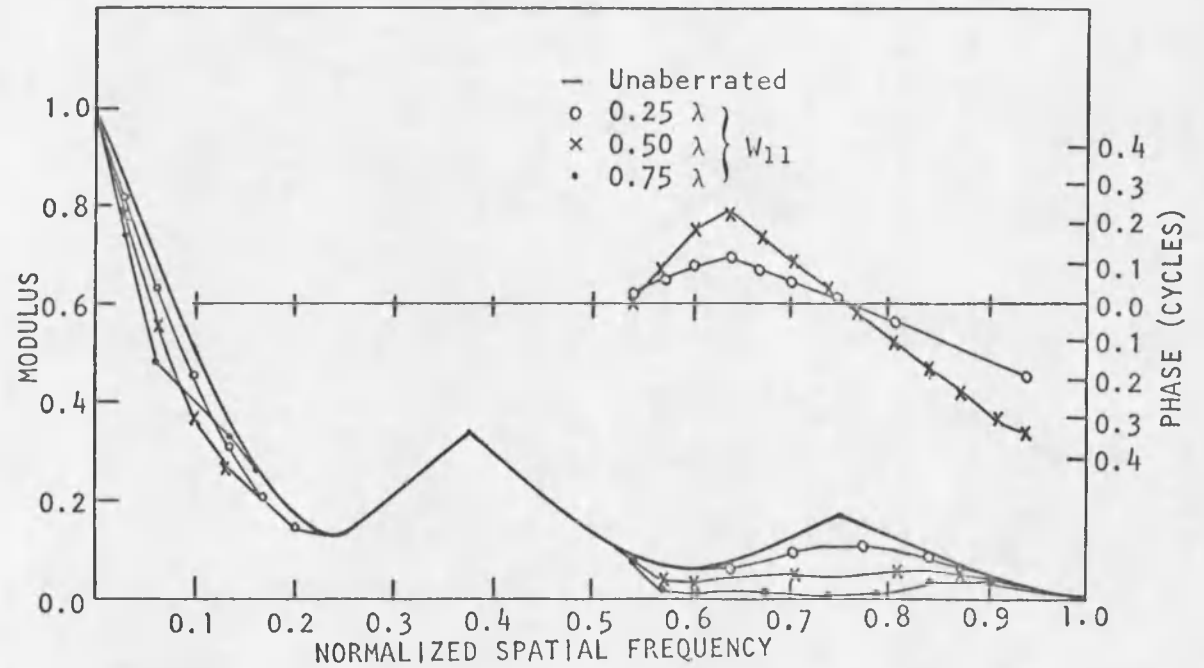

a $\phi = 0°$

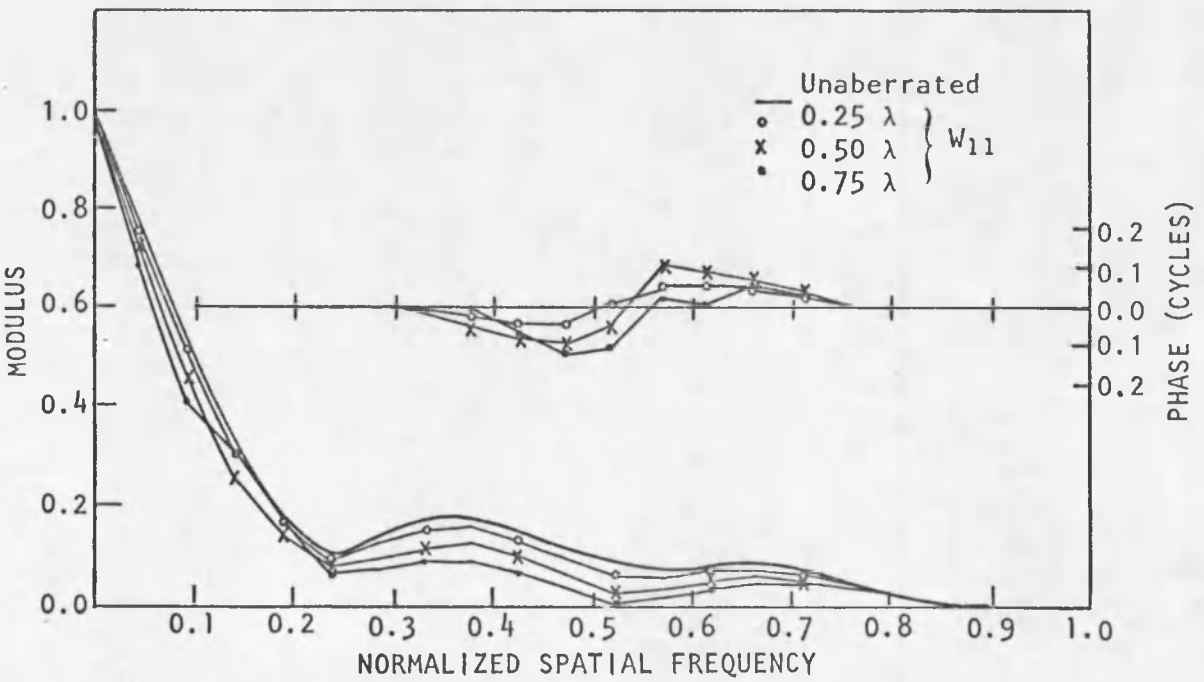

b $\phi = 45°$

Fig. 66. Transfer Function for Tilt ($\alpha = 0°$).

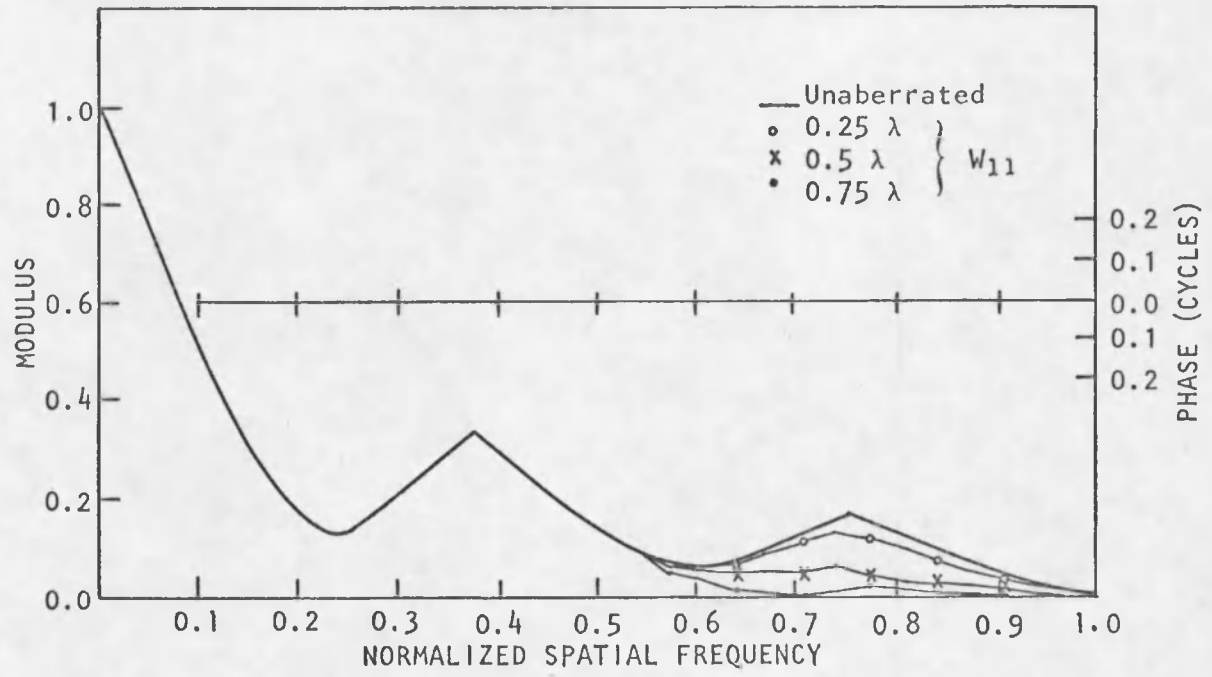

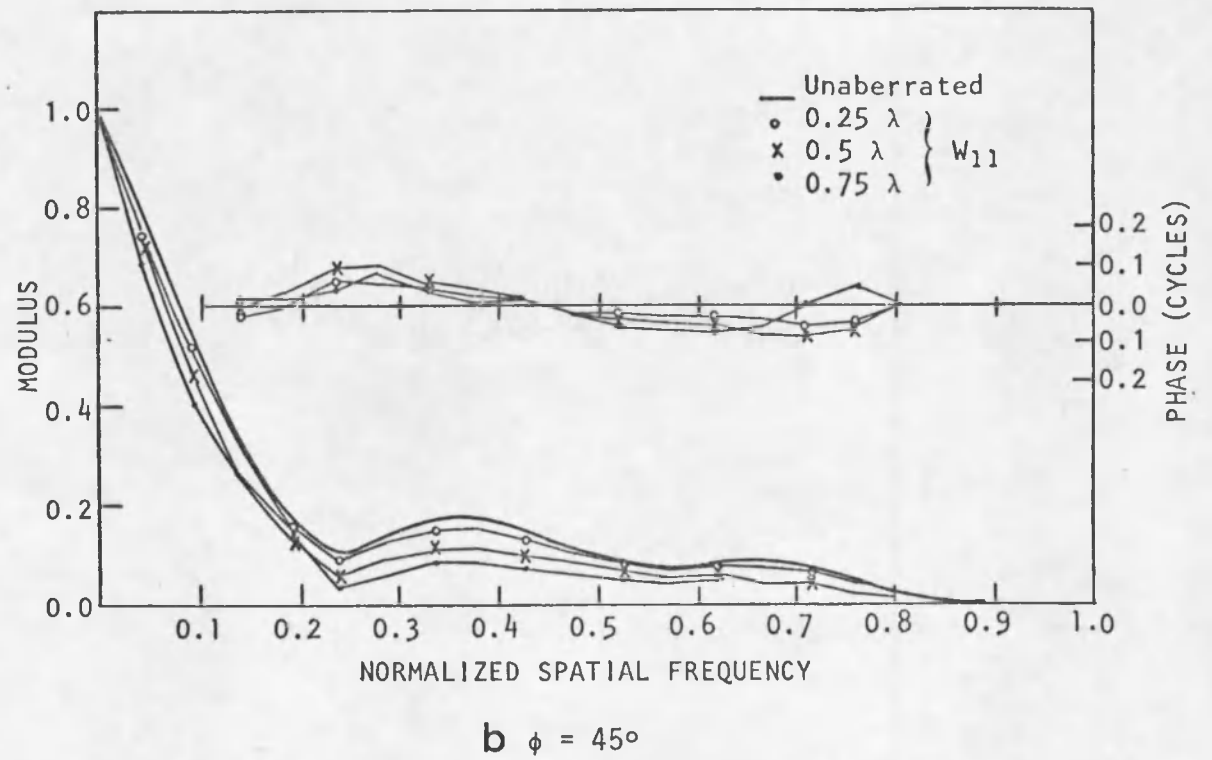

Fig. 67. Transfer Function for Tilt (α = 90°).

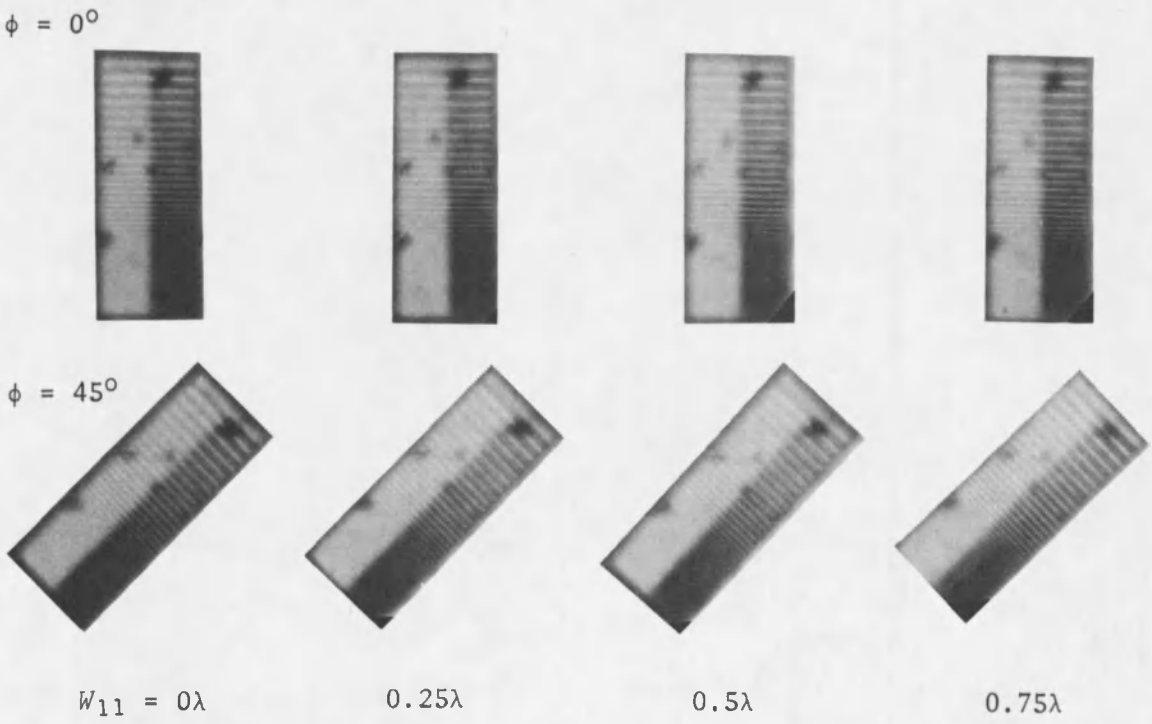

Fig. 68. Log-Periodic Target for Tilt ($\alpha = 0°$).

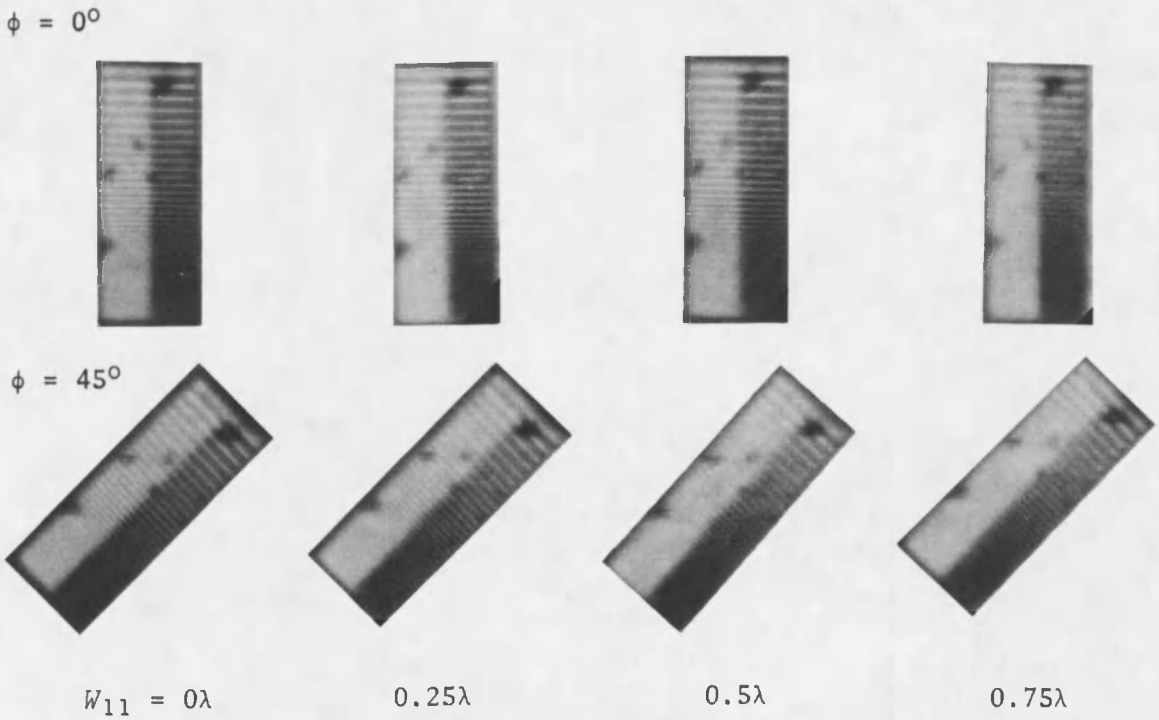

Fig. 69. Log-Periodic Target for Tilt ($\alpha = 90^{o}$).

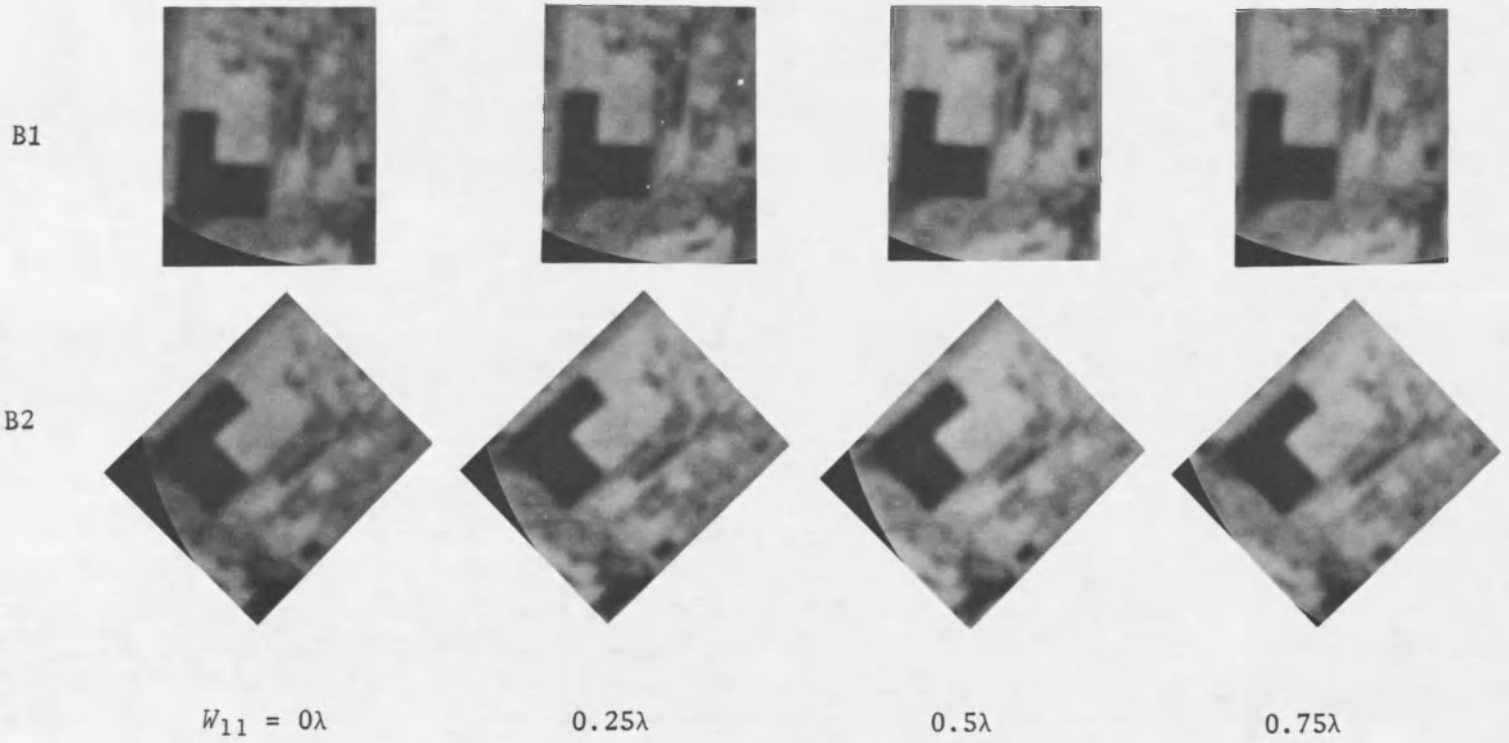

Fig. 70. Target Section B for Tilt ($\alpha = 0^{o}$).

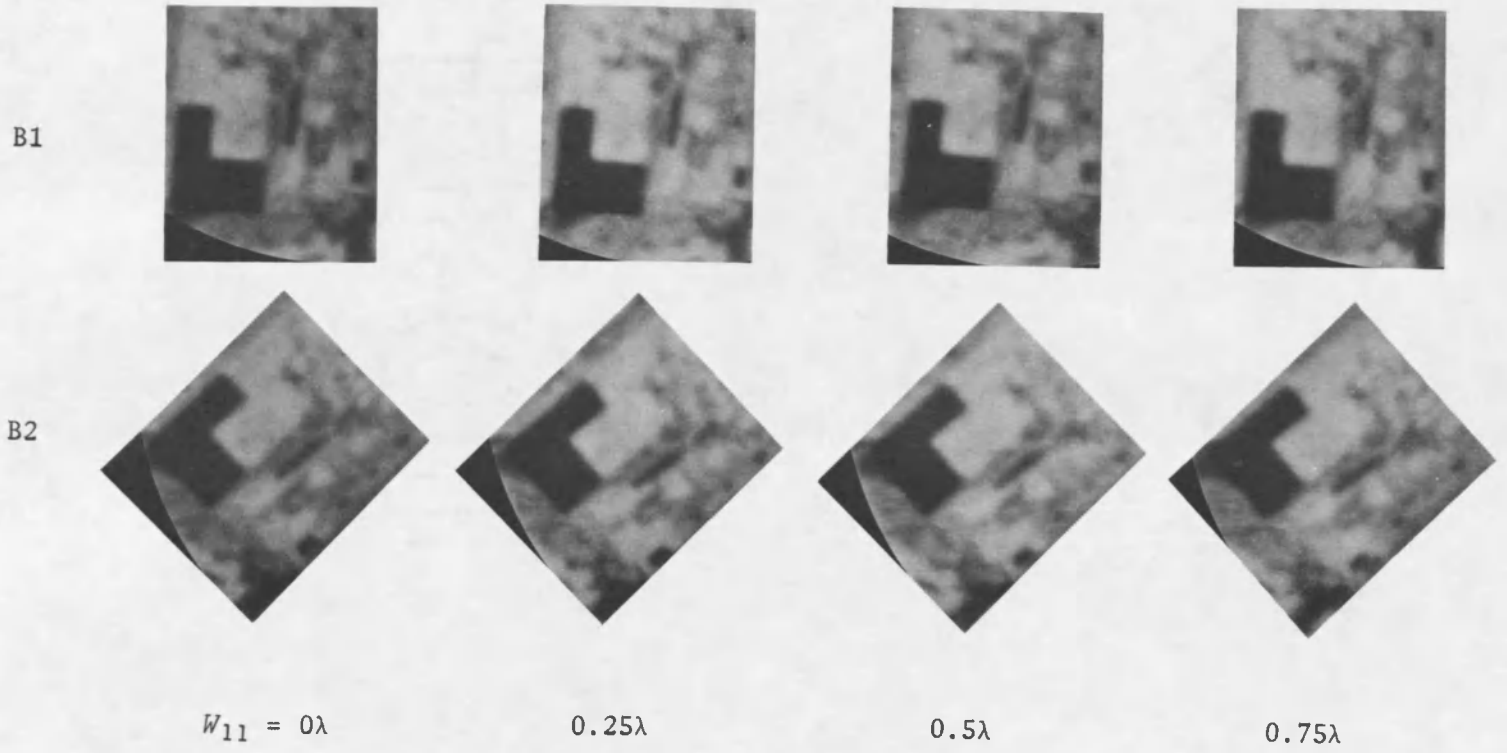

Fig. 71. Target Section B for Tilt ($\alpha = 90^{o}$).

for 0.75λ. Similar degradation occurs with the railroad tracks (target section B1 in Fig. 70) although the tracks are still resolved when the tilt equals 0.75λ. For $\alpha = 0^\circ$ tilt of 0.5λ, a third railroad track appears in the B1 target section. This artifact is caused by strong double imaging, as evidenced by the $\phi = 45^\circ$ log-periodic target in Fig. 68.

Defocus

The effect of single-element defocus on the point spread function is illustrated in Fig. 72. With as little as 0.25λ of defocus, a change in the central core and surrounding plateau can be detected. The core exhibits a threefold symmetry and has a slightly triangular shape. Similarly, the intensity distribution across the plateau region has a threefold symmetry whereas in the unaberrated case it has a sixfold symmetry (note in Fig. 72 the bright plateau regions at the 2, 6, and 10 o'clock positions).

When 0.5λ of defocus is present, the point spread function is more complicated but still shows signs of a threefold symmetry. Whereas for 0.25λ of defocus the changes in the spread function were subtle, when the defocus reaches 0.5λ the changes are very apparent. When the defocus is 0.75λ the central core has greatly elongated and the plateau region has broken into separate patches. Defocusing from 0.75λ to 1.0λ changes the egg-shaped central core into an oval but does not change the spread function, as little of the light from the aberrated pupil is concentrated near the central core.

The transfer function behavior (Fig. 73) is consistent with the observed changes in the spread function. For 0.25λ of defocus there is

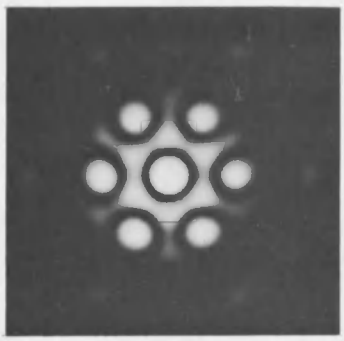

W_{20} = 0λ

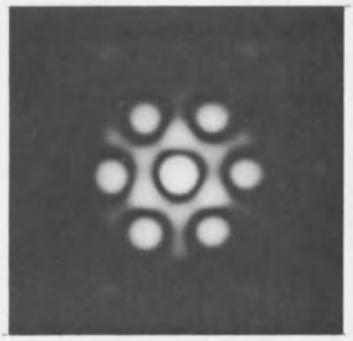

0.25λ

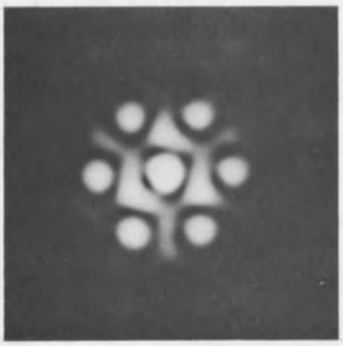

0.5λ

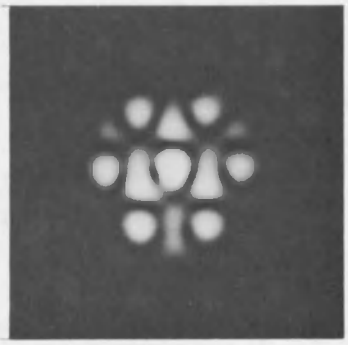

0.75λ

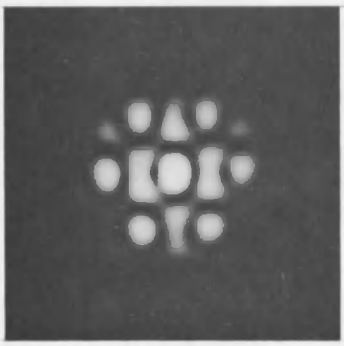

1.0λ

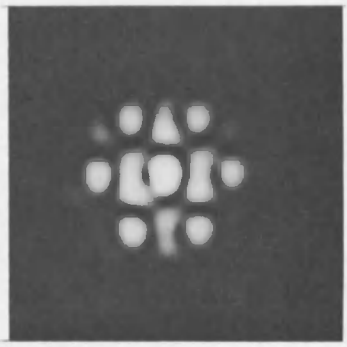

1.5λ

Fig. 72. PSF for Defocus.

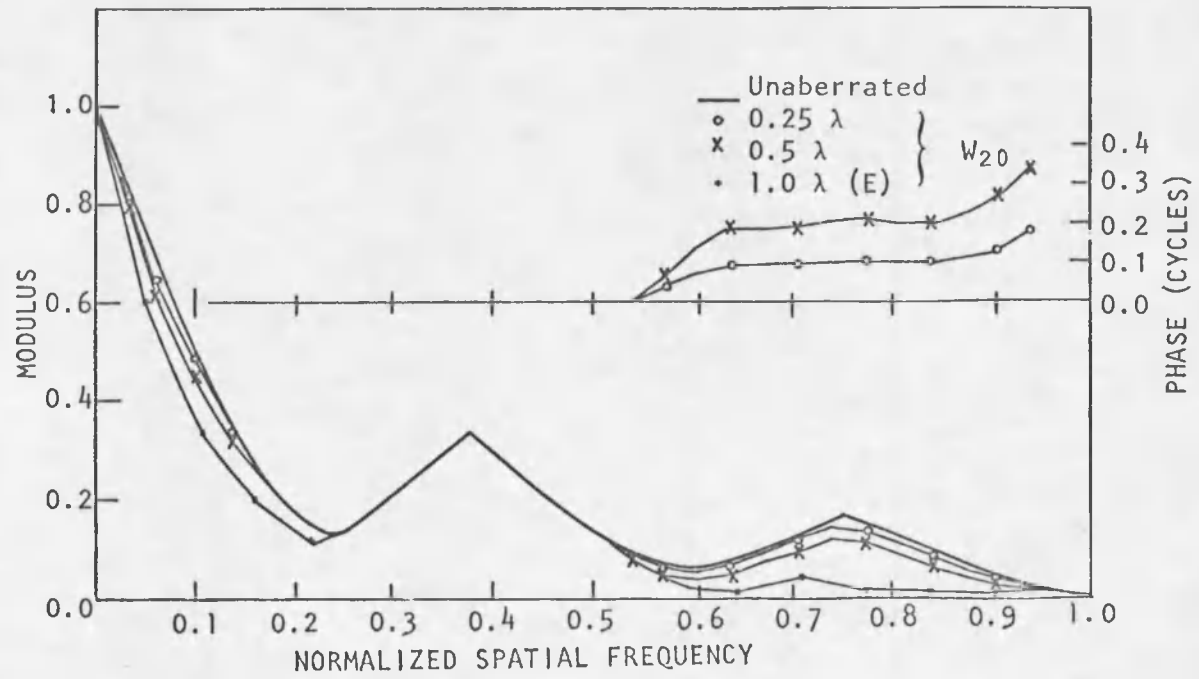

a $\phi = 0°$

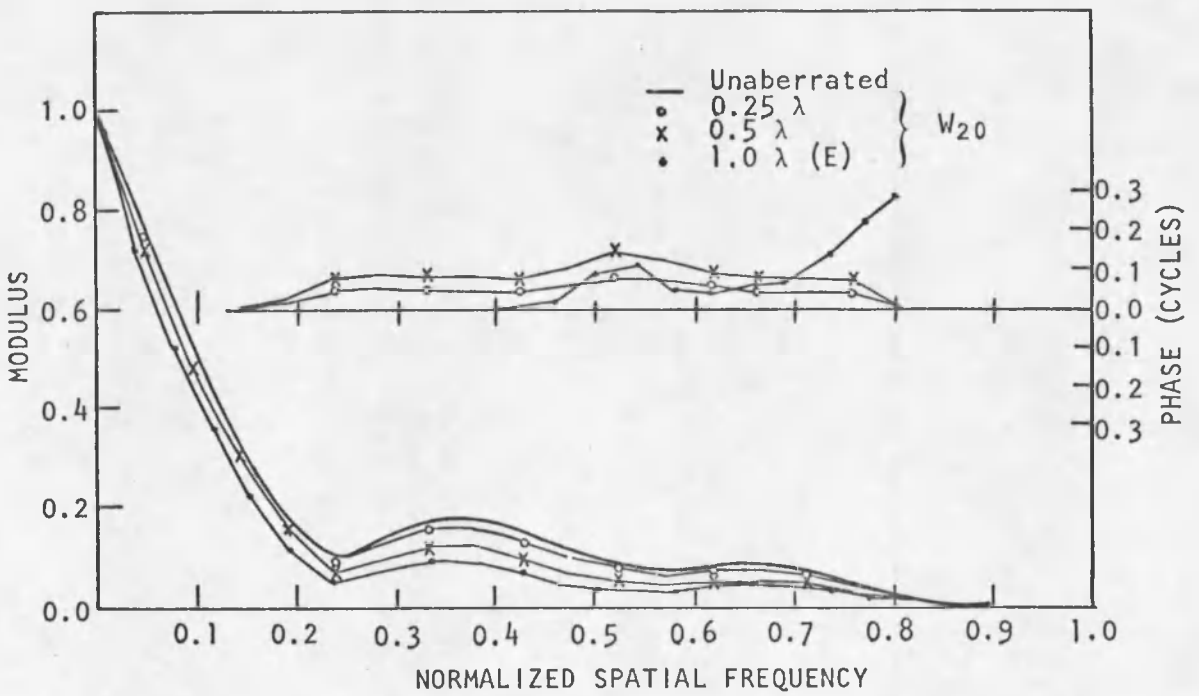

b $\phi = 45°$

Fig. 73. Transfer Function for Defocus.

only a slight decrease in the MTF and a small phase error in the PTF. When the defocus reaches 0.5λ, the MTF has decreased a small amount (about 0.04) in those spatial frequency regions where the aberrated element contributes to the transfer function. The PTF is small in the ϕ = 45° direction but nearly 25% of a cycle in the ϕ = 0° direction (for frequencies greater than 0.6).

The transfer function for 1.0λ of defocus is substantially less than for 0.5λ of defocus. In the ϕ = 0° direction, the low-frequency components are reduced in modulus by as much as 0.12 and the high-frequency components (greater than 0.6) have a modulation that is effectively zero. In the ϕ = 45° direction the low-frequency (less than 0.25) modulation has been reduced by about 0.06 and the middle and high frequency modulation has been reduced by about 50%.

The PTF curves in Fig. 73 indicate the asymmetry of the point spread function. As the defocus increases, the asymmetry and hence the PTF increase. However, as the defocus increases from 0.5λ to 1.0λ, much of the symmetry in the ϕ = 0° and ϕ = 45° directions is regained.

The target photographs in Figs. 74 and 75 show no degradation for 0.25λ of defocus. When the defocus reaches 0.5λ the high-frequency (greater than 0.6) components in the ϕ = 0° log-periodic target are no longer visible and the railroad tracks in target section B1 cannot be resolved. For defocus of 1.0λ the contrast of the ϕ = 0° and ϕ = 45° log-periodic targets is noticeably lower than in the unaberrated case. In addition, the stripes on the railroad car can no longer be resolved in target section B2. Increasing the defocus from 1λ to 2λ does not change the appearance of the log-periodic target (Fig. 74).

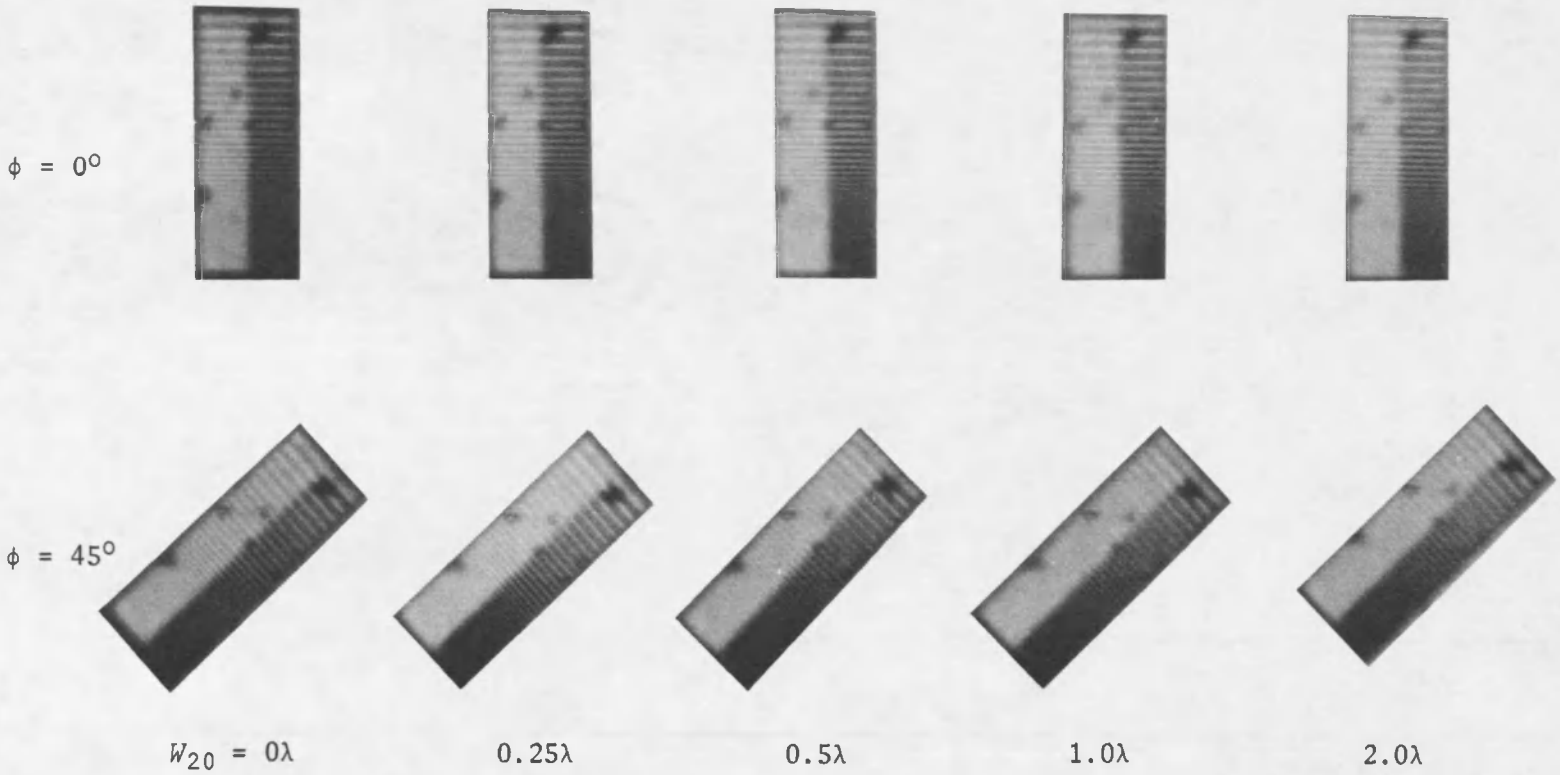

Fig. 74. Log-Periodic Target for Defocus.

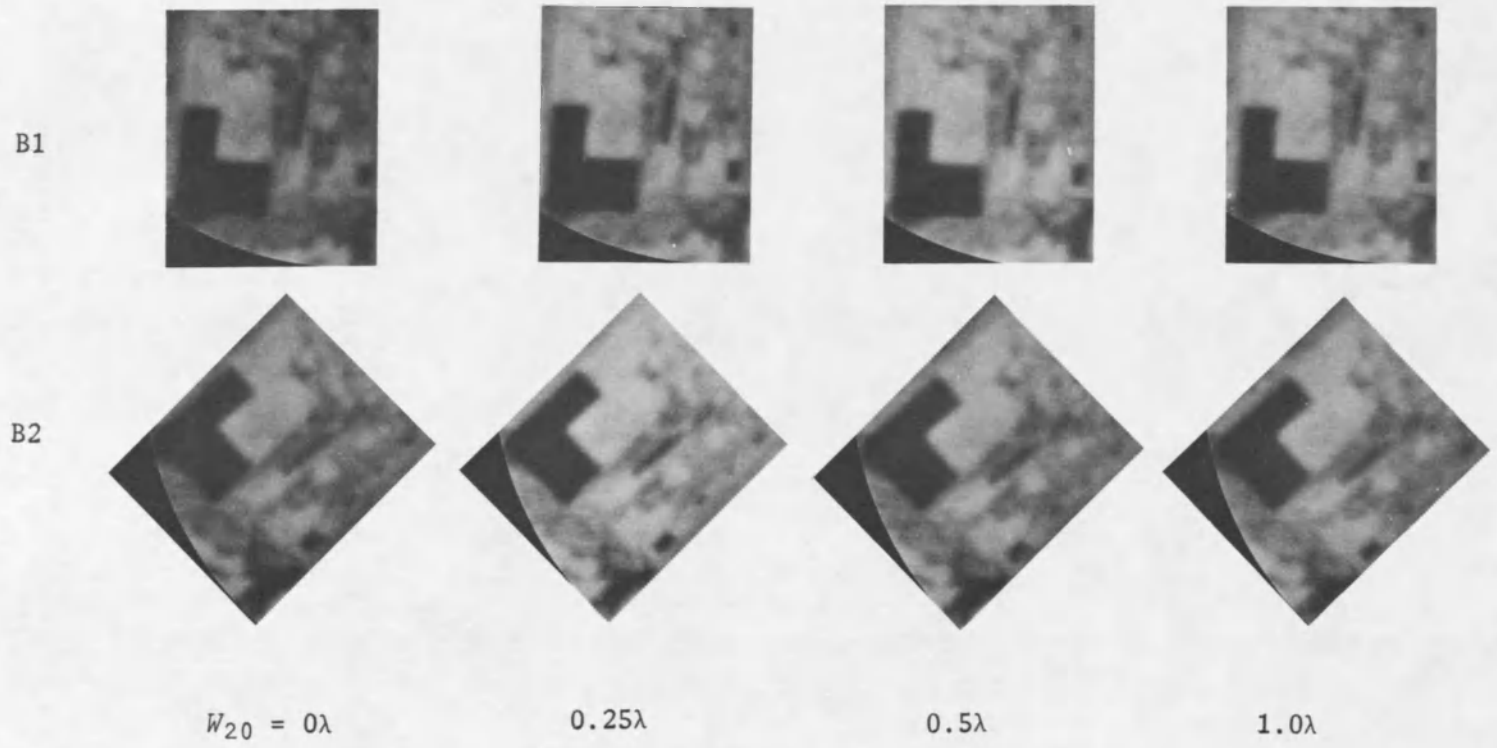

Fig. 75. Target Section B for Defocus.

When 1.0λ of defocus has been introduced, most of the light from the aberrated element is distributed away from the central core of the synthetic aperture point spread function. As a result, the aberrated six-element aperture is behaving like the unaberrated five-element aperture discussed in Chapter II. The modulation transfer function of the five-element synthetic aperture (Fig. 16) is very similar to the transfer function of the highly aberrated six-element aperture (Fig. 73).

Spherical Aberration

The effects of spherical aberration on the synthetic aperture images are very small. Figure 76 shows that the central core of the point spread function elongates slightly when 1.0λ of spherical aberration is introduced. However, the spread function is not nearly as distorted as when there is 1.0λ of defocus (see Fig. 72). With 1.0λ of spherical aberration there is a significant reduction in the $\phi = 0°$ MTF (Fig. 77) and a significant phase error for spatial frequency components greater than 0.6. Bars in that frequency range on the log-periodic target (Fig. 78) cannot be resolved.

The $\phi = 45°$ MTF is slightly reduced by 1.0λ of spherical aberration although the phase error is negligible. The effect on the log-periodic target is visible as a slight reduction in contrast.

When the spherical aberration is balanced by an equal amount of defocus (of the opposite sign), the image quality improves markedly. With the balancing defocus the core of the point spread function is more compact and has a slightly triangular rather than an oval shape. The

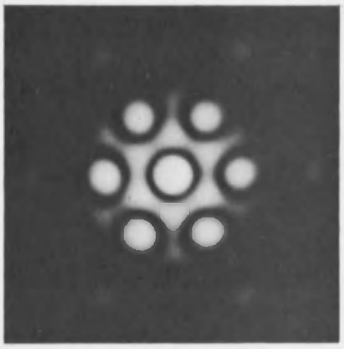

$W_{40} = 0\lambda$

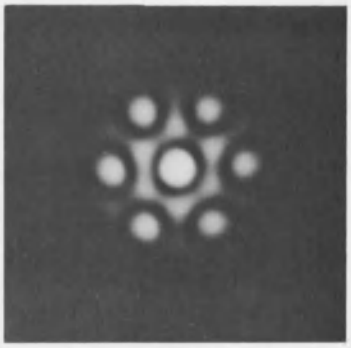

$W_{40} = 0.25\lambda$

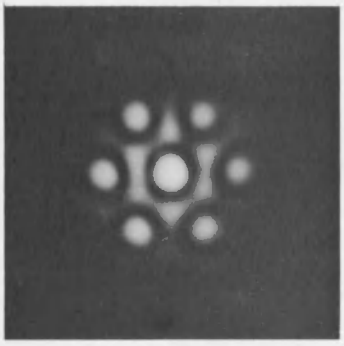

$W_{40} = 0.5\lambda$

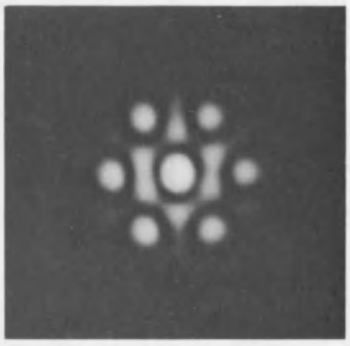

$W_{40} = 1.0\lambda$

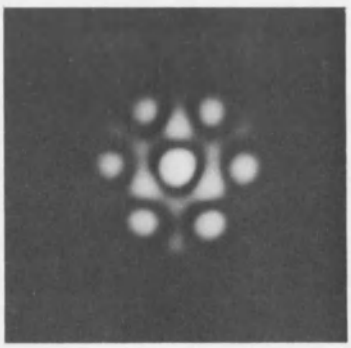

$W_{40} = 1.0\lambda$
$W_{20} = -1.0\lambda$

Fig. 76. PSF for Spherical Aberration.

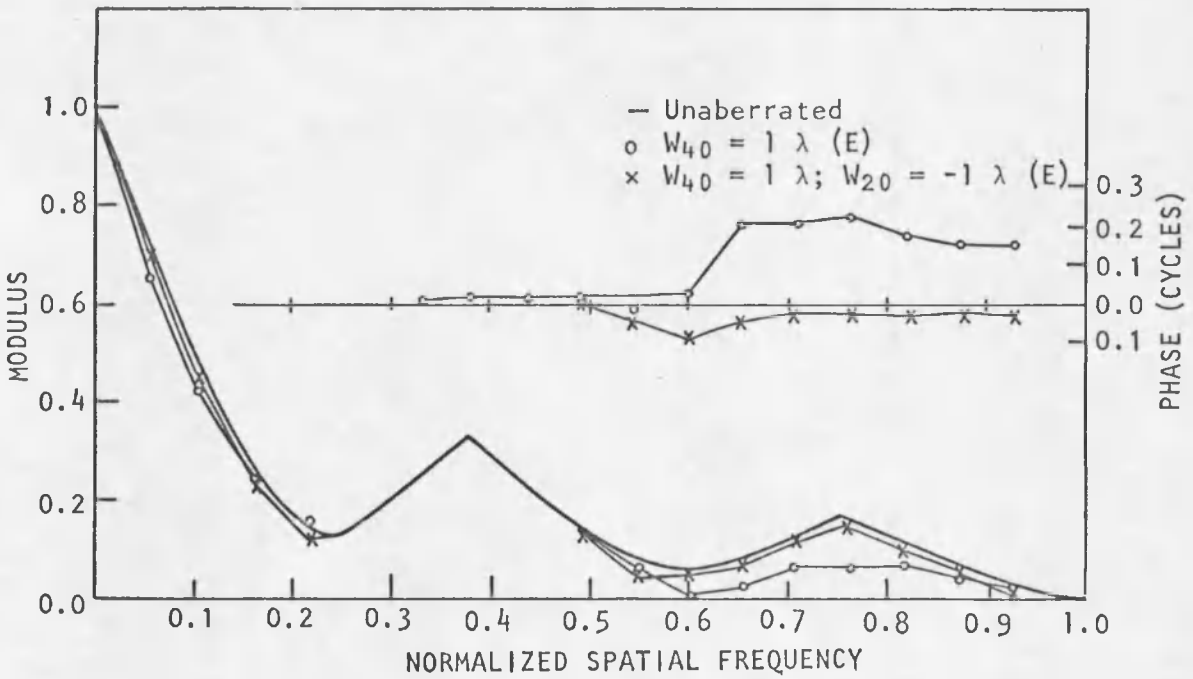

a $\phi = 0°$

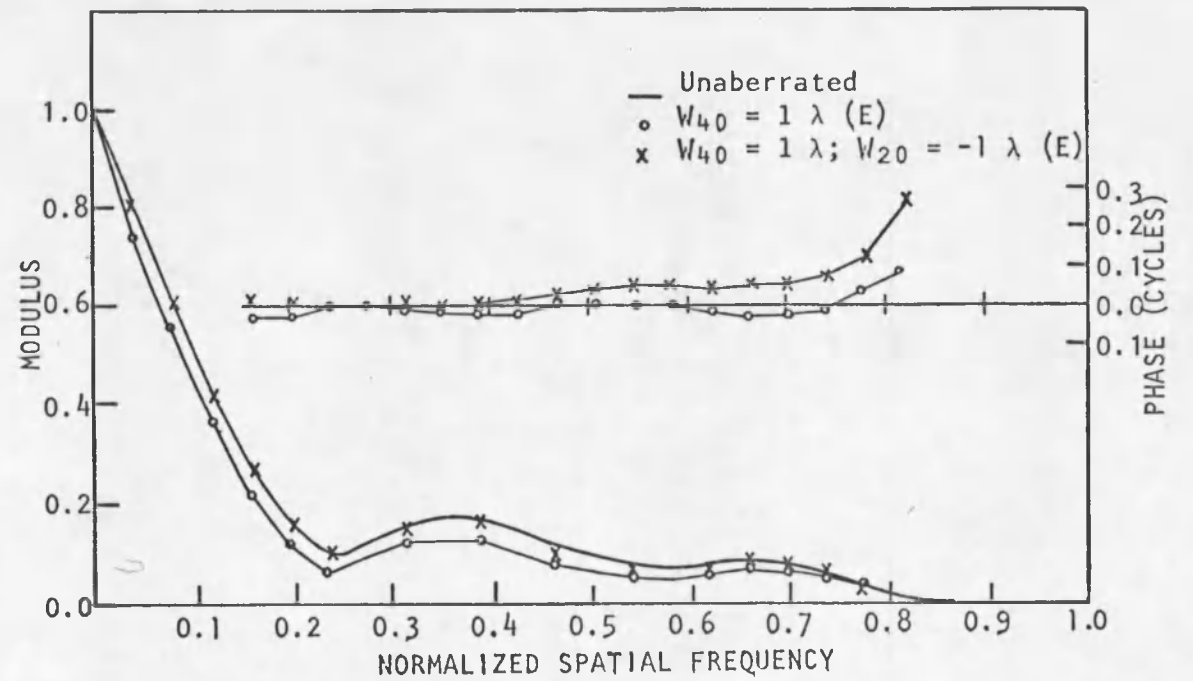

b $\phi = 45°$

Fig. 77. Transfer Function for Spherical Aberration.

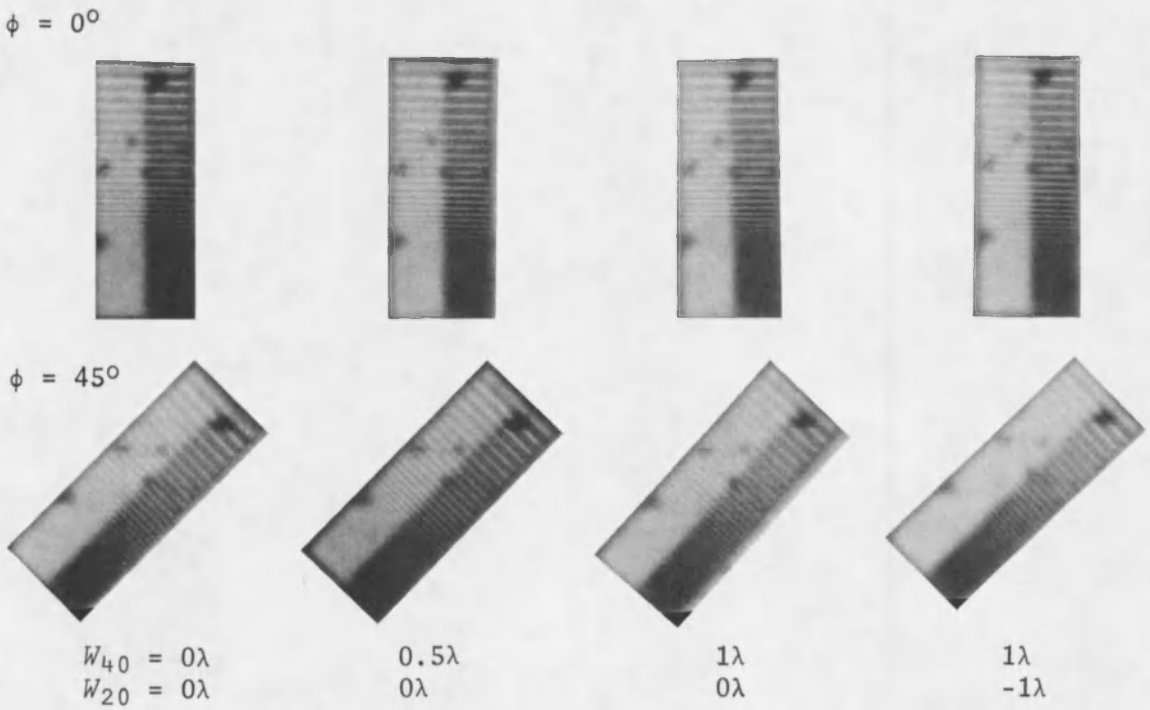

Fig. 78. Log-Periodic Target for Spherical Aberration.

high-frequency region of the $\phi = 0°$ MTF has been regained, and the high-frequency bars on the $\phi = 0°$ log-periodic target are visible.

There are no noticeable changes in the target sections for 1.0λ of spherical aberration.

Astigmatism

The cylindrical symmetry of the astigmatic wavefront produces an effect on an image that is highly dependent upon focal position. Three focal positions were considered in this study: the sagittal focus ($W_{20} = 0$), the mid focus ($W_{20} = -\frac{1}{2}W_{22}$), and the tangential focus ($W_{20} = -W_{22}$).

The orientation of the astigmatism was such that the direction of the astigmatic sagittal image was parallel to the y axis. Information about the effects of astigmatism in this orientation ($\alpha = 0°$) also describes the case where the astigmatism is oriented at $\alpha = 90°$. In particular, the MTF for the sagittal (or tangential) focus when $\alpha = 0°$ is identical to the MTF for the tangential (or sagittal) focus when $\alpha = 90°$. The PTF's for $\alpha = 0°$ and $\alpha = 90°$ are related in a similar fashion and are identical except for a change of sign. The MTF for the mid focus position is the same for both orientations, as is the PTF except for a change of sign.

The point spread function in the presence of astigmatism is shown in Fig. 79. For 0.5λ of astigmatism at the mid focus, the point spread function appears unaberrated. At the sagittal and tangential foci the central core is slightly egg-shaped, and the intensity distribution in the surrounding plateau exhibits a slight threefold symmetry. The narrow end of the egg-shaped core points radially in the direction

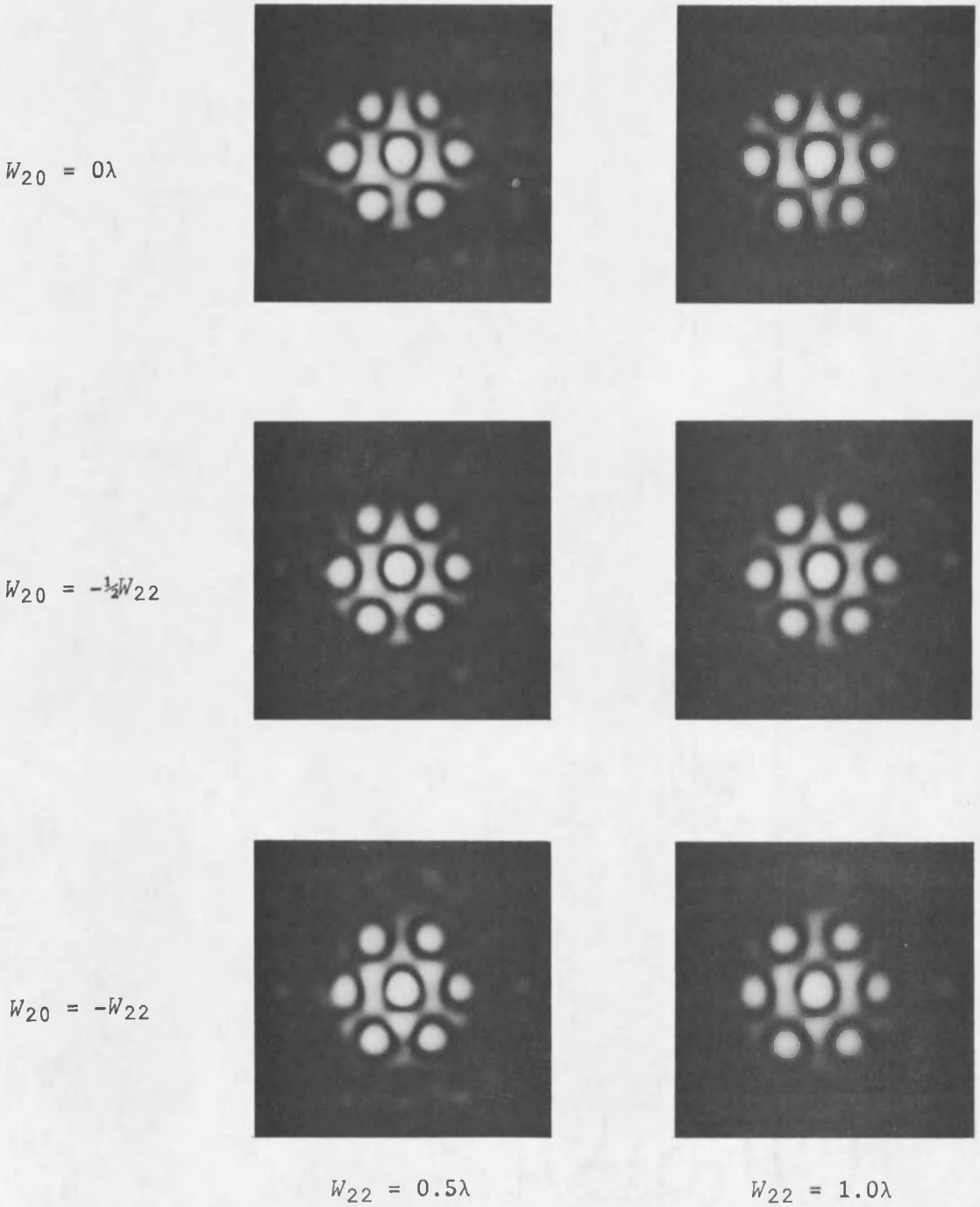

Fig. 79. PSF for Astigmatism.

of the aberrated pupil at the tangential focus and away from it at the sagittal focus.

When 1.0λ of astigmatism is present, the spread function appears distorted for all focal positions. At mid focus the central core has an oval rather than an egg shape and the surrounding plateau is more uniformly illuminated than at the sagittal or tangential foci.

The effect of astigmatism on the transfer function is illustrated in Figs. 80 and 81. In each figure the transfer function is plotted for one value of astigmatism at the three focal positions. For 0.5λ of astigmatism (Fig. 80), the transfer function is affected very little. The sagittal focus is the worst for both the $\phi = 0°$ and $\phi = 45°$ directions, and, as expected, the mid focus is the best. At the tangential focus the MTF is never reduced more than 0.04 from the unaberrated curve except at very low spatial frequencies where the reduction reaches 0.08. The PTF error is less than 0.1 cycle over most of the spatial frequency region. The mid focus transfer function is practically unaffected.

When 1.0λ of astigmatism is introduced, the effect on the transfer function is more significant (see Fig. 81). The high-frequency (less than 0.6) region of the $\phi = 0°$ MTF is very low for both the tangential and the sagittal foci although the response for the mid focus curve is high. At low spatial frequencies (less than 0.2) the sagittal focus MTF is decreased by as much as 0.1 and the tangential focus MTF is not reduced at all. For the $\phi = 45°$ MTF the sagittal and tangential focus curves are reduced by 0.04 to 0.06 from the unaberrated curve. At mid focus the reduction in MTF is about 0.03.

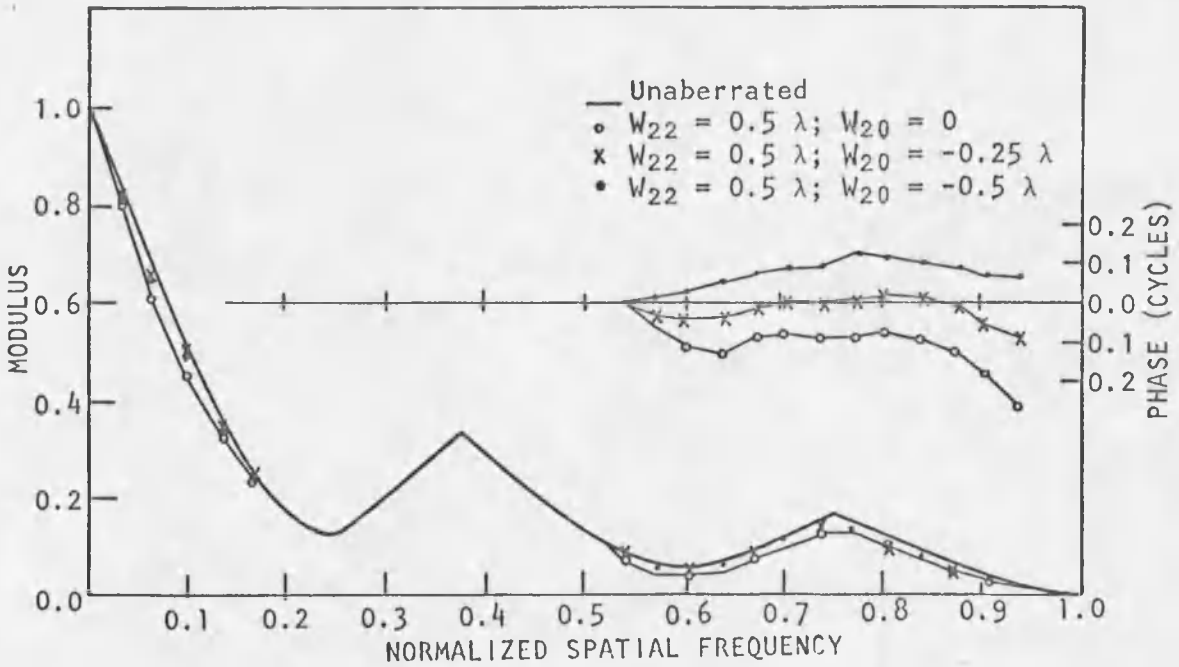

a $\phi = 0°$

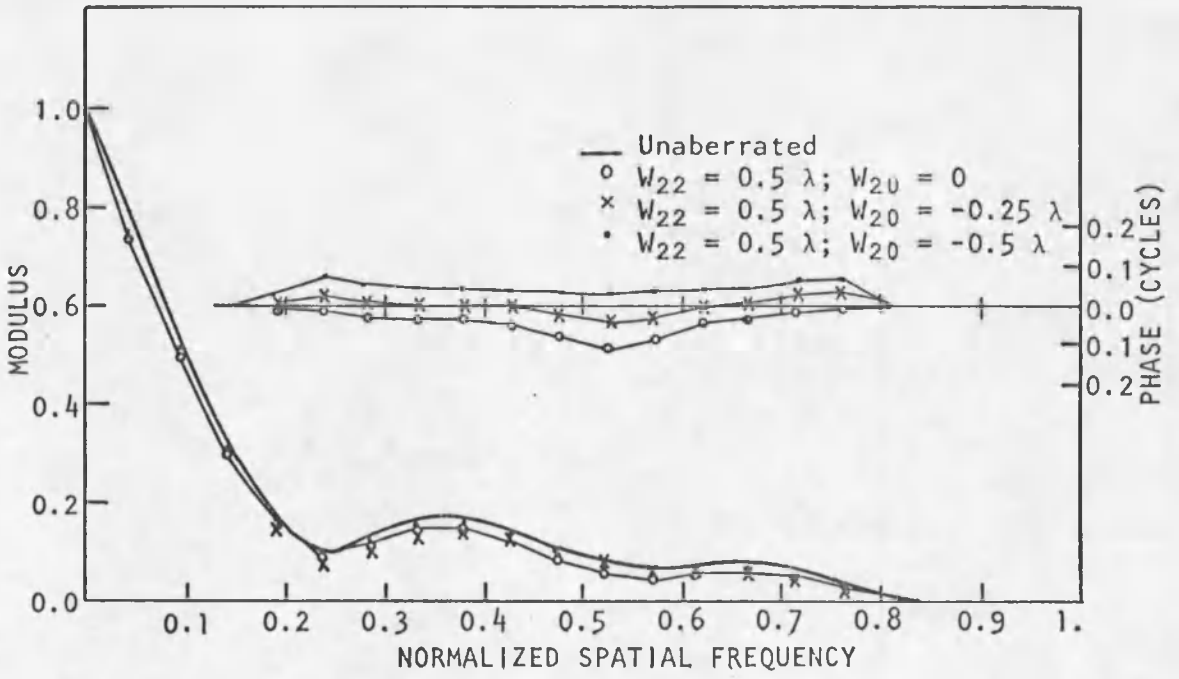

b $\phi = 45°$

Fig. 80. Transfer Function for Astigmatism ($W_{22} = 0.5\lambda$).

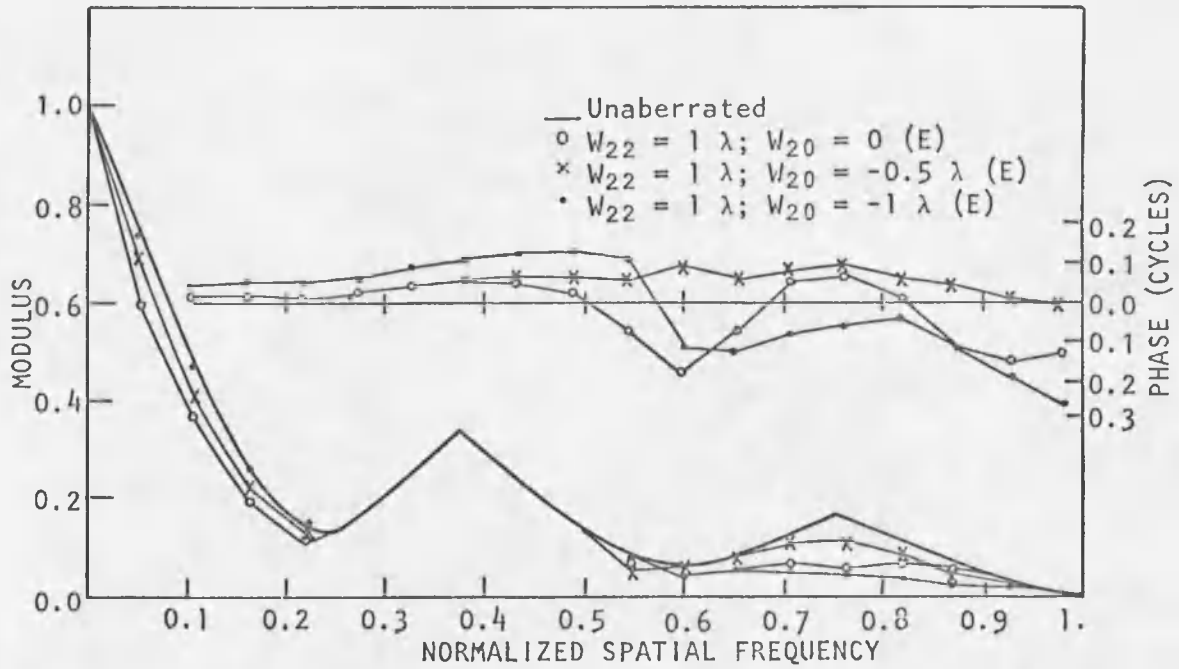

a $\phi = 0°$

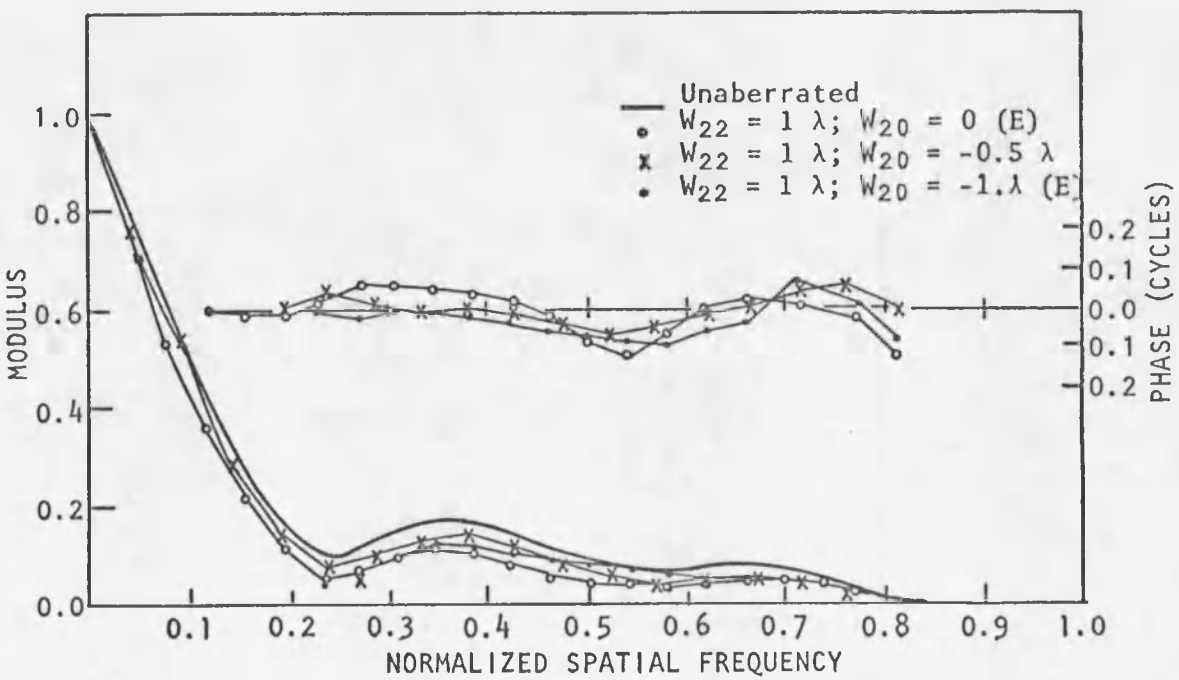

b $\phi = 45°$

Fig. 81. Transfer Function for Astigmatism (W_{22} = 1λ).

The $\phi = 0°$ PTF varies by about one fourth of a cycle in the high-frequency region for the satittal and tangential foci. At mid focus, the phase error is less than 0.1 cycle. The $\phi = 45°$ PTF error at mid focus is also less than 0.1 cycle.

The reduction in the MTF is reflected in the log-periodic target photographs shown in Fig. 82. For 1.0λ of astigmatism the high-frequency (greater than 0.6) portion of the $\phi = 0°$ target is not resolved for the sagittal and tangential foci. However, at the mid focus they are visible. At the sagittal focus in the low-frequency region there is more apparent double imaging than at the other foci. This is consistent with the lower MTF for the sagittal focus as shown in Fig. 81a.

The target section photographs do not show much change with the introduction of astigmatism. One feature that does change is the railroad tracks in target section B1 (Fig. 83). When 1.0λ of astigmatism is introduced, the tracks are more distinct at mid focus than at the other foci.

Coma

The point spread function does not change significantly until large amounts of coma are introduced. Figure 84 shows that 0.4λ of coma produces only a slight asymmetry in the core and surrounding plateau. The asymmetry is somewhat worse for $\alpha = 90°$ than for $\alpha = 0°$. When the coma reaches 1.0λ the PSF is clearly aberrated, but not as much as with an equal amount of defocus or tilt.

The transfer function curves (Figs. 85 and 86) also show that coma oriented at $\alpha = 0°$ is more harmful than coma oriented at $\alpha = 90°$.

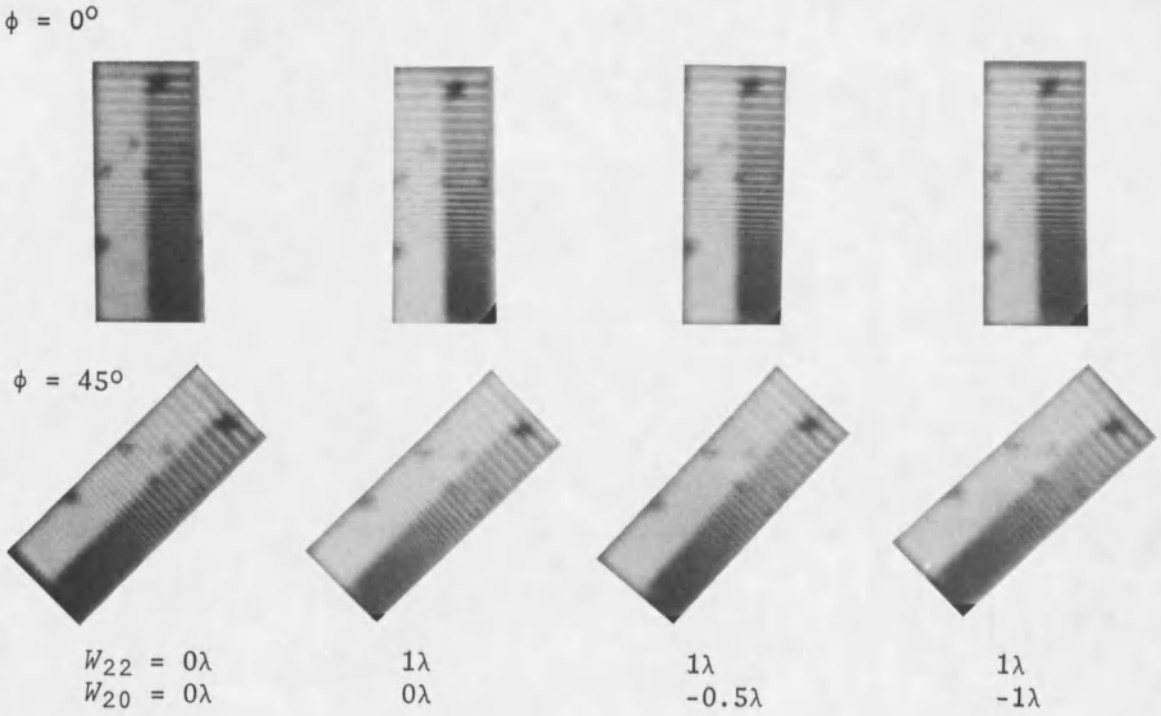

Fig. 82. Log-Periodic Target for Astigmatism.

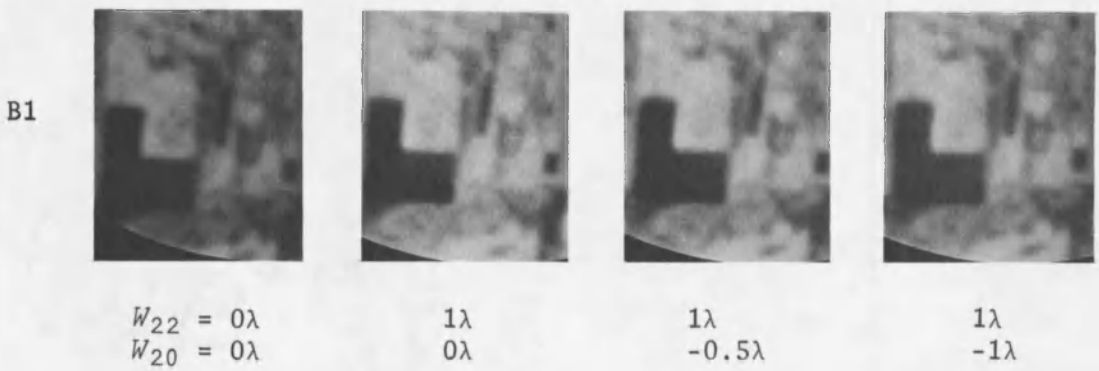

Fig. 83. Target Section B for Astigmatism.

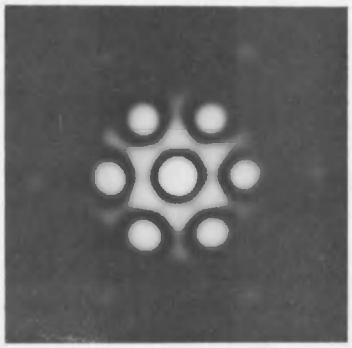

W_{31} = 0λ

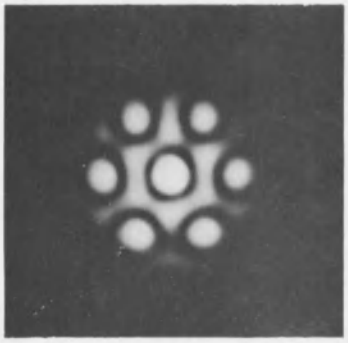

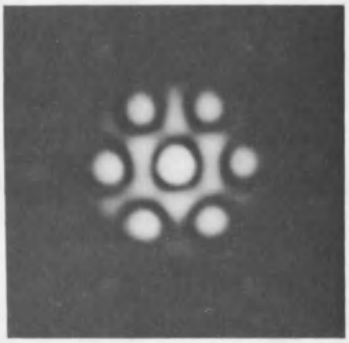

W_{31} = 0.4λ

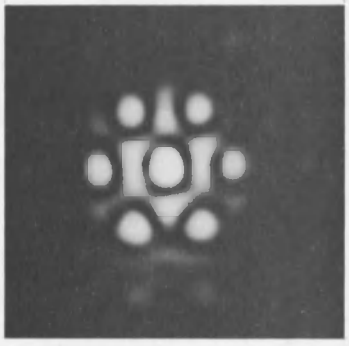

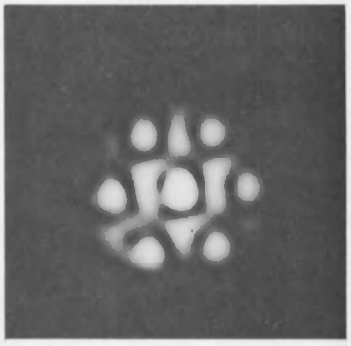

W_{31} = 1.0λ

α = 0°

α = 90°

Fig. 84. PSF for Coma.

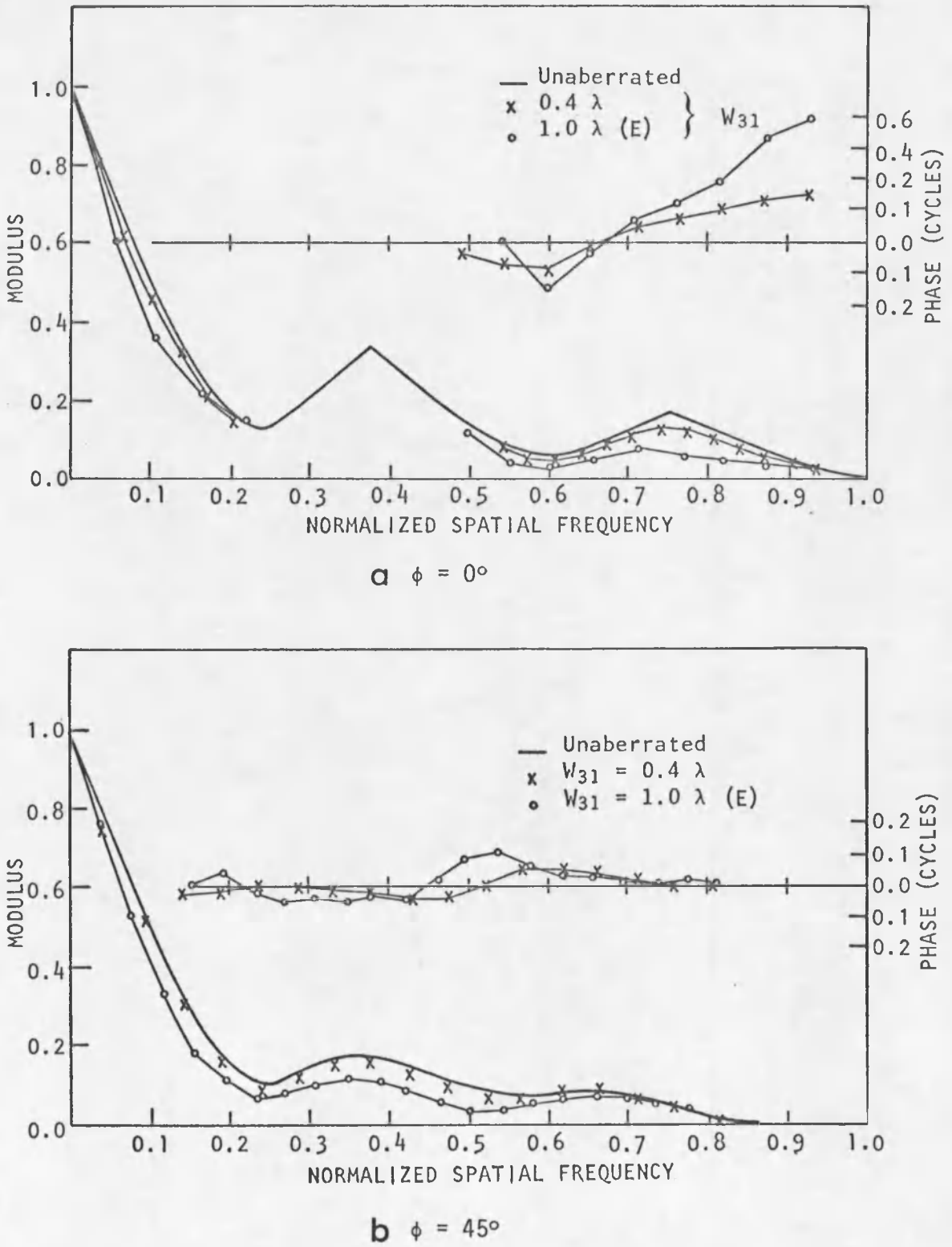

Fig. 85. Transfer Function for Coma (α = 0°).

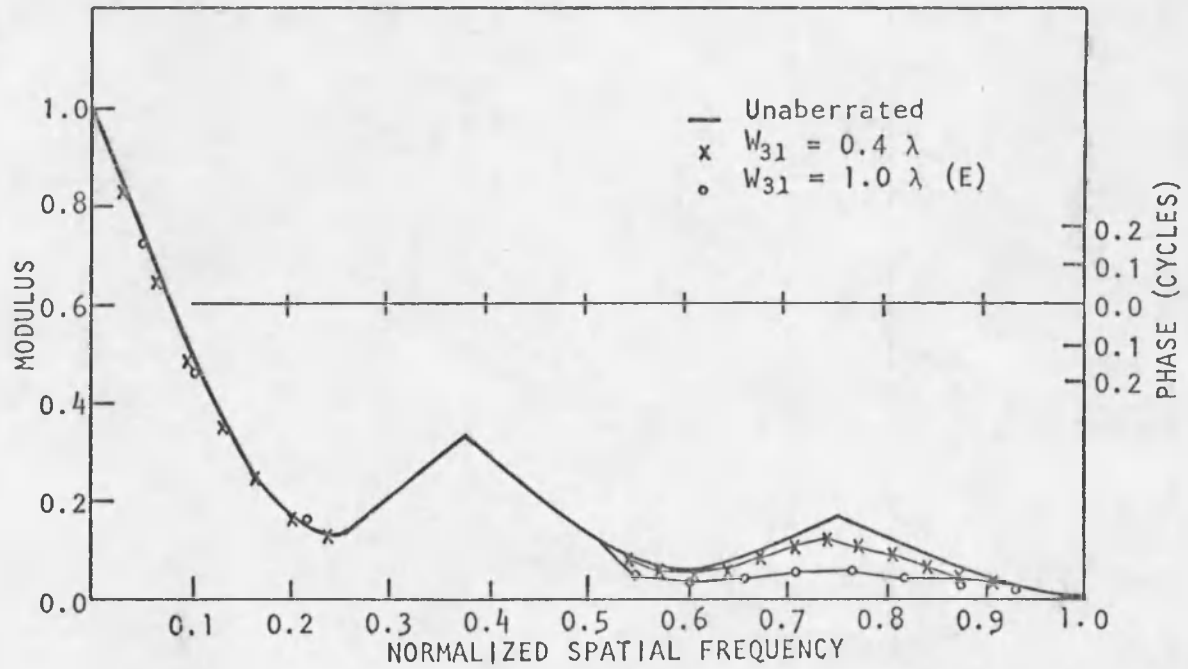

a $\phi = 0°$

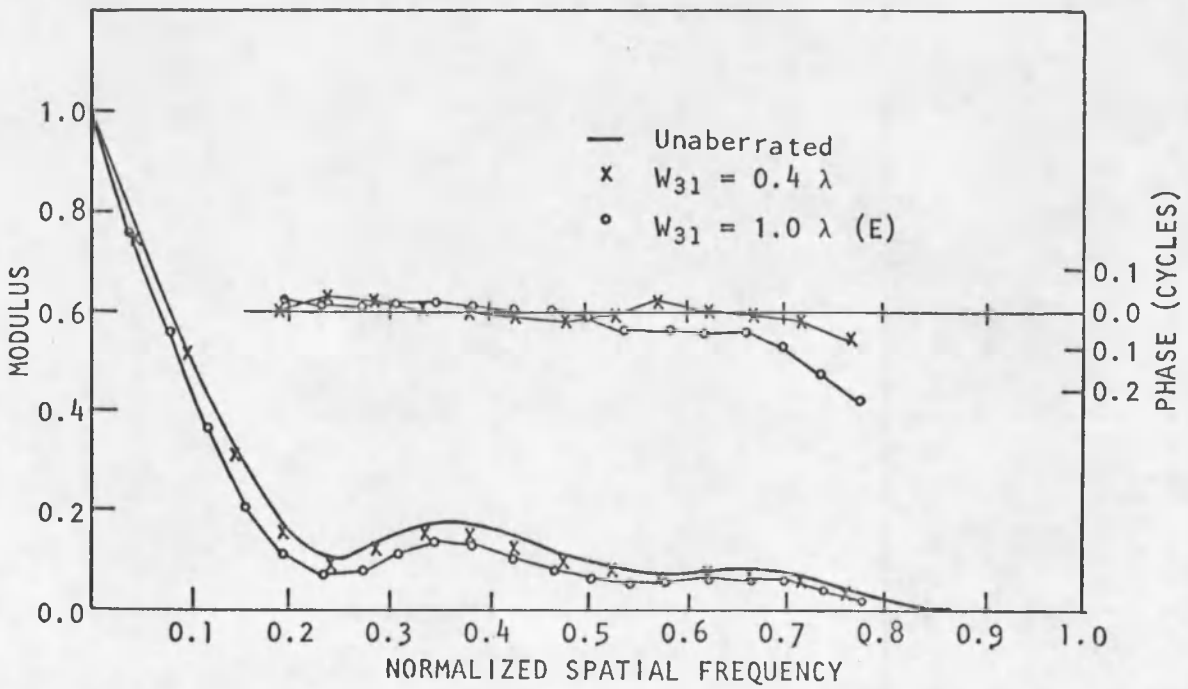

b $\phi = 45°$

Fig. 86. Transfer Function for Coma ($\alpha = 90°$).

However, 0.4λ of coma does not have an appreciable effect on the PTF or MTF for either orientation. For 1.0λ of coma the high-frequency region (greater than 0.6) of the $\phi = 0°$ transfer function has fallen to 50% of its unaberrated value. The phase error is large at the higher spatial frequency components although its significance is diluted by the low modulation in that region. The decrease in high-frequency response is illustrated in the $\phi = 0°$ log-periodic target in Fig. 87.

The $\phi = 45°$ transfer function is hardly affected by 0.4λ of coma. For 1.0λ of coma oriented at $\alpha = 0°$, the $\phi = 45°$ MTF is decreased to about 65% of its unaberrated value in the spatial frequency region 0.25 to 0.6. In the same region an equal amount of coma oriented at $\alpha = 90°$ reduces the MTF to about 75% of its unaberrated value. The PTF for both orientations is insignificant.

The effect of up to 1.0λ of coma on the target sections is subtle. Some changes can be seen in the B1 target section (Fig. 88). The contrast of the railroad tracks decreases slightly as coma is introduced.

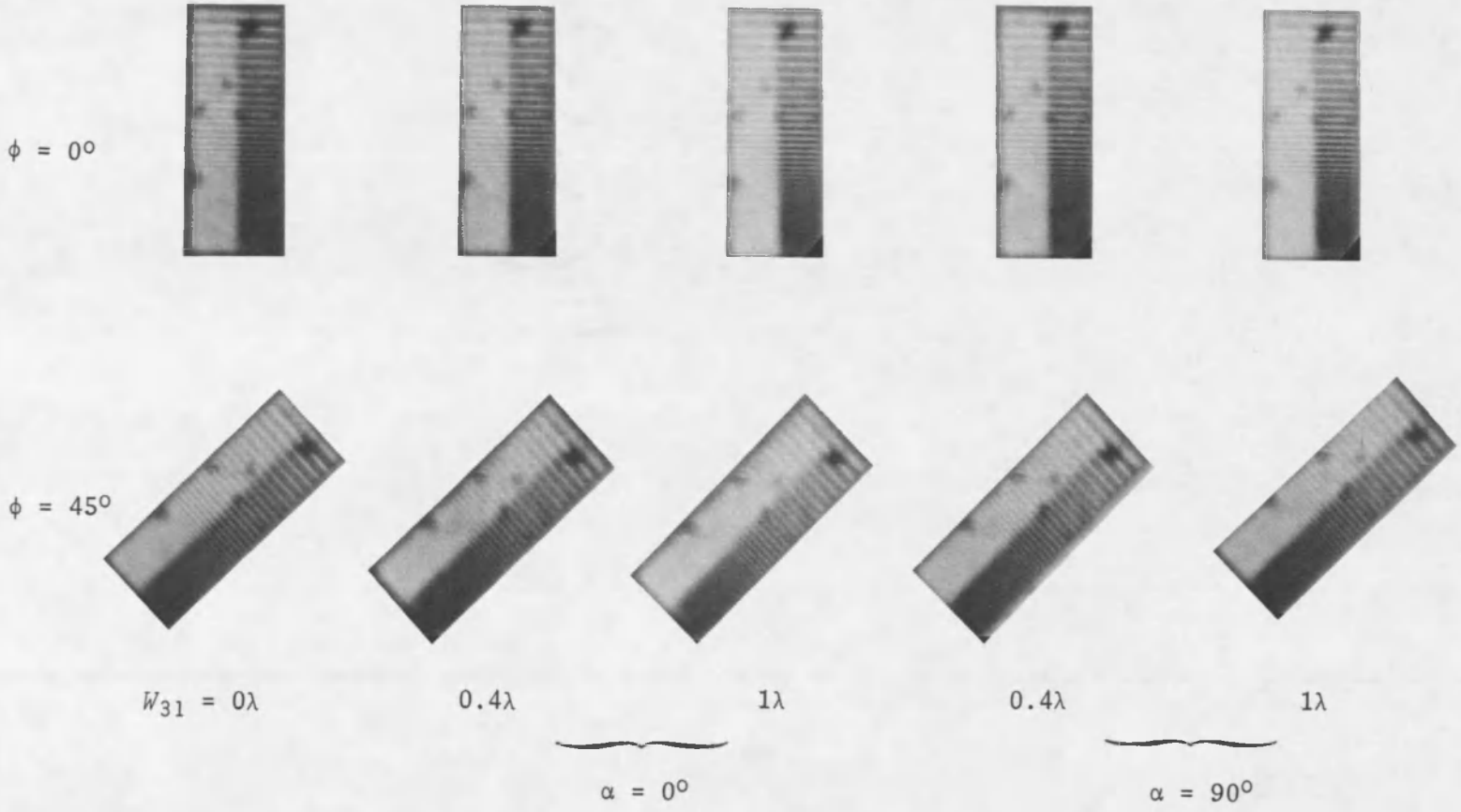

Fig. 87. Log-Periodic Target for Coma.

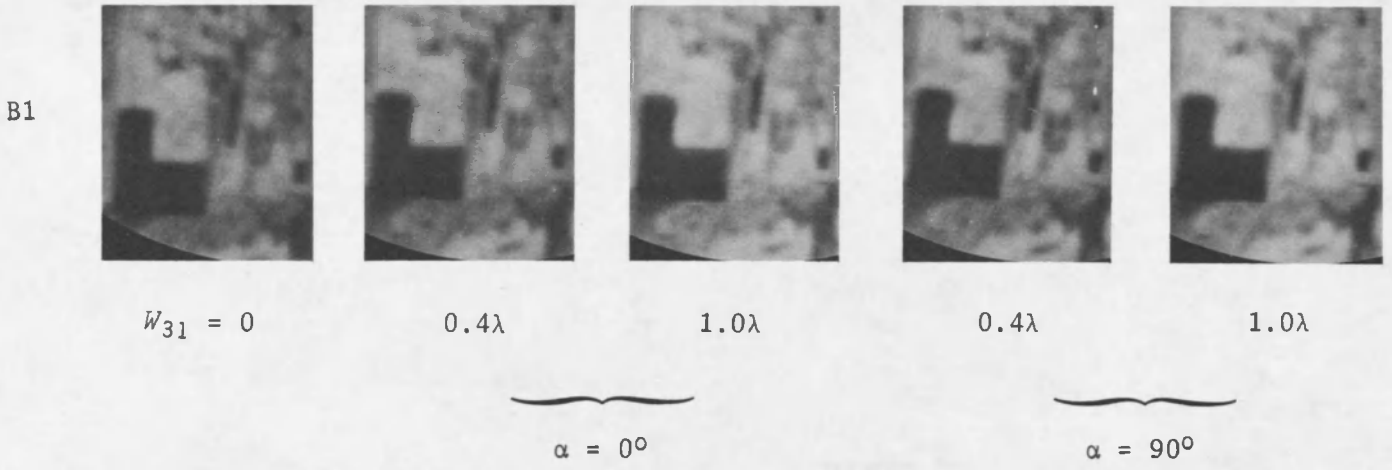

Fig. 88. Target Section B for Coma.

CHAPTER VI

CONCLUSIONS

The effects of aberrations on the wavefront variance, the point spread function, the transfer function, and images of extended objects have been discussed. In the present chapter these effects will be correlated so that conclusions may be drawn about the general nature of the aberration effects, the relative sensitivity of the aberrations, and the tolerable magnitude of the aberrations.

General Characteristics

With a circularly-symmetric optical system, aberrations may be categorized as (1) changing the phase of the amplitude spread function, (2) changing the location of the point spread function, and (3) changing the form of the point spread function. Introducing piston error changes the phase of the amplitude spread function but has no effect on the imaging characteristics of an incoherently illuminated system. Tilt changes the location of the PSF and gives rise to either a magnification error (if the field dependence is linear) or distortion (if the field dependence is cubic). However, as with piston error, the form of the PSF remains unchanged. Defocus, spherical aberration, coma, and astigmatism change the form of the PSF and hence influence the optical transfer function.

With a synthetic aperture array having one aberrated element, all aberration terms change the form of the PSF and influence the

transfer function. Piston error and linear tilt, which are not really considered to be aberrations in circularly symmetric systems, are among the most serious aberrations in a synthetic aperture system. Since any aberration introduced into one pupil element makes the system pupil function asymmetric, the point spread function is asymmetric and the phase transfer function is nonzero.

As aberrations that change the form of the PSF are introduced into a circularly symmetric system, the quality of the image steadily decreases. This is not the case when one element of a synthetic aperture array is aberrated. If large amounts of aberration are present, the point spread function associated with the aberrated element is very dilute in the region of the spread functions formed by the unaberrated elements. As a result, there is little contribution by the aberrated element to the central core of the synthetic aperture PSF, and increasing the magnitude of the aberration has little or no effect.

The effect of piston error in a synthetic aperture system is unlike any aberration in an incoherently illuminated, circularly symmetric system. The influence of piston error on the image is cyclical as the magnitude of the piston error increases. Unaberrated images will be formed by monochromatic light whenever the piston error is a multiple of the wavelength.

As discussed in Chapters II and IV, images formed by synthetic aperture systems exhibit artifacts that are particularly noticeable in the vicinity of edges and linear objects. These artifacts are produced by the relatively large amount of energy in the skirts of the line spread function, and by the plateaulike shape of the skirts. As

aberrations are introduced, light from the central core of the point spread function is redistributed outward, and the amount of energy in the skirts increases. Depending on the nature of the aberration, this redistribution of energy can increase the effect of the artifacts. For example, with tilt and system defocus there is a significant increase in the artifact called double imaging. With piston error there is no noticeable increase, and with the other aberrations there is only a slight increase.

The quality of an image formed by a synthetic aperture system is highly dependent upon the orientation of the image. Figures 47 and 48 in Chapter V showed that certain features that are resolved for one target orientation are not resolved for a different orientation. Since the transfer function has hexagonal symmetry, the image quality varies in a cyclical manner as the object is rotated through 360°. When aberrations are introduced, the hexagonal symmetries of the point spread function and the transfer function are, in general, destroyed. As a result, the image quality varies in a more complex manner as the orientation of the object is changed.

Just as the image quality is dependent upon the orientation of an object relative to the array, it is also dependent upon the orientation of the aberration relative to the array. For example, the effect of tilt on the $\phi = 0°$ transfer function is less if $\alpha = 90°$ than if $\alpha = 0°$. For either orientation, the effect on the $\phi = 45°$ transfer function is about the same. Similarly, coma and astigmatism produce a smaller effect on the $\phi = 0°$ transfer function if they are oriented at $\alpha = 90°$ rather than at $\alpha = 0°$.

This is not to say that the values of the two-dimensional transfer function as a whole are larger if α equals 90° rather than 0°. As we saw in Chapter II, the central ordinate of the point spread function is the same regardless of the orientation of tilt. Therefore, the volume under the transfer function must be the same for all tilt orientations. By changing the orientation of tilt, coma, or astigmatism, the form of the two-dimensional transfer function is changed, but not its volume. For a particular object with a given orientation, there is a preferred orientation for the aberration. However, if there is no a priori knowledge of the object distribution, then no preferred orientation can be selected.

Correlations

Four different quality criteria were correlated to determine the relative significance and the tolerable magnitude of the aberrations. Two of the criteria (wavefront variance and area under the transfer function cross sections) are objective, and the other two (the appearances of the point spread function and the target image) are subjective.

General expressions for the wavefront variance were derived in Chapter II. For small aberrations (less than $\lambda/4$), the variance is proportional to the decrease in the central ordinate of the transfer function and to the decrease in the volume under the transfer function. Since aberrations larger than $\lambda/4$ were used, the relationship between the variance and the PSF and MTF does not necessarily hold. Nevertheless, the variance may still be used as a quality criterion because the main limitation of the variance criterion arises when the aberrations

are greater than 0.75λ when applied to synthetic aperture systems. In this case, the variance continues to increase as the magnitude of the aberration increases although the quality of the image does not change.

A commonly used quality criterion is the volume under the two-dimensional transfer function. Since only two cross sections of the transfer function were measured in this study, the volume could not be determined. As a result, the transfer function was described by the decrease in area under cross sections of the modulation transfer function, and by the area under the absolute value of the phase transfer function cross section. As the area associated with the MTF cross section decreases or the area associated with the PTF cross section increases, the quality of the image generally decreases. The values obtained for the $\phi = 0°$ and $\phi = 45°$ cross sections were averaged to form the modulation area reduction factor (MAR) and the phase error descriptor (PED).

Although the MAR and PED are descriptions of just two cross sections of the transfer function, they are representative of the behavior of the transfer function in most situations. The two cross sections used are at $\phi = 0°$ and $\phi = 45°$ and, as was seen in Chapter II, the $\phi = 90°$ cross section is rather insensitive to aberrations in pupil element 1. It is expected that the behavior of the transfer function for intermediate values of ϕ is not fundamentally different from the cross sections that were considered. That is, as the aberrations are increased, it is unlikely that the MAR or PED would increase for an intermediate value of ϕ while they decreased for $\phi = 0°$ and $\phi = 45°$.

Table 5 compares the wavefront variance, the MAR, and the PED for different magnitudes of the aberrations. Aberrations that have a relatively greater effect for magnitudes of 0.5λ are placed toward the top of the list.

Table 5. Summary of Objective Criteria

Aberration	Magnitude W	MAR	PED	$100\sigma^2$
Piston error	0.1	0.01	58	0.16
	0.25 and 0.75	0.06	150	0.81
	0.5	0.17	210	3.60
	0.5 (W_{20} = -0.66)	0.15	65	0.53
Defocus	0.25	0.03	55	0.36
	0.5	0.11	105	1.21
	1.0	0.26	36	4.85
Tilt α = 0°	0.25	0.06	47	0.25
	0.50	0.18	87	1.00
	0.75	0.24	20	2.25
α = 90°	0.25	0.04	18	0.36
	0.50	0.14	36	1.21
	0.75	0.21	21	4.85
System defocus	0.25	0.04	0	0.25
	0.50	0.18	0	0.81
	0.75	0.38	0	1.96
	1.0	0.52	0	3.60
Astigmatism	0.5	0.08	72	0.49
	1.0	0.18	79	1.96
	0.5 (W_{20} = -0.25)	0.02	19	0.16
	1.0 (W_{20} = -0.5)	0.08	31	0.64
	0.5 (W_{22} = -0.5)	0.06	54	0.49
	1.0 (W_{22} = -1.0)	0.13	87	1.96
Coma α = 0°	0.4	0.04	51	0.36
	1.0	0.18	90	1.96
α = 90°	0.4	0.04	9	0.36
	1.0	0.13	30	1.96
Spherical aberration	0.5	0.08	47	0.75
	1.0	0.14	66	2.9
	1.0 (W_{20} = -1.0)	0.03	28	0.16

The point spread functions and the target images provided a subjective measure of whether significant amounts of aberration have been introduced. The aberrated point spread functions were classified as having no, slight, moderate, or high degradation. The target images were classified according to whether or not there was a noticeable degradation in one of the target sections.

Table 6 compares the changes in the point spread functions and the target images for various aberrations. As in Table 5, the aberrations that produced the largest changes are listed first.

Table 6. Summary of Subjective Criteria.

Aberration		Change in PSF	Change in target sections?
Piston error	0.1λ	None to slight	No
	0.25λ	High	Yes
Tilt	0.25λ	Slight to moderate	No
	0.5λ	High	Yes
Defocus	0.25λ	Slight	No
	0.5λ	High	Yes
Over-all defocus	0.25λ	None	No
	0.5λ	Moderate	Yes
Astigmatism	0.5λ	Slight	No
	1.0λ	Moderate	Yes, faint
Coma	0.4λ	Slight	No
	1.0λ	Moderate	Yes, faint
Spherical aberration	0.5λ	Slight	No
	1.0λ	Moderate	Yes, very faint
Astigmatism at mid focus		None	No
Spherical aberration at mid focus		Slight	No

Several conclusions may be drawn from the comparisons in Tables 1, 5, and 6. Piston error is by far the most significant aberration. Its effect is negligible when $W_{00} = 0.1\lambda$ but is very much apparent when $W_{00} = 0.25\lambda$. Tilt, defocus, and system defocus have approximately the same effect when their magnitudes are less than 0.75λ. For magnitudes of 0.25λ their effect is insignificant, and for 0.5λ their effect is noticeable. The maximum tolerable magnitude of these three aberrations is about 0.35λ. The least sensitive aberrations are astigmatism, coma, and spherical aberration. Their effect is insignificant for magnitudes less than 0.5λ although it is noticeable for magnitudes of 1.0λ. A tolerable magnitude for these aberrations lies in the range 0.5λ to 1.0λ.

Balancing piston error, astigmatism, and spherical aberration with defocus can improve the system performance significantly. As was seen in Chapter IV, 0.5λ of piston error produces a dramatic effect on the transfer function and point spread function. However, if the piston error is balanced with -0.66λ of defocus, the net effect is approximately equivalent to 0.25λ of piston error. Similarly, 1.0λ of astigmatism or spherical aberration produces a noticeable if not large effect. By refocusing to the best focal position ($W_{20} = -0.5W_{22}$ or $W_{20} = -1.0W_{40}$), the system performance is increased to the point where the aberration has no noticeable effect.

Table 1 listed the minimum detectable aberration magnitudes based on wavefront variance considerations. These magnitudes are consistent with the magnitudes producing observable changes in the point spread function (Table 6). However, changes in the target image are not observable until aberration magnitudes nearly twice as large are introduced.

APPENDIX A

DESIGN OF THE ABERRATION GENERATOR

The optical layout of the aberration generator is shown in Fig. 23, and the detailed optical specifications are given in Table 7.

Elements A, B, and C were fabricated at the Optical Sciences Center, and elements D through K were fabricated by Herron Optical Company. (Surface radii match Herron's test plates.) The optical elements had a peak-to-peak surface error of less than $\lambda/12$ (at λ = 550 nm); a cosmetic surface quality of 40-30, and a centration of better than 1 min of arc. All elements were antireflection coated by Herron.

The motions of the optical elements that were necessary to produce the desired aberrations are listed in Table 8.

Table 7. Optical Specification of the Aberration Generator.

Element	Axial thickness	Axial spacing	Radius of curvature Front	Radius of curvature Back	Diameter	Clear aperture	Material
A	5.0		∞	∞	32	28	BK7
		ASAP					
B	5.0		∞	24,400 cc	32	28	BK7
		ASAP					
C	5.0		24,400 cc	∞	32	28	BK7
		ASAP					
D	2.54		846.55 cc	57.22 cc	32	28	KF9
		8.04					
E	5.08		70.36 cx	∞	35	32	SK5
		1.50					
F	2.54		70.36 cc	∞	35	32	SK5
		8.04					
G	5.08		∞	72.64 cx	36	32	SK5
		ASAP					
H	5.08		72.64 cx	∞	36	32	SK5
		8.04					
I	2.54		∞	70.36 cc	35	32	SK5
		1.50					
J	5.08		∞	70.36 cx	35	32	SK5
		8.04					
K	2.54		57.22 cc	846.55 cc	32	28	KF9

Note: All dimensions are in millimeters.

ASAP ≡ as small as practicable

cc ≡ concave

cx ≡ convex

Table 8. Mechanical Specification of the Aberration Generator.

Element	Motion					Aberration introduced		
	x	y	z	Rotation	Least count	Type	Least count	Maximum
A	--	--	--	±6° about x axis	0.15°	W_{00}	0.05λ*	±16λ
B	--	--	--	±90° about y axis	1°	W_{22}	0.2λ*	±6.7λ
C	--	--	--	±90° about z axis	1°			
D	--	--	±0.5 mm	--	10 μm	W_{20}	0.08λ*	±3λ
E,F	--	--	±5.6 mm	--	100 μm	W_{40}	0.1λ	±2λ
G	(Stationary)	--	--	--	--			
H	(Stationary)	--	--	--	--			
I,J	±1.5 mm	±1.5 mm	--	--	25 μm	W_{31}	0.1λ	±3λ
K	±60 μm	±60 μm	--	--	0.5 μm	W_{11}	0.1λ	±12λ

Note: * For small amounts of aberration.

APPENDIX B

THE LINE SPREAD FUNCTION PROGRAM

The Line Spread Function Program calculates the cross section of the optical transfer function from the measured line spread function (LSF) using a Fast Fourier Transform routine. The modulus of the transfer function is then multiplied by a correction factor that takes into account the finite size of the slit used to measure the line spread function (see slit width discussion in Chapter IV).

The LSF input to the program must be described by 2^n data points. Although any n may be used with the Fourier transform routine, the correction factor will be properly scaled only for $n = 7$ (corresponding to 128 data points). The scale of the correction factor is also dependent upon the size of the LSF sampling interval. Since this interval is different for the $\phi = 0°$ and $\phi = 45°$ scans, it is necessary to specify MAJOR AXIS to indicate a $\phi = 0°$ scan or 45 DEGREE AXIS to indicate a $\phi = 45°$ scan.

The outputs of the program are the real part, imaginary part, modulus, and phase of the optical transfer function. In addition, the corrected modulus is printed. The modulus is normalized to unity at the origin, and the phase is expressed in fractions of a cycle. The spatial frequency interval $\Delta\nu$ between adjacent output points is

$$\Delta\nu = \frac{1}{(2^n)(\Delta s)} ,$$

where 2^n is the number of input data points and Δs is the spatial interval between input data points.

A sample input data deck is as follows:

```
Control cards
7
 8
  9
*1.0 WAVES COMA
MAJOR AXIS
 0.0
 0.9
46.
 4.
7
 8
  9
(next data deck)
```

The comment card is required. Depending on the scan direction, 45 DEGREE AXIS or MAJOR AXIS is used. The peak value of the LSF (45 in this example) is always the $2^n/2 + 1$ data position. Data are entered in columns 10 spaces wide (1-10, 11-20, 21-31, etc.) and may have three ditits following the required decimal point. If the measured LSF does not fill the 2^n data positions, then zeros must be added to either end of the LSF in order to fill all positions.

APPENDIX C

FINE FOCUSING METHOD

The focal plane of the synthetic aperture system was located using a three-beam interference technique suggested by Shack (1970).

A mask containing three small apertures was placed over the pupil of the synthetic aperture array. One of the holes was positioned on the optical axis and the other two holes were located on each side of and equidistant from the center hole.

The three-beam interference pattern observed in the focal plane of the synthetic aperture system had the form shown in Fig. 89a. A set of low-visibility fringes existed between a set of high-visibility fringes. When the observation plane was moved a distance corresponding to 0.5λ of defocus, the two sets of fringe fields had the same maximum intensity (Fig. 89b). The focal plane, therefore, was found by first adjusting the sensor head on each side of the nominally best focus until the fringes observed on the focusing screen had the same maximum intensity. The plane of best focus was located halfway between the two planes where this occurred.

It was found that with this method the repeatability in positioning the sensor head in the focal plane was better than ± 10 μm. This corresponds to a system defocus of less than $\pm\lambda/50$.

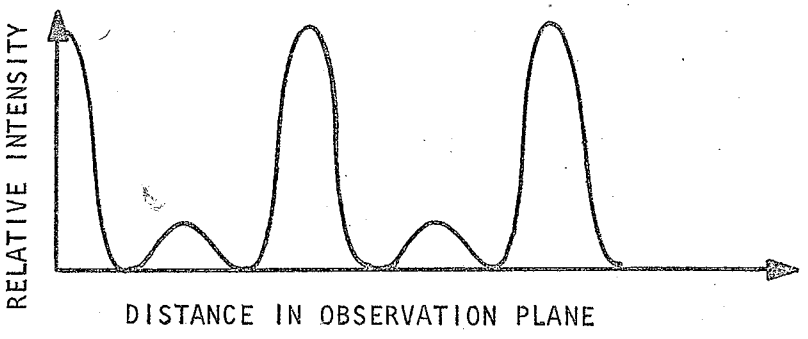

a. In focal plane

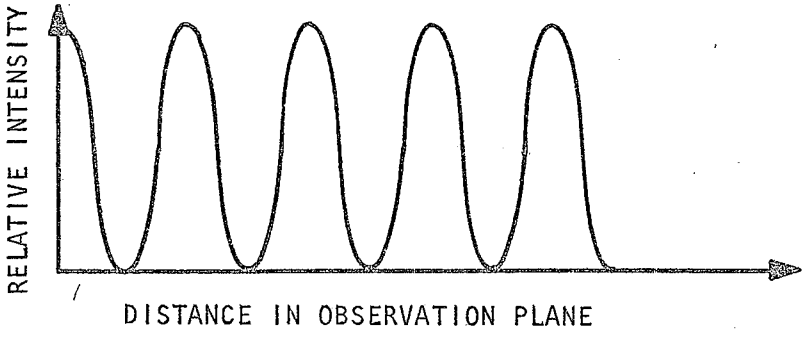

b. $\lambda/2$ out of focus

Fig. 89. Interference Fringes Observed Using Fine Focus Method.

REFERENCES

Born, Max, and Emil Wolf, 1965, *Principles of Optics*, ed. 3 (Pergamon Press, New York).

Boyce, B. M., 1971, "Role of Image Processing in Synthetic-Aperture Systems," J. Opt. Soc. Am. 61:1558A.

Eastman Kodak Company, 1967, *Modulation Transfer Data for Kodak Films*, ed. 3 (Eastman Kodak Company, Rochester, N.Y.).

Fell, Barbara, J. D. Rancourt, and R. R. Shannon, 1971, "The Computer Program FROLIC," Optical Sciences Center (Univ. of Ariz.) report prepared for the U.S. Air Force Avionics Laboratory under Contract AF33613-70-1413.

Golay, M. J. E., 1971, "Point Arrays Having Compact, Nonredundant Autocorrelations," J. Opt. Soc. Am. 61:272.

Goodman, J. W., 1968, *Introduction to Fourier Optics* (McGraw-Hill, San Francisco).

Hopkins, H. H., 1949, "The Disturbance near the Focus of Waves of Radially Non-Uniform Amplitude," Proc. Phys. Soc. B 62:22.

Jain, Anil, 1971, "Random Misalignments and the MTF of Segmented-Mirror Optical Systems," J. Opt. Soc. Am. 61:1586A.

Kishner, S. J., 1971, "Measurement of Synthetic-Aperture-Segment Misalignments by Analysis of Edge Images," J. Opt. Soc. Am. 61:1559A.

Meinel, A. B., 1970, "Aperture Synthesis Using Independent Telescopes," Appl. Opt. 9:2501.

Meinel, A. B., R. R. Shannon, F. L. Whipple, and F. J. Low, 1972, "A Large Multiple-Mirror Telescope (MMT) Project," p. 155 in Larmore, Louis, and R. W. Poindexter, eds., *Instrumentation in Astronomy* (Society of Photo-Optical Instrumentation Engineers, Redondo Beach, Calif.).

National Academy of Sciences, 1967, *Synthetic Aperture Optics*, Vol. 2, Woods Hole Summer Study (National Academy of Sciences--National Research Council Advisory Committee to the AFSC, Washington, D.C.).

Rabedeau, M. E., 1969, "Effect of Truncation of Line-Spread and Edge-Response Functions on the Computed Optical Transfer Function," J. Opt. Soc. Am. 59:1309.

Reynolds, G. O., and D. J. Cronin, 1970, "Imaging with Optical Synthetic Apertures (Mills-Cross Analog)," J. Opt. Soc. Am. 60:634.

Russell, F. D., and J. W. Goodman, 1971, "Nonredundant Arrays and Post-detection Processing for Aberration Compensation in Incoherent Imaging," J. Opt. Soc. Am. 61:182.

Sanger, G. M., T. E. Hoffman, and M. A. Reed, 1972, "Some Design Aspects of a Multiple-Mirror Telescope," p. 161 in Larmore, Lewis, and R. W. Poindexter, eds., *Instrumentation in Astronomy* (Society of Photo-Optical Instrumentation Engineers, Redondo Beach, Calif.).

Sanger, G. M., and R. R. Shannon, 1973, "Optical Fabrication Techniques for the MMT," Sky and Telescope 46:280.

Shack, R. V., 1970, Optical Sciences Center, The University of Arizona, personal communication to the author.

Shack, R. V., J. D. Rancourt, and H. Morrow, 1971, "Effects of Dilution on a Six-Element Synthetic Aperture," Appl. Opt. 10:257.

Shannon, R. R., G. M. Sanger, and J. E. Gray, 1971, "Dynamic Processing of Synthetic-Aperture Images," J. Opt. Soc. Am. 61:1558A.

Smith, W. J., 1966, *Modern Optical Engineering* (McGraw-Hill, New York).

Stockton, Martha W., ed., 1970, "Symposium on Synthetic Aperture Optics," Optical Sciences Center (Univ. of Ariz.) Tech. Rept. 58.

Tschunko, H. F. A., and P. J. Sheehan, 1971, "Aperture Configuration and Imaging Performance," Appl. Opt. 10:1432.

Weymann, R. J., and N. P. Carlton, 1972, "The Multiple-Mirror Telescope Project," Sky and Telescope 44:159.

Yansen, D. E., D. J. Cronin, A. E. Smith, and G. O. Reynolds, 1972, "Assessment of Alignment Tolerances in Optical Synthetic Apertures," J. Opt. Soc. Am. 62:743A.

Yansen, D. E., G. O. Reynolds, and D. J. Cronin, 1971, "Optical Synthetic Aperture Analogues of Two Radio Interferometers," Optica Acta 18:167.